RECOMMENDED PROCEDURE FOR DETERMINATION OF RELATIVE PERMEABILITIES

Roland Lenormand and Guillaume Lenormand, Cydarex, France

This paper was prepared for presentation at the International Symposium of the Society of Core Analysts held in Snowmass, Colorado, USA, 21-26 August 2016

ABSTRACT

This paper discusses the basic mechanisms involved during determination of oil/water imbibition relative permeabilities (Kr).

One-step experiments (only one injection pressure or flow-rate) generally referred to as JBN experiments must be discarded even if experiments are interpreted with Pc curves. Their interpretation is based on transient flow dominated by viscous fingering and/or channeling, which does not represent "true" pore-scale relative permeability.

A more accurate UnSteady-State (USS) experiment requires 7 to 10 steps. After the first step, saturations become more uniform and flows are then controlled by local Kr. The range of saturation is controlled by the balance between viscous and capillary forces and works only for the negative part of the Pc curve. The experiment is difficult to design if the Pc curve is not well-known.

Simultaneous injection of oil and water (steady-state, SS) allows a more precise control of saturations. When two fluids are injected at high flow rates, saturation is close to being uniform on a large part of the plug, and its value is controlled by the ratio of viscous forces in the two fluids. This method can be used for any type of wettability.

Based on these observations, the recommended procedure is a compromise between SS and USS methods. We also show that laboratory fluid velocities are much higher than reservoir velocities and discuss how to deal with this issue.

INTRODUCTION

The determination of relative permeabilities by displacements is still a subject of much discussion in oil companies. There is always a debate between Steady-State (SS) and UnSteady-State (USS) methods. The purpose of this paper is to explain the physical mechanisms that govern these displacements, and how they affect the determination of relative permeabilities.

For oil and water displacements, the following definitions are used, independently of wettability: **drainage** is a displacement leading to an increase of oil saturation, and **imbibition** to an increase of water saturation. We will use oil/water imbibition, the most

common case for relative permeabilities. Results can easily be extended to other types of displacements, such as gas drainage.

Kr curves are defined and calculated at local scale, the scale of a Representative Elementary Volume where the two-phase Darcy's laws are written:

$$\frac{Q_w}{A} = -\frac{K\ Krw}{\mu_w}\frac{\partial Pw}{\partial x} \quad ; \quad \frac{Q_o}{A} = -\frac{K\ Kro}{\mu_o}\frac{\partial Po}{\partial x} \tag{1}$$

where, Q is flow rate, K absolute permeability, Kr relative permeability, μ viscosity, P pressure and x the distance along the sample from the injection face. Indices are "w" for water and "o" for oil. Capillary pressure is defined by $Pc = Po - Pw$.

A laboratory experiment is not a "small scale" representation of the reservoir. Especially, the residual oil saturation (Sor) obtained in laboratory depends on laboratory conditions, sample length, flow rates, etc. and differs from the recovery at reservoir scale, controlled by other parameters (geological structure, well implementation, etc.). The purpose of a laboratory experiment is to determine a full curve of relative permeabilities (Kr) as functions of water saturation (Sw) in a very large range of saturation that covers or even exceeds the saturations encountered in the reservoir.

For a given type of displacement (drainage or imbibition), the Kr curves are assumed to be independent of fluid velocities. This means that the viscous coupling between the fluids is negligible, as if the two fluids were flowing in separate channels (see discussion by Ayub and Bentsen [1]). With this assumption, the Kr curves are the same for SS, USS and other types of displacements such as centrifuge experiments. This assumption is in contradiction with the discontinuous flows observed at high flow rates both in micromodel experiments and Digital Rock Physics simulations. It is also often observed that Pc curves determined by history matching differ from Pc curves measured by porous plate or centrifuge methods. Lackner *et al.* [2] attribute this difference to "dynamic capillary pressures" and recommend local pressure measurements using semi-permeable membranes. We will not discuss this point here and assume that both Kr and Pc curves do not depend on fluid velocity.

We will start by discarding the JBN method, in which the information obtained is limited and not accurate, especially in terms of Sor. Then we will analyze the USS and SS methods in terms of balance between viscous forces and capillary forces. Finally we will compare laboratory experiments to numerical simulations at reservoir scale to discuss the problem of fluid velocities and the important notion of Sor.

ONE FLUID INJECTED –ONE STEP (JBN)

This simple experiment of water displacing oil in a sample at irreducible saturation Swi, is usually referred to as JBN, from the name of the authors of the paper describing the Kr

analytical calculation [3]. This method is still often used, because it is quick and cheap, but it presents several drawbacks.

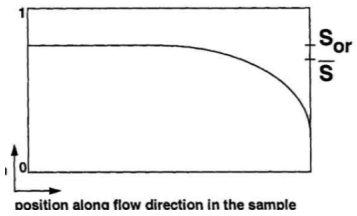

Figure 1 - (from Kokkedee et al) Saturation profile along the plug.

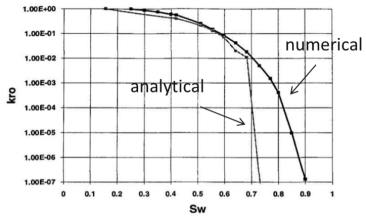

Figure 2 - (from Kokkedee et al). Analytical and numerical Kro.

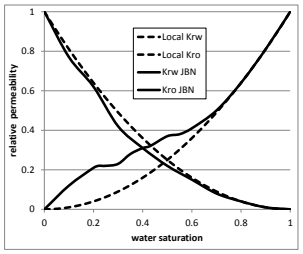

Figure 3 - Kr determination assumed on a heterogeneous sample (from Fenwick et al.)

More than 20 years ago, Kokkedee *et al.* [4] showed that there was always an important error on Sor when the JBN method was used. Whatever the reservoir type, Sor obtained by numerical history matching with capillary pressures is always smaller than the JBN Sor by 15% to 30%. The explanation is illustrated on Figure 1. The JBN calculation assumes a uniform saturation over the sample; however the profile is not uniform and drops near the outlet due to capillary effects. Although the average, derived from the effluent balance, is the same, the "local" saturation near the inlet face is larger than the average saturation. Figure 2 shows the effect on the oil Kr curve.

Another drawback is channeling. In 1988, Mohanty and Miller [5] wrote: "Results illustrate that the early part of the JBN method relative permeability is dominated by fingering and heterogeneity effects. But the later part (> 1PV) represents the relative permeability of the end-face saturation". This result has been confirmed and illustrated by numerical simulations (Fenwick et al. [6]). In their study, the sample is represented as a 2-Dimensional heterogeneous permeability field with uniform Corey-shapes Kr curves for all the grids (dashed lines in Figure 3). The displacement is computed using a streamlines method and the Kr curves are determined from the production and pressure drop, as in a real experiment (solid lines). At low saturations, Krw is larger than the local value because water is flowing in channels more permeable than the average. At the end of the experiment, Kr are close to the local values. The beginning of displacement is also prone to viscous fingering with an adverse mobility ratio (see for instance Sarma et al. [7]). Due to all these problems the one-step injection of water (JBN type experiment) is no longer recommended, even if numerical simulations are used with Pc curves. Multi-step experiments, either SS or USS, provide more accurate results.

MULTI-STEP EXPERIMENTS

For both USS and SS multi-step experiments, the relative permeabilities are determined by history matching of the transient and stabilized parts of differential pressure and oil production. The numerical simulation takes into account a Pc curve, either measured or adjusted from the experimental results together with Kr. As for JBN, the heterogeneity plays a role at the beginning of the first displacement. At the end of the first step and all

the further steps the sample is assumed uniformly saturated with the two fluids and that the Kr are not affected by channeling and fingering.

Using numerical optimization does not provide "points" Kr values as for analytical calculations, but an analytical curve (Corey, LET, etc.) determined by minimizing the mean square root difference between experimental and calculated parameters during both transient and stabilized regimes. The most accurate determination of the Kr curves is when average saturations are numerous and regularly spaced.

Physical mechanisms during USS multi-step displacements

In imbibition, only water is injected, starting at a low flow rate and allowing for stabilization of oil production and differential pressure. Then the water rate is increased, until stability is reached and the process is repeated for 5 to 10 steps. At each step the average saturation increases. We will show that in a USS experiment, average saturation at each step is controlled by the balance between viscous forces and capillary forces. Another important result is that the differential pressure is equal to capillary pressure at entrance when stabilization is reached.

For illustration on a general case, the Pc curve is assumed to have a positive and negative part (mixed wettability). For any step, when stabilization is reached, the water and oil pressures along the samples are schematically displayed in Figure 4a:

- At outlet, the capillary pressure is assumed to be zero; consequently both oil and water are equal to the outlet imposed pressure, taken as reference (P = 0).
- The pressure in oil is uniform since oil is no longer flowing when equilibrium is reached (no gravity).

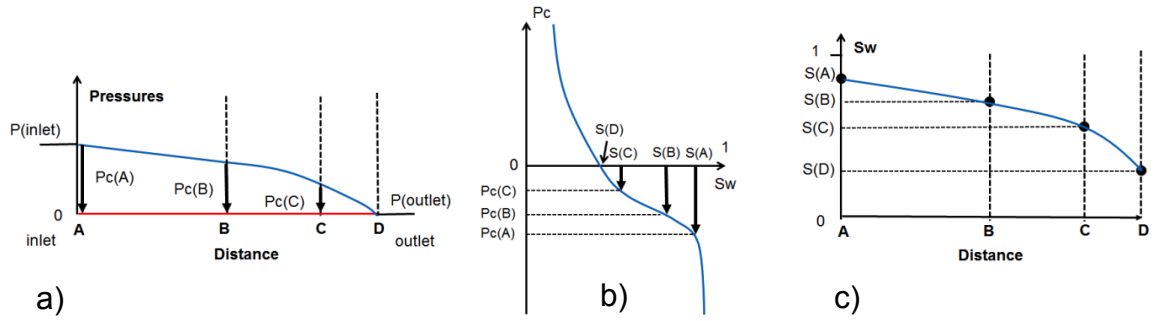

Figure 4 - USS displacement: a) pressures profiles at equilibrium (water blue, oil red), arrows represent the capillary pressure at several locations along the sample, b) determination of corresponding saturations from the Pc curve, c) saturation profile.

- Water is flowing through the sample and since the outlet pressure is 0, the pressure in water is positive everywhere along the sample (a fluid flows from higher to lower pressure). The pressure measured in the inlet end-piece is the highest pressure between the water and oil pressures inside the sample at the entrance, equal to the pressure in water (this point is discussed in [8]) Since $Pc = P_{oil} - P_{water}$, Pc is negative at any location along the sample (arrows in Figure 4a). Consequently, the difference

of pressures measured between the inlet and outlet end pieces is equal to the opposite of the capillary pressure at inlet face (Figure 4a). This property is the principle of determination of the Pc curve by the semi-dynamic method [8].

- From the value of Pc at any location (B, C, D), the corresponding saturation is imposed by the capillary pressure curve (Figure 4b), leading to the saturation profile (Figure 4c).
- At outlet Pc=0 and the corresponding saturation S(D) is equal to the saturation at Pc=0 (where the curve cuts the saturation axis). For an "oil-wet" sample, with totally negative Pc curve, the saturation at outlet is equal to Swi.

Figure 5 shows the flow rate increased by a factor 2. Most of pressures are now in the near vertical part of the Pc curve (Figure 5a and b). Saturation is more uniform on a large part of the sample with a smaller capillary end effect. Average saturation of water has increased and during the experiment a production of oil has been observed.

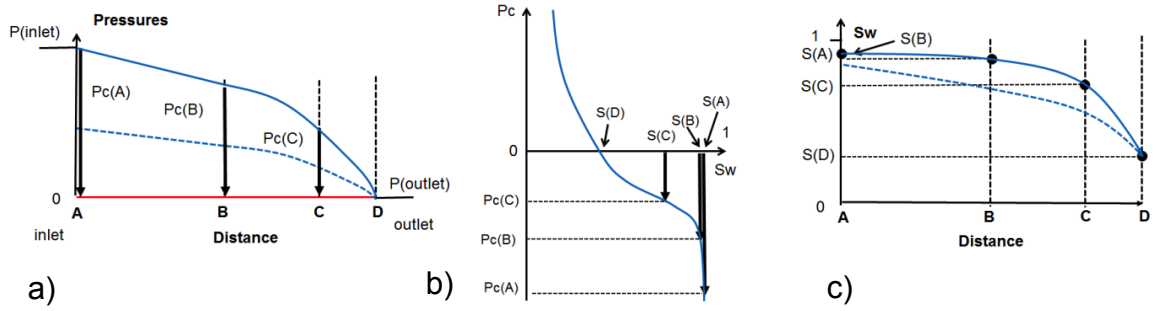

Figure 5 - USS displacement: similar to Figure 4, but with a higher flow rate a) pressure profiles in solid line, previous profiles in dashed lines, b) higher local Pc leads to higher local water saturations, c) saturation profile with the higher flow rate (solid line) showing a decrease of the extend of the capillary end effect.

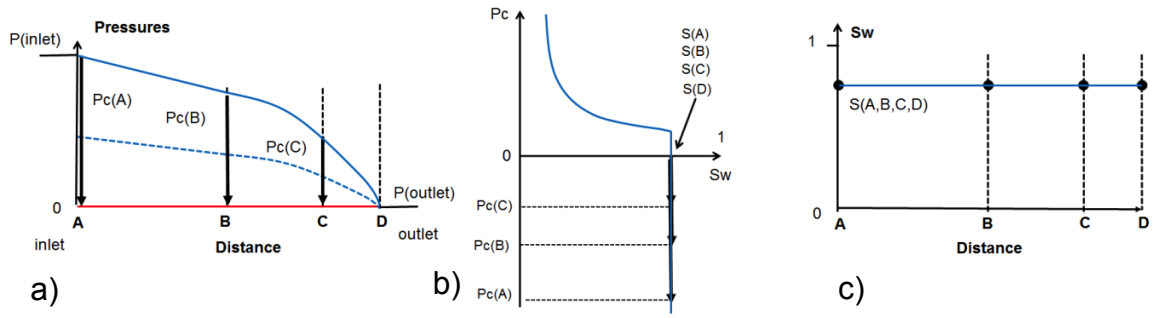

Figure 6 - Pressure and saturation profiles for a water-wet sample. Since Pc is negative, the corresponding saturation is always equal to 1-Sor.

For a water-wet sample (Figure 6), the water pressure profile may defer from the previous case since Kr are different, but the overall shape is similar with positive pressures everywhere in water that is flowing. Capillary pressure along the sample is always negative and for all locations, the local saturation is equal to the maximum value (1-Sor).

When flow rate is increased, saturations do not change since they are at their maximum values and there is no production after the first step.

The main conclusion is that capillary pressure is always negative along the sample. Consequently, local saturations are determined from the negative part of the Pc curve. In drainage it is the opposite.

Numerical example USS

We now illustrate the previous explanation using a numerical simulation with the commercial software CYDAR (http://www.cydarex.fr). Sample, fluid properties and Kr are given in Table 1 and flow rates in Table 2.

Table 1 - Sample and fluid properties for numerical simulations

type of displacement		imbibition
disposition		horizontal
length	cm	8
Diameter	cm	4
Base permeability	mD	100
porosity	frac	0.3
water viscosity	cP	1
water density	g/cm^3	1
oil viscosity	cP	5
oil density	g/cm^3	1
initial Sw	frac	0.2
final Sw	frac	0.8
Krw_max	frac	0.5
Kro_max	frac	0.5
Corey exponent water		3
Corey exponent oil		3

Table 2 - Flow rates during the USS experiment

duration (hour)	5	5	5	5	5	5	5
rate cc/h	2	20	100	250	450	500	1000

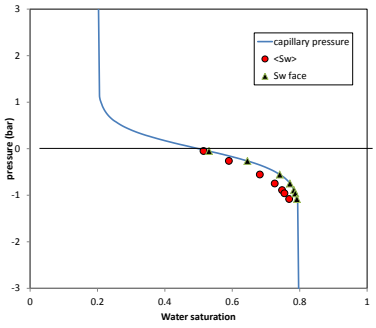

Figure 9 - USS simulation: inlet face capillary pressure versus average water saturations and inlet face saturations;

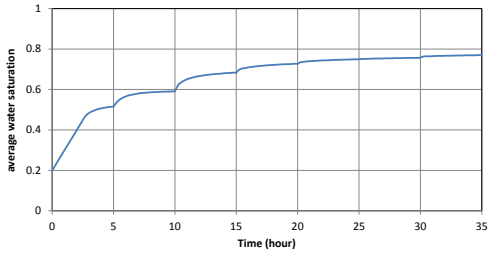

Figure 7 - USS experiment: Water average saturation.

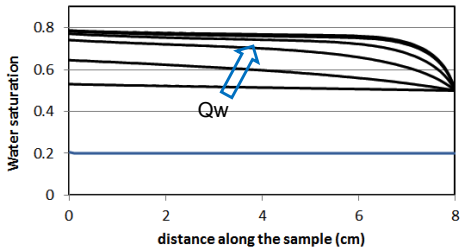

Figure 8 - USS experiment: saturation profiles

Figure 7 shows the average water saturation as function of time. Figure 8 shows saturation profiles at end of each step. For each step there is an increase of average water saturation and consequently additional production of oil.

Figure 9 shows capillary pressure at the inlet face at each stabilized step as function of the average saturation and local saturation. As explained previously, only saturations corresponding to Pc<0 are obtained.

Physical mechanisms during SS multi-step displacements

Oil and water are injected together starting with 100 % of oil at Swi. Then several flow rates (5 to 10) are used by increasing the fraction of water until 100% of water is injected. The displacement mechanisms are more complicated than for the USS case since there are now three types of forces: viscous forces in each fluid and capillary forces.

At the beginning of the experiment, the flow rate is much higher in oil than in water (low water fractional flow) and Pc>0 since pressure in oil is higher than pressure in water (Figure 10a). The local saturations correspond to the positive part of the Pc curve (Figure 10b and 10c). For higher water fractional flow, Pc is negative and local saturations correspond to the negative part of the Pc curve (Figure 11).

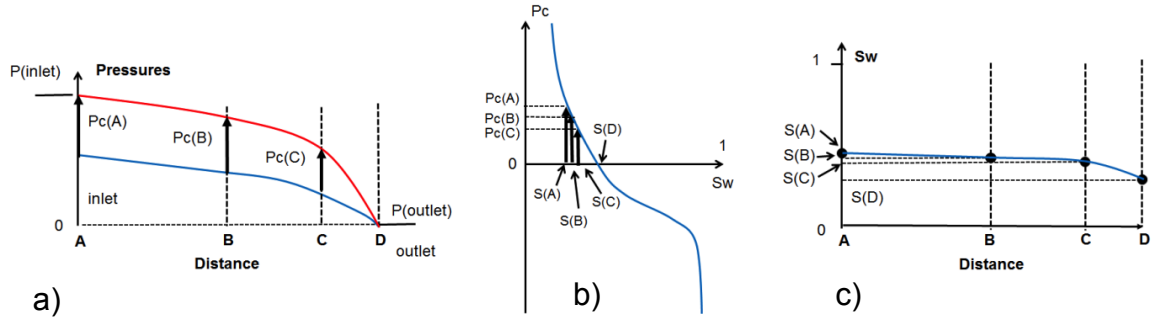

Figure 10 - SS displacement at low water fractional flow: pressure is higher in oil and capillary pressure is positive

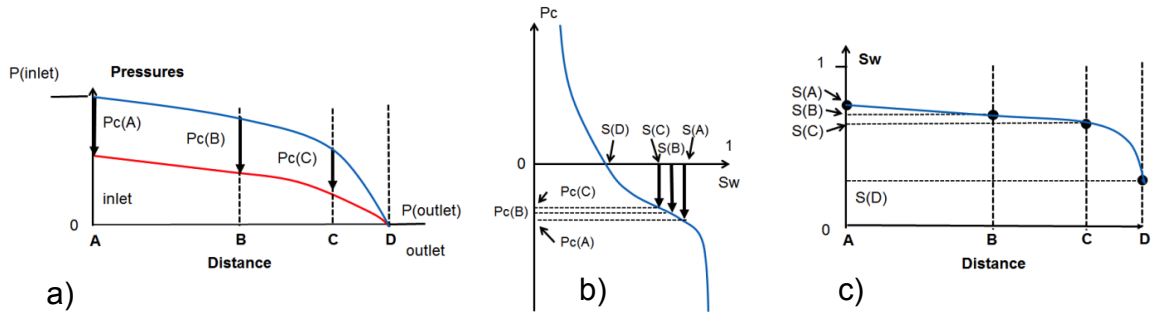

Figure 11 - SS displacement at high water fractional flow: pressure is higher in water and capillary pressure is negative

Numerical example SS

Experiments are simulated using the same fluids and sample properties as for the USS case (Table 1) with 3 total flow rates Qt = 2, 20, and 1000 cc/h. Saturation profiles at end of experiments are shown in Figure 12.

Figure 13 and Figure 14 display the fractional flow as function of average saturation. The numerical fractional flow Qw/(Qw+Qo) is obtained from the simulations when stabilization is reached and the analytical values are derived from Darcy's law with the assumption of Pc=0:

$$fw = \frac{Krw}{\mu_w} \Bigg/ \left(\frac{Krw}{\mu_w} + \frac{Kro}{\mu_o} \right) \quad (2)$$

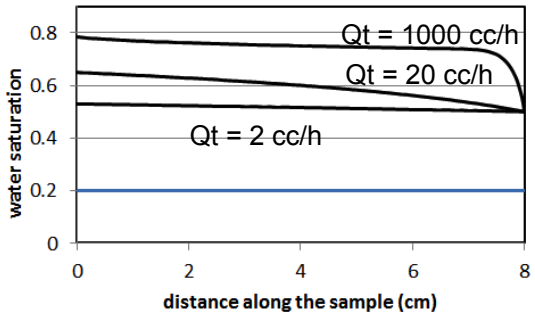

Figure 12 - saturations profiles at end of experiment for 3 total flow rates.

At high total flow rate, Qt = 1000 cc/h (Figure 13), analytical and numerical fractional flows are very close and well-spaced saturations can be determined over all the range of saturations by imposing the fractional flow, independently of the capillary pressure (negligible forces). For lower total flow rate, capillary forces are acting and the numerical fractional flow is no longer close to the analytical one (Figure 14).

In addition, for the lowest total flow rate case (2 cc/h), the range of saturation decreases and the main value is centered around 0.5 where Pc =0. For Qt = 20 cc/h, the average saturation is only in the range 0.3 – 0.6. In the limit of very low flow rate (dashed line in Figure 14), viscous forces are negligible and the final saturation is uniform and equal to 0.5 (spontaneous imbibition).

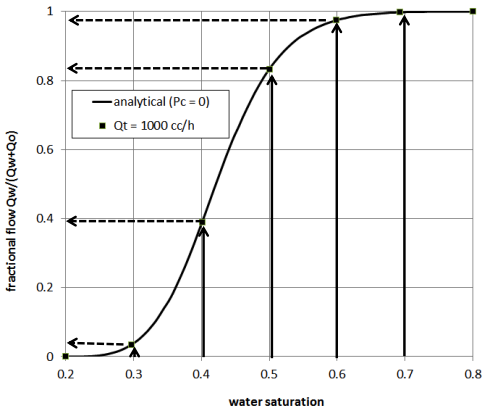

Figure 13 - High total flow rate: Analytical and numerical fractional flows are very close and saturations can be determined by imposing the fractional flow.

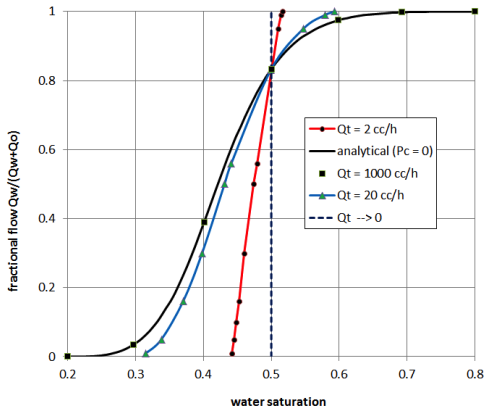

Figure 14 - Analytical and numerical fractional flows as function of average saturation for several total flow rates.

RESERVOIR SCALE DISPLACEMENT MECHANISMS

We will present results of numerical simulation at reservoir scale to illustrate the applications and limitations of laboratory experiments. The reservoir is schematically represented by a 200 meters 1-D medium with same permeability and porosity than the laboratory sample. For Kr properties, we have used 2 cases:

- **Low mobility**, same as the laboratory simulations with Corey exponents $\alpha = 3$;
- **High mobility**, same other properties but with Corey exponents $\alpha = 2$.

For field velocity, we have used the rule of thumb of 1 foot/day and chosen 0.7 foot/day, corresponding to the laboratory injection at 2 cc/h (Table 1). Oil production during 30 years is shown in Figure 15. As expected, production is faster for high mobility. An important result is that after 30 years, even if oil rate is very low, there is still an important pressure gradient in oil along the reservoir, close to the gradient in water and the capillary pressure is higher than -1.2 bar everywhere, even for the high mobility case (Figure 16). From Pc profiles, we have calculated saturation and corresponding Kroil profiles (Figure 17). Another important point is that Kroil is always larger than 10^{-4} (dashed red line) except very close to the injection well.

Table 3 - Equivalence between laboratory total flow rate and front velocity

cc/h	2	20	100	500	1000
foot/day	0.7	6.5	65	162	323

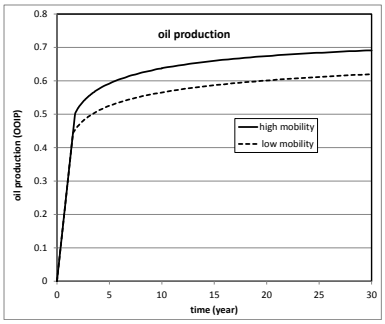

Figure 15 - Oil production during 30 years.

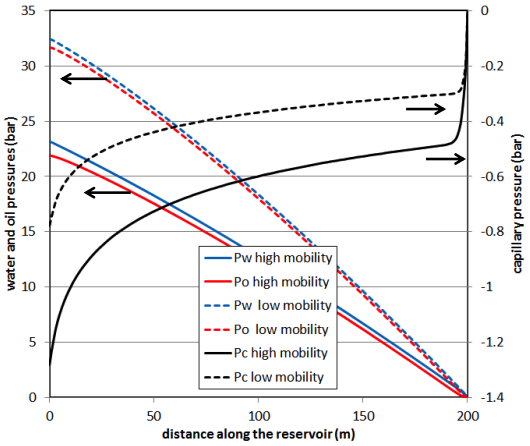

Figure 16 - Numerical simulation for a 1-D reservoir after 30 years of production: water and oil pressure profiles and capillary pressure for 2 values of oil mobility.

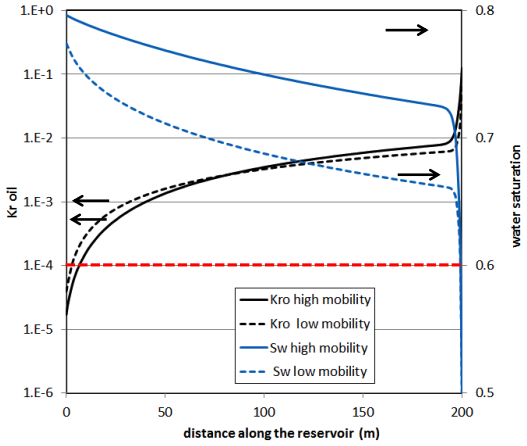

Figure 17 - Numerical simulation for a 1-D reservoir after 30 years of production: water saturation and Kro profiles for 2 values of oil mobility.

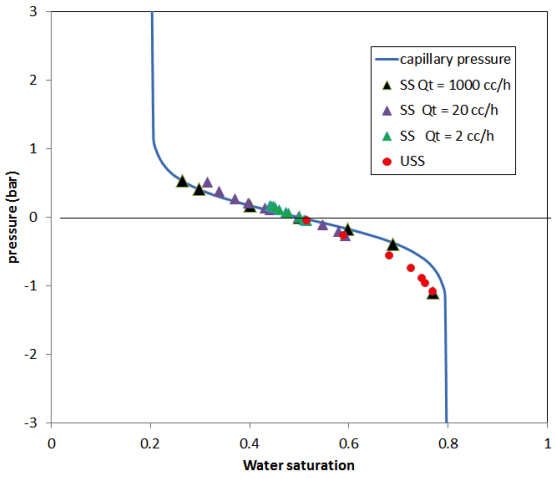

Figure 18 - Range of saturations obtained during the USS and SS displacements performed at various flow rates.

DISCUSSION

We will first present the advantages and drawbacks of SS and USS methods without focusing on the flow rate. We will then discuss how to deal with the fact that reservoir velocities are much lower than designed front velocity. We will finally discuss the notion of residual oil saturation, laboratory values compared to reservoir final recovery.

One fluid injected (USS)

The main drawback is that there is no possibility to have saturations in the positive part of the Pc curve and this method cannot be used for water-wet cases. In addition, when the negative Pc presents a flat plateau, it is difficult to adjust the flow rates to have regularly-distributed saturations. This point is the main limitation of the USS multi-rate method.

Two fluids injected (SS)

Simultaneous injection of oil and water (SS) allows a precise control of saturations. When two fluids are injected at high flow rate, saturation is close to be uniform on a large part of the plug, and its value is mainly controlled by the ratio of viscous forces in the two fluids. This method can be used for any type of wettability. At lower flow rates, the range of saturation is limited (Figure 18).

How to avoid high flow rates during laboratory experiments?

The first answer is to increase the length of the core. Horizontal cores do not exceed 8-10 cm and the standard solution was to use composite cores, several cores put together in the same coreholder. Now, in-situ saturation monitoring shows that there is a huge discontinuity at each contact (Figure 19), and composite cores should be avoided. A better compromise is to take vertical plugs with length around 20 cm.

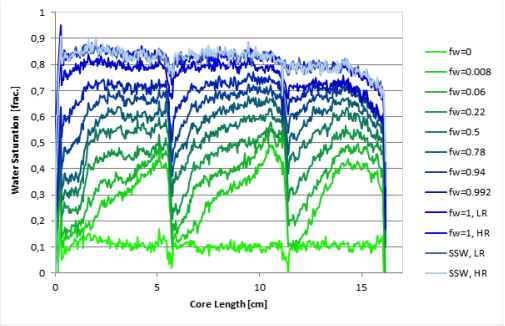

Figure 19 - In-situ saturation monitoring along a composite core showing the discontinuity at each interface.

What is the difference with reservoir? If a 8 cm slice of the reservoir is considered as a plug, the main difference with laboratory is that the condition at outlet is not Pc=0 (this condition is only imposed at the producing well) and local capillary pressures are much higher in the reservoir (see pressure profiles in Figure 16). Semi-permeable porous plates can be used to increase the Pc inside the sample. However, due to the huge pressure drop through the porous plates and their possible partial invasion, it is not possible to derive directly the Kr from standard porous plate experiments (Lenormand *et al.* [9]). Brown in 1951 [10] used a modified Hassler core holder with ceramics plates to measure "dynamic capillary pressures" and to compare them to "static" values, but there was no result for relative permeability. Oil was injected and produced through the ceramic plates and gas through grooves at the contact between ceramics and the sample. A similar equipment was patented by Rose in 1985 [11] for Kr measurement. More recently, Egermann and

Fleury [12] have described an apparatus to measure Kr behind the porous plates, but their equipment does not allow an outlet boundary condition different from Pc = 0. Centrifuge experiments could be a solution to allow high capillary pressure with low flow rate. However, Kr measurements with centrifuge are challenging (Bauget et al. [13]).

Recommended procedure

We will give an example using our numerical simulations. The lower saturations (Pc>0) can be reached only using the Steady-State method. The range of saturations as function of total flow rate is displayed in Figure 18. The highest flow rate can cover all ranges of saturation but a flow rate of 20 cc/h is preferred in order to approximate reservoir velocities. However, this rate limits the final saturation to 0.6. Afterwards a one-fluid injection (USS) is performed with several steps to estimate the negative part of the Pc curve, giving information on the wettability.

Asymptotic values for Sor

Our last point of discussion concerns the residual oil saturation (Sor). When using an analytical function for Kr representation during numerical simulation (Corey or LET), the asymptotic Sor value ($Pc \rightarrow -\infty$) is often equal to zero. For instance, the result presented by Kokkedee (Figure 2) shows a tendency to reach asymptotic zero Sor value. This result is not in contradiction with physical mechanisms: when samples are not strongly water-wet, oil can flow very slowly on the surface of the solid up to very low saturation when pressure is increased. However, this asymptotic value is not the final value reached in reservoir production because capillary pressures are always limited, due to the low mobility of oil, as shown in Figure 16.

CONCLUSIONS

- One-step experiments, generally referred to as JBN experiments, must be avoided even if they are interpreted with Pc curves. Their interpretation is based on transient flow dominated by viscous fingering and/or channeling, which does not represent "true" pore-scale relative permeability.
- A more accurate experiment requires 7 to 10 steps: saturations become more uniform after the first step, and flows are then controlled by local Kr.
- Capillary end effect is not an artifact that should be removed but rather an advantage that allows exploration of all the range of saturations. Conducting Kr (or EOR) experiments at maximum speed as described in [14] is not a recommended solution. However, with standard displacement experiments, either SS or USS, the balance between capillary and viscous forces requires fluid velocities to be much higher than in reservoirs. An ideal experiment should be able to provide high capillary pressure with low flow rate. Solutions should be investigated using porous plate or centrifuge methods.
- Kr determination during experiments with capillary effects is only possible with numerical simulators. Numerical simulators are also useful to design the experiments.
- When a single fluid is injected (unsteady-state, USS), the range of saturation is controlled by the balance between viscous and capillary forces. Consequently, the experiment is difficult to design if the Pc curve is not well-known.

- Steady-state method allows a precise control of saturations. When two fluids are injected at high flow rates, saturation is close to be uniform on a large part of the plug, and its value is controlled by the ratio of viscous forces in the two fluids. This method can be used for any type of wettability. At low flow rate, the range of saturation is limited to a small interval around the saturation where Pc=0.
- Based on these observations, the recommended procedure is a compromise between SS and USS methods.
- We finally show how the Sor measured in laboratory by history matching may defer from the true reservoir Sor.

ACKNOWLEDGEMENT

We want to thank Jos Maas and Karl Sigurd Årland for providing authorizations to reproduce their figures and Fabrice Bauget for useful comments on the manuscript.

REFERENCES

1. Ayub, M. and R.G. Bentsen, "Interfacial viscous coupling: a myth or reality?", (1999), J. Petroleum Science and Engineering, Vol 23.
2. Lackner, A.S., O. Torsaeter, "Phase pressure measurements: simultaneous and direct derivation of relative permeability and dynamic capillary pressure", (2005), SCA2005-05.
3. Johnson, E.F., D.P. Bossler, and V.O. Naumann, “Calculation of Relative Permeability from Displacement Experiments”, Transactions AIME, 216, 1959, 370-372.
4. Kokkedee, J.A, W.Boom, A.M. Frens and J.G. Maas, "Improved Special Core Analysis: Scope for a reduced residual oil saturation", (1996), SCA9601.
5. Mohanty, K.K. and A.E. Miller, "Factors influencing unsteady relative permeability of a mixed-wet reservoir", (1988), SPE18292.
6. Fenwick, D., N. Doerler, and R. Lenormand, "The effect of heterogeneity on unsteady-state displacements", (2000), SCA2000-30.
7. Sarma, H.K., B.B. Maini and G. Allen, "Effect of viscous instability on unsteady-state relative permeability", (1992), Revue Institut Français du Pétrole, Vol. 47, Nov-Dec.
8. Lombard J.-M., P. Egermann and R. Lenormand, "Measurement of Capillary Pressure Curves at Reservoir Conditions", (2002), SCA 2002-09.
9. Lenormand R., P. Delaplace and P. Schmitz, "Can we really measure the relative permeabilities using the micropore membrane method", (1996), SCA9637.
10. Brown H. W., "Capillary pressure investigations", Petroleum Transactions, AIME, vol. 192, (1951), also SPE-951067-G.
11. Rose W. D., "Apparatus and procedure for relative permeability measurements", US patent number 4,506,542, 1985.
12. M. Fleury, P. Poulain and P. Egermann, "A new approach to derive relative permeability data while measuring resistivity index, SCA2005-04.
13. F. Bauget, S. Gautier, R. Lenormand and A. Samouillet, "Gas-liquid relative permeabilities from one-step and multi-step centrifuge experiments", (2012), SCA2012-13.
14. Masalmeh, S.K, "Determination of waterflooding residual oil saturation for mixed to oil-wet carbonate reservoir and its impact on EOR", (2013), SPE-165981-MS.

A NOVEL LABORATORY METHOD FOR DETERMINING CAPILLARY PRESSURE AND WETTABILITY WHILE MEASURING STEADY-STATE RELATIVE PERMEABILITY

Robin Gupta, Daniel Maloney, David Laverick, Robert Longoria, Larry Poore and Jeff Spitzenberger, ExxonMobil Upstream Research Company

This paper was prepared for presentation at the International Symposium of the Society of Core Analysts held in Snowmass, Colorado, USA, 21-26 August 2016

ABSTRACT

A novel laboratory method was developed that obtains relative permeability (k_r), capillary pressure (P_c), and wettability characteristics from a single reservoir-condition steady-state coreflood test. The method uses a modified inlet end-piece that isolates injection phases so that the difference between injection phase entry pressures is measured. Several inlet end-piece designs and related instrumentation are developed that can isolate and precisely capture the pressure difference of injection phases at the inlet. A method is developed to extract the capillary pressure from the difference in flowing injection phase pressures, which has both capillary and viscous pressure contributions. For this method, injected phase pressures are measured for several total flow rates for each steady-state fractional flow. This process enables quantification of P_c and k_r at each steady-state fractional flow condition. Rock wettability can be estimated from such measurements using either USBM or Amott-Harvey methods when the steady-state test includes both primary imbibition and secondary drainage cycles. Measured steady-state live-fluid coreflood data is used to illustrate this method of gaining both P_c and k_r functions from a single test. An excellent match was obtained between P_c quantified by the centrifuge method and the new method.

INTRODUCTION

Capillary pressure (Pc), relative permeability (kr) and wettability are key special core analysis (SCAL) characteristics used for reservoir performance predictions. Common practice is to measure these characteristics independently via several tests. Ideally, one would like to obtain all of these characteristics for a rock and fluid system from one test, saving time and cost. By doing so, a number of technical issues are avoided, such as mismatched data sets, anomalies from using different samples, test conditions, and fluids in the various tests, and propagation of errors from combining results from different tests.

When a sample (core plug or composite of core plugs) is mounted for a steady-state coreflood test, it is placed between inlet and outlet flow distribution end-pieces. The end-pieces serve as interfaces between the sample and upstream and downstream flow lines. During a two-phase steady-state flow measurement, two fluids are injected into and produced from the sample until steady-state is attained, that is, until saturation and

pressure drop across the length of the sample stabilize. The difference in phase pressures is close to zero at the outlet of the sample because of the capillary end-effect phenomenon (CEE). The difference between phase pressures is non-zero at the core inlet. From independent measures of injected phase pressures, one could conceptually determine capillary pressure as the difference between the non-wetting and wetting phase pressures. This is typically not practical because of phase mixing. This work addresses the mixing issue, enabling measures of phase pressures at the sample inlet face.

In a steady-state test, ability to measure differences in injection phase pressures at the sample inlet and to correct such measurements for viscous effects enables interpretation of capillary pressure. Thus, this work is an effort towards measuring relative permeability and capillary pressure curves on the same core plug (or first of a series of stacked plugs) simultaneously. Wettability can be calculated using established methods such as the Amott and the USBM (US Bureau of Mines) wettability index methods if both imbibition and secondary drainage capillary pressure cycles are available. Combining relative permeability, capillary pressure and wettability measurements into one test can yield a significant reduction in experimental time compared to measuring each separately.

Much of the previous work (for example, Longeron *et al.*, 1995; Richardson et al. 1952; Jennings *et al.*, 1988, Virnovsky *et al.*, 1995a, Virnovsky *et al.*, 1995b) relates to independent phase pressure measurements at the sample inlet using hydrophobic (oil-wet) and hydrophilic (water-wet) porous disks or membranes. For such approaches, properties of the disk or membrane allow pressure communication with one phase while the other phase is excluded. Drawbacks include the difficulty of initiating a reservoir-condition live fluid test without exceeding excluded-phase entry pressures of the porous disks or membranes, and uncertainty about whether or not the disk or membrane will perform as desired throughout the test. This work seeks to isolate the injection phases physically for phase pressure measurement rather than isolation via disks and membranes.

Authors including Richardson *et al.* (1952) and Gupta and Maloney (2015) suggested that capillary pressure may be quantified as the difference between non-wetting and wetting fluid phase pressures at the inlet. However, they did not account for the need to correct the viscous flow contribution to the pressure difference, which this work addresses. They also did not describe a practical inlet end-piece design to accomplish phase pressure measurements. Richardson *et al.* (1952) stated that the difference between non-wetting and wetting phase pressures at any point within porous media equals the capillary pressure corresponding to the saturation at that point. They demonstrated the concept by cementing gas (non-wetting) pressure probes to the rubber sleeve and oil (wetting phase) pressure probes made of ceramic porous media to core walls. Their experiments showed that the pressure difference between the non-wetting and wetting fluid phases inside the core is constant away from the outlet end and equals capillary pressure. Cementing probes on a sample is not a preferred approach because the practice might damage the sample or alter its wettability. Further, cementing probes for each test could be time intensive and susceptible to leaks.

Kokkedee (1994) and Pini (2013) proposed that capillary pressure is equal to pressure drop across the core at low rates. No special end-piece is required in this technique. However, this technique assumes that viscous forces are small compared to capillary forces, which may not be true in many test conditions. In this work, a method to correct viscous forces from inlet phase pressure is used to estimate capillary pressure.

APPARATUS DESIGN

Design elements of the proof of concept apparatus are shown in Diagram 1. In this design, end screens at the upstream face of the sample ordinarily used to promote mixing of injection phases are omitted. The inlet face of the sample is directly in contact with the inlet end-piece. To accurately measure difference in phase pressures at the inlet, two differential pressure transducers (high and low pressure ranges) are used in parallel, which can be engaged or disengaged depending upon the magnitude of the pressure difference. Pressures are also measured with Quartz absolute pressure transducers to provide redundancy. Pressure taps are placed as close as possible to the core holder inlet to minimize pressure drops from flow in the tubing and are placed at the same height to avoid gravity head differences. It is preferred to have check valves upstream of the inlet side pressure transducers to prevent back flow, which could result in phase mixing. As in a conventional flow system design, a differential pressure transducer or pair of Quartz absolute pressure transducers is used to measure pressure drop across the length of the sample. Pore pressure is maintained via closed-loop flow or by using a back pressure regulator (BPR). Overburden pressure is supplied by a pump.

INLET END-PIECE DESIGNS

Designing an inlet end-piece that is robust and prevents injection phase mixing at rock and end-piece junction is a challenging problem. Conventional inlet end-pieces have patterns that promote distribution of fluid phases. Examples of several conventional end-pieces are shown in Figure 1. Because test samples are porous, it is challenging to obtain a good seal between a metallic end-piece and a rock sample. Small scale irregularities on the rock surface and the smooth metal pattern on inlet end-pieces seal imperfectly, resulting in mixing of injected fluids and equilibration of their pressures. The challenge of obtaining a good seal and phase isolation exists even for a metal-based inlet end-piece with flow distribution patterns that do not intersect (Figure 1b and Figure 1c). To demonstrate this challenge, steady-state coreflood tests were performed on Cordova Cream limestone (7-9 mD) using helium gas and brine (20000 ppm) at room temperature, 1500 psi pore pressure, and 2400 psi net confining stress. Metal inlet end-pieces like those of Figure 1 were used. Capillary pressure was measured on a companion plug using the centrifuge method with the same net confining stress and temperature conditions. The modified flow apparatus, as discussed above, was used to perform this experiment. The steady-state coreflood was performed with multiple gas-water fractional flows. Pressure and saturation values were recorded at steady-state for each fractional flow. Figure 2 compares difference of inlet phase pressures for each fractional flow with centrifuge capillary pressure data. Clearly, no inlet phase pressure difference (ΔP) at steady-state conditions was measured when using a metal-based inlet end-piece, indicating phase

mixing at the inlet face of the sample. Similar results were observed from a repeat test using a screen between the inlet end-piece and core.

New end-piece designs were tested with the aim of finding a configuration that prevents phase mixing at the core inlet. New designs used machined metal end-pieces and elastomer seals. The metal is used to provide: 1) a desired pattern for fluid distribution, and 2) a rigid base for an elastomer seal that maintains structural integrity at high pressures. The elastomer in the design is used to seal between the inlet end-piece and sample surface to prevent phase mixing. The elastomer and metal/alloy needs to withstand test conditions. Examples of a few end-piece designs are shown in Figure 3.

Although the combination of metal and elastomer can prevent phase mixing, some designs perform better than others. For example, designs with small flow apertures like the O-ring design (Figure 3a) provide excellent sealing between the inlet end-piece and core face, but at the cost of significant additional viscous pressure contribution to the inlet phase pressure. This additional viscous pressure contribution can exceed capillary pressures. It comes from an enlarged region of high injection fluid saturation inside the core near the inlet. Figure 4 shows Cordova Cream limestone results of pressure difference of inlet phases from tests with the O-ring design and metal-based designs. In this test, steady-state was attained with multiple total flow rates for two helium fraction flows (0.5 and 0.8). The pressure difference of helium and brine were non-zero, clearly indicating that the O-ring end-piece provided a good seal. However, helium-brine pressure differences at the inlet were of large negative magnitude compared to centrifuge capillary pressures. This resulted from the additional viscous pressure contribution due to the O-ring design's small inlet aperture. With the O-ring design, phase saturations expanded in a hemispherical pattern inside the core at phase inlet ports. Since brine viscosity is almost two orders of magnitude higher than helium viscosity, the viscous pressure drop near the brine end-piece port is significant compared to that of the helium port. For this reason, the difference in helium-brine inlet pressures makes it seem that capillary pressure is negative in Figure 4. Typical measurement techniques for capillary pressure are performed with no flow and negligible viscous pressure gradients. In this test, the range of measured phase pressure differences match closely with Darcy equation calculations for hemispherical flow in porous media. To remedy this problem, it appeared desirable to have an elastomer-based inlet end-piece with wider flow aperture to reduce the viscous pressure contribution in measured inlet phase pressures.

The use of an elastomer seal that withstands test fluids and conditions is important. Some elastomers may perform well at room conditions, but may lose structural integrity in the presence of hydrocarbons at high pressure and temperature. An example is shown in Figure 5 in which a spiral elastomer pattern made using an incompatible material was destroyed when exposed to live crude oil and brine at high temperature and pressure.

Inlet end-piece patterns with metal and elastomer (e.g., Half-moons and Spiral with gasket in Figure 3) tend to perform better than those with only elastomer between the end-piece and sample (e.g., Elastomer spiral). Elastomers are more compressible

compared to metal. In a 100% elastomer based design, if grooves are not sufficiently deep or wide, there is a risk of pattern distortion under high pressure. During another test with Cordova Cream limestone outcrop at 1500 psi pore pressure and 2400 psi net confining stress, an Elastomer spiral pattern was able to isolate phases at the inlet for the first 4000 minutes (Figure 6), but later failed as evidenced by the reduction in inlet phase pressures to zero as a result of phase mixing. Figure 7 shows post-test pictures of the core and end-piece. The salt residue from brine spreading over most of the inlet end-piece face (Figure 7a) and the brine streak connecting positions of injection ports for both phases on the rock face (Figure 7b) provide clear evidence that fluids mixed at the core face and did not remain isolated. The risk of having the elastomer lose structural integrity under high pressure can be reduced if the end-piece is made of both elastomer and metal.

Based on the above discussion, a good inlet end-piece design contains: 1) a wider aperture or surface area for injection phases to minimize the viscous pressure contribution in measured inlet phase pressures, 2) compatible elastomer material, and 3) face design consisting of both metal and elastomer, or 100% elastomer with sufficient groove width and depth. Examples of such end-pieces are the Spiral with gasket (Figure 3c) and Half-moons (Figure 3d).

From a similar experiment on Cordova Cream limestone outcrop, the Half-moon inlet end-piece successfully isolated both brine and helium phases. Figure 8 shows the difference of phase pressures at steady-state for multiple fractional flows and multiple rates at each fractional flow. Clearly, phase pressure differences at the inlet are non-zero, indicating successful isolation of injection phases at the face of the inlet end-piece. Further, the differences between phase pressures at the inlet are positive, indicating lower viscous contributions to the measurements because of better phase spreading at the core plug face (or wide injection cross section) compared to results from an end-piece with small injection aperture, such as the O-ring design. Though viscous contributions with the Half-Moon design are relatively low, they are not zero, which reflects flow rate dependence in the difference between inlet phase pressures. Because of viscous gradient effects, the difference in inlet phase pressures is lower than the static capillary pressure measured by the centrifuge method in Figure 8. Thus, the viscous contribution must be subtracted from the difference in inlet phase pressures to achieve a measure of capillary pressure from a steady-state coreflood test.

VISCOUS PRESSURE CORRECTION

The difference between non-wetting and wetting phase pressures at the inlet equals P_c only at a static condition (zero flow rate). However, in a coreflood test (both steady-state and unsteady-state), one or both phases are continuously injected, and the phase pressures at the inlet result from both capillary and viscous forces. Hence, a method is required to estimate and correct the viscous pressure contribution from the difference of phase pressures at the inlet.

In a steady-state coreflood test, corrections for viscous pressure contributions can be determined by performing tests at multiple flow rates for each fractional flow. Steady-

state is achieved at each flow rate. For a given fractional flow, capillary pressure is equal to the intercept of the trend line from a plot of steady-state phase pressure difference at the inlet versus total flow rate (Figure 9). Close to the inlet, fluid saturation does not change significantly with flow rates. Hence, phase pressure difference at the inlet changes linearly with total flow rate for a typical steady-state fractional flow condition, and the intercept of the linear trend equals capillary pressure. The capillary pressure measured using the above method corresponds to the capillary end-effect corrected fluid saturation, which can be estimated using the Intercept Method (Gupta and Maloney, 2015) or through in-situ saturation monitoring. In tests with sufficiently high pressure drop across the core, the correction might be small and within experimental accuracy, and the average saturation across the core can be used.

APPLICATION EXAMPLE AT RESERVOIR CONDITIONS

A water-oil steady-state coreflood test was performed using one of the new inlet end-pieces to demonstrate the concept of obtaining capillary pressure from the difference of phase pressures (after viscous pressure correction) at the inlet. This test was performed on native state core plugs stacked in series to make a composite of 25 cm length. The test was performed at reservoir temperature and reservoir pore and overburden pressures using live fluids. Viscosities of oil and brine were similar. Pressure measurement devices were configured as in Diagram 1. The "Half-Moons" inlet end-piece was used (Figure 3d). The test was an imbibition steady-state test, beginning with a measurement of oil permeability at irreducible water saturation and continuing with oil and water co-injection in steps of decreasing oil fractional flow (F_o). For each F_o, after achieving steady-state conditions, total flow rate was increased several times. With the direction of total flow rate increasing, unwanted hysteresis is avoided. When F_o is decreased for the next set of steady-state measurements, flow rate can be reduced concurrently with the fractional flow change. Because the change in oil fractional flow coincides with an increase in brine saturation, the reduction of total flow rate between consecutive fractional flows avoids or reduces potential for inadvertently introducing hysteresis because of saturation reversals.

Figure 10 shows phase pressure difference (oil minus brine phase pressure) at the inlet and total flow rate versus time. As discussed above, reductions in total flow rate on Figure 10 coincide with changes in fraction flow. In Figure 10, the difference in phase pressures at the inlet is non-zero and ranges from -10 to +10 psi. The "Half-Moons" end-piece was able to clearly prevent phase mixing at the inlet face during this test.

In theory, the capillary pressure contribution to the difference between measured phase pressures is insensitive to total flow rate. In Figure 10, the phase pressure difference at the inlet changes with flow rate at each fraction flow. This flow rate dependence is the result of viscous rather than capillary phenomena. Figure 11 plots oil phase pressure minus brine phase pressure at the inlet versus total flow rate from steady-state measurements with oil fractional flows of 0.985, 0.9 and 0.3. All three plots show linear trends, as do plots for the other fractional flows that are not shown. Intercepts equal capillary pressure, while slopes are influenced by viscous effects. Slopes are positive for

oil fractional flows above 0.5 (because oil rates are greater than brine rates) and negative for fractional flows below 0.5 (because brine rates are greater than oil rates).

Constructing the capillary pressure curve for the rock at the inlet consists of plotting the intercepts (from the phase pressure difference versus rate plots) versus the corresponding brine saturations. Brine saturation was calculated by applying the Intercept method (Gupta and Maloney, 2015), which corrects the steady-state data for capillary end-effects. Since pressure drops in this test were high, capillary end-effect corrections to brine saturations were small. Figure 12 shows the resulting capillary pressure plot for this test. Saturations at the first and last points represent residual brine and residual oil saturations for this test. In theory, capillary pressure curves asymptote at residual saturations at both ends, but values of 11 psi and -15 psi were used to denote the capillary pressures at these residual saturations. This plot closely matches the centrifuge capillary pressure curves measured on preserved companion plugs of the same rock type (Figure 12), particularly with core sample C1. Figure 13 shows pore throat size distributions for the centrifuge core plugs (C1 to C4) and inlet-plug (S1) of the steady-state test. Clearly, plug C1 pore throat size and imbibition centrifuge capillary pressure data is closest to core plug S1 used in the steady-state test. The k_r curve obtained in this test closely matched with the curve obtained on samples with similar geology.

Overall, the new method is easy to implement and only requires minor modifications to a steady-state apparatus along with using a modified inlet end-piece. Even if an end-piece fails to prevent phase mixing during a test, quality steady-state relative permeability data is still obtained. However, this method has certain challenges. For example, the inlet end-piece design should be robust and needs to prevent phase mixing throughout the test, the test duration is slightly increased due to multiple flow rates performed for each fractional flow, and viscous pressure correction needs to be added to the test workflow. The application for a gas-liquid system is relatively more challenging compared to a liquid-liquid system because of low gas viscosity. A gas is more susceptible to leaks and phase mixing and generates relatively high viscosity pressure correction compared to a liquid.

CONCLUSION

Modified inlet end-pieces described in this work successfully isolated injected phases in a coreflood test, allowing measurement of inlet phase pressures. The inlet phase pressures at steady-state conditions were used to estimate capillary pressure of the core after applying viscous pressure corrections. If both imbibition and secondary drainage cycles are performed during a steady-state test, then capillary pressures as well as relative permeabilities can also be measured. Wettability of the core can be inferred from imbibition and secondary drainage capillary pressure curves using either Amott or USBM wettability index methods. Thus, using the described inlet end-piece designs and test methodology, relative permeability, capillary pressure and wettability of a core can be measured simultaneously in a single steady-state test, which may result in significant time and cost savings.

REFERENCES

1. Richardson, J. G., Kerver, J. K., Hafford, J. A. and Osoba, J. S. (1952, August 1). Laboratory Determination of Relative Permeability. Society of Petroleum Engineers. doi:10.2118/952187-G
2. Longeron, D., Hammervold, W. L. and Skjaeveland, S. M. (1995, January 1). Water-Oil Capillary Pressure and Wettability Measurements Using Micropore Membrane Technique. Society of Petroleum Engineers. doi:10.2118/30006-MS
3. Virnovsky, G.A., Guo, Y. and Skjaeveland, S.M. (1995a, May 15). Relative Permeability and Capillary Pressure Concurrently Determined from Steady - State Flow Experiments. 8th. European IOR - Symposium in Vienna, Austria
4. Virnovsky, G.A., Guo, Y., Skjaeveland, S.M. and Ingsoy, P (1995b, October). Steady-State Relative Permeability Measurements and Interpretation with Account for Capillary Effects. Society of Core Analysts Conference in San Francisco, USA
5. Gupta, R., and Maloney, D. R. (2015, December 1). Intercept Method--A Novel Technique To Correct Steady-State Relative Permeability Data for Capillary End Effects. Society of Petroleum Engineers. doi:10.2118/171797-PA
6. Kokkedee, J. A. (1994, January 1). Simultaneous Determination of Capillary Pressure and Relative Permeability of a Displaced Phase. Society of Petroleum Engineers. doi:10.2118/28827-MS
7. Pini, R., and Benson, S.M.. 2013. "Simultaneous Determination of Capillary Pressure and Relative Permeability Curves from Core-Flooding Experiments with Various Fluid Pairs." Water Resources Research 49 (6): 3516–30. doi: 10.1002/wrcr.20274

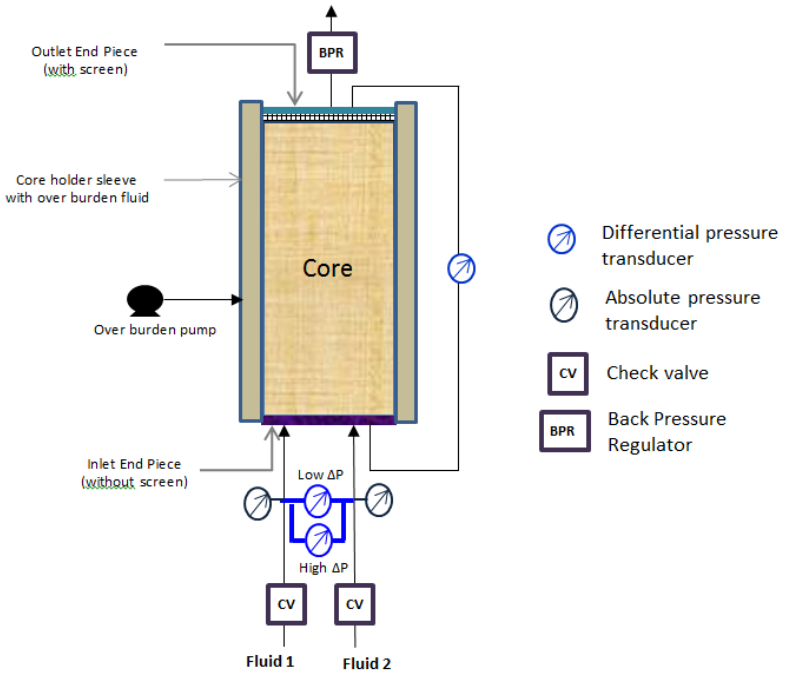

Diagram 1: Schematic of modified core holder assembly

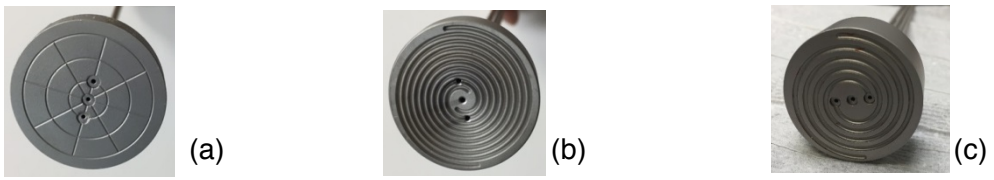

Figure 1: Examples of conventional inlet end-piece designs: (a) Cross, (b) Spiral, and (c) Modified spiral

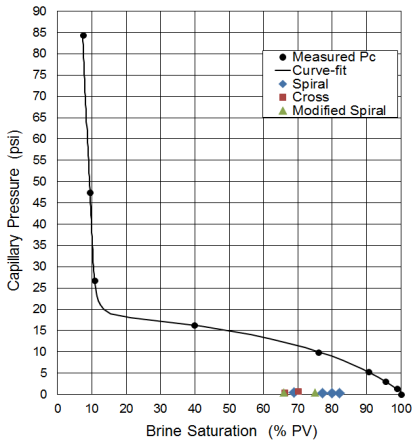

Figure 2: Difference of inlet phase pressure compared to measured capillary pressure for Cross, Spiral and Modified spiral inlet end-pieces

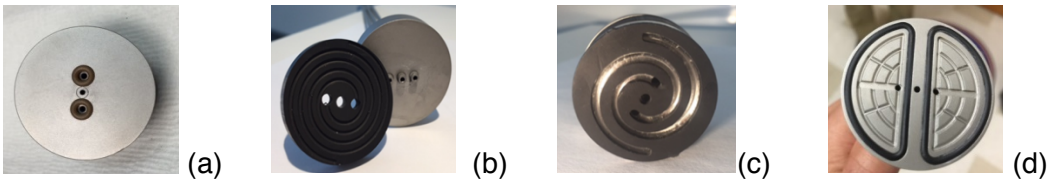

Figure 3: Examples of new elastomer based inlet end-piece designs, (a) O-ring, (b) Elastomer spiral, (c), Spiral with gasket, and (d) Half-moons

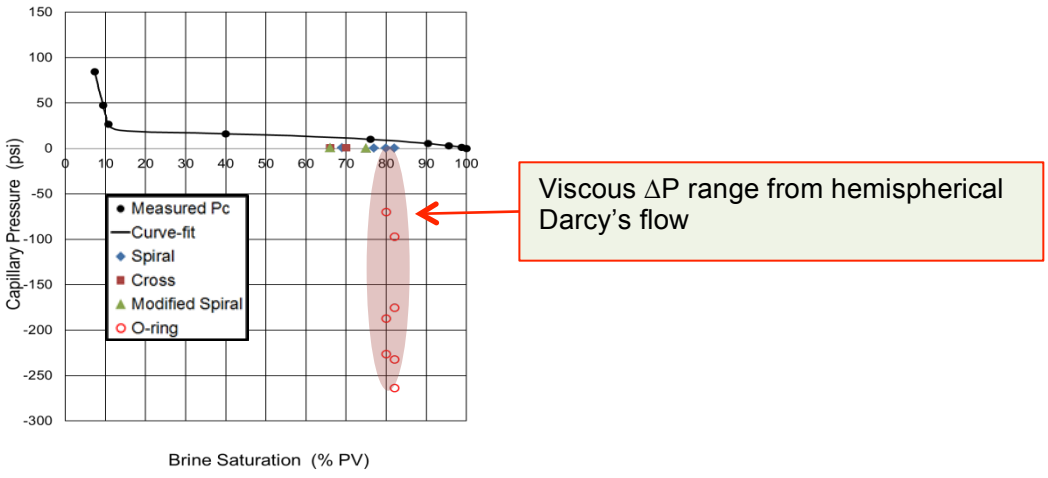

Figure 4: Difference of inlet phase pressure compared to measured capillary pressure for Cross, Spiral, Modified spiral and O-ring inlet end-pieces

Figure 5: Spiral with gasket end-piece after exposure to live crude oil at high pressure and temperature. Incompatible material was used in this test.

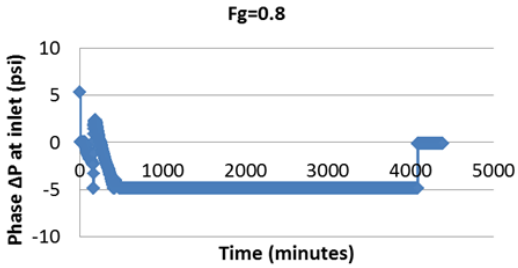

Figure 6: Plot of difference in inlet phase pressures with time for helium-brine steady-state test with Elastomer spiral inlet end-piece

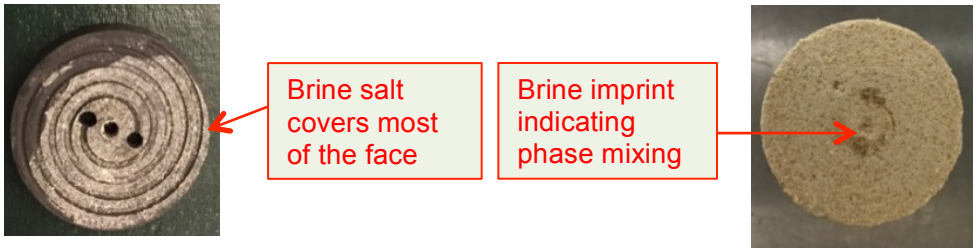

Figure 7: Pictures taken after the test for, (a) face of Elastomer spiral inlet end-piece, and (b) face of the core at the inlet side

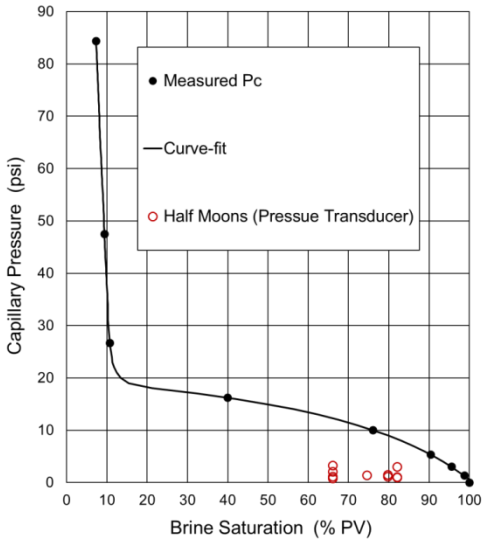

Figure 8: Difference of inlet phase pressures from Half-Moons end-piece compared to measured capillary pressure

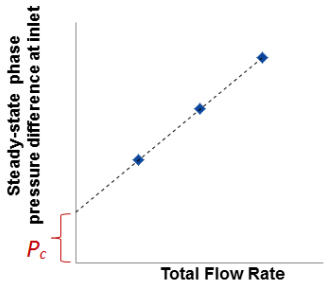

Figure 9: Plot of steady-state phase pressure difference at inlet with total flow rate for a given fractional flow. The intercept of the trend line of this plot equals static capillary pressure.

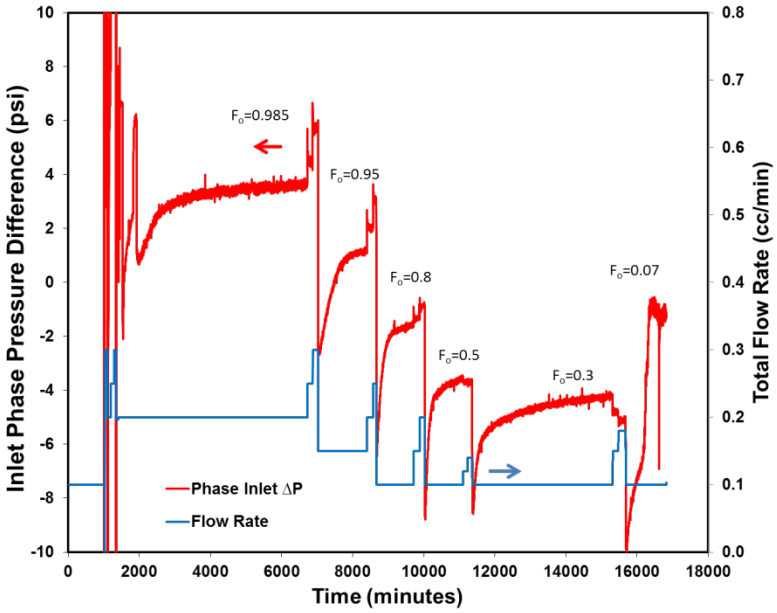

Figure 10: Difference in phase pressure at inlet and total flow rate with time at different oil fractional flow (Fo)

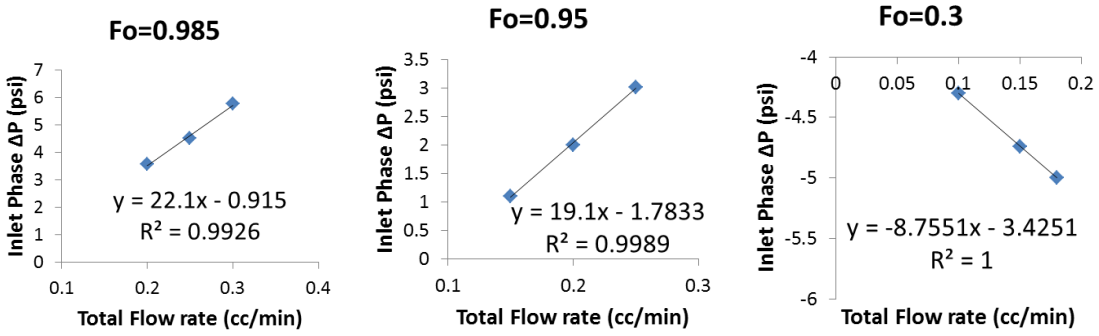

Figure 11: Plot of inlet phase pressure difference at steady-state condition with total flow rate for oil fractional flows of 0.985, 0.95 and 0.3. All three plots have linear trends. Intercepts equal capillary pressures.

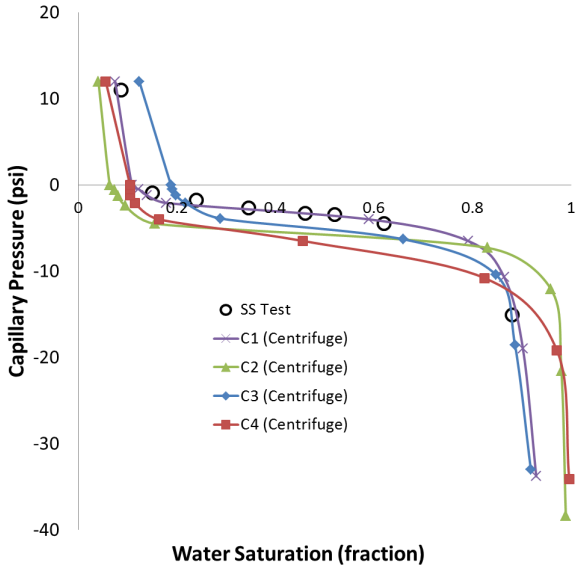

Figure 12: Capillary pressure curve obtained using the new method and compared with centrifuge capillary pressure measured on preserved plugs (C1 -C4) of the same rock type

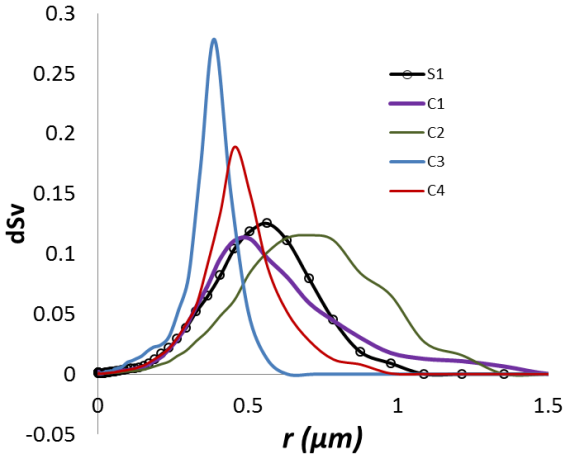

Figure 13: Pore throat size distribution for the inlet core plug used in the steady-state test and the four core plugs for same rock type used in the centrifuge capillary pressure test

SCAL FOR GAS RESERVOIRS: A CONTRIBUTION FOR BETTER EXPERIMENTS

Arjen Cense[1], Jules Reed[2], Patrick Egermann[3]
[1]A/S Norske Shell, [2]LR Senergy, [3]Storengy (ENGIE)

This paper was prepared for presentation at the International Symposium of the Society of Core Analysts held in Snowmass, Colorado, USA, 21-26 August 2016

ABSTRACT

Special core analysis for gas fields requires a different approach than for oil fields. Gas fields are mostly produced via pressure depletion. Saturation changes are not large during this process, except if water is flooding (parts of) the reservoir. Gas reservoirs are mostly water wet, which is, from a SCAL point of view and from a reservoir simulation point of view, a significant simplification compared to oil fields, where wettability is often a big uncertainty and has significant impact on the shape of the (imbibition) capillary pressure and relative permeability curves. However, although the required SCAL input for reservoir simulation may seem to be relatively simple, the design and do-ability of the SCAL experiments in the lab is challenging, due to compressibility and solubility effects of gas. In this paper, we discuss what laboratory experiments are appropriate for gas fields and how they should be performed to obtain maximum value. We discuss what the uncertainties in these experiments are and how uncertainties can be reduced.

INTRODUCTION

With the current low oil prices and the focus to reduce cost, investments in gas projects are becoming more attractive. The price of gas has not dropped nearly as much as that of oil, which makes gas producing fields economically more stable. In addition, at the last climate change summit in Paris, it was decided by leaders of 195 nations that they will cut their carbon emissions. Since gas emits lower carbon emissions than coal and crude, gas producing fields are potential candidates to decrease the pace of global warming until we can rely on renewable energy sources.

When a natural gas field is discovered, the initial distribution of gas can often be inferred from the primary drainage capillary pressure curves, from which the saturation height function, i.e. gas saturation as a function of height-above-free-water-level (HAFWL), can be established. If the water level has moved pre-production, because of a (temporary) breach in the seal or because of a hydrodynamic (flowing) aquifer, we need to use the imbibition capillary pressure curves to describe those parts of the reservoir where water has displaced gas, and where gas has become residual or trapped (Figure 1).

Most natural gas fields are produced by depletion, meaning that wells produce gas by lowering the reservoir pore pressure, until production becomes uneconomic. Gas reservoirs are generally water wet, as the rock has not been in contact with wettability altering hydrocarbon components such as resins and asphaltenes. The processes at play

during reservoir production are simple: saturations hardly change and gas is flowing at initial (or connate) water saturation. The gas relative permeability is determined as the endpoint gas relative permeability ($k_{rg}(S_{wi}$ or $S_{wc})$ - green point in Figure 2). The water is still immobile, hence water relative permeability is zero.

In cases where a (strong) aquifer is present, the aquifer will invade during pressure depletion (depicted by orange arrows in Figure 1). The water from the aquifer then displaces the gas to its endpoint (yellow point in Figure 2), while the gas becomes trapped at residual gas saturation (S_{gr}). We generally see that pressures in gas reservoir models are mostly sensitive to $k_{rg}(S_{wi})$. Ultimate recovery appears less sensitive to $k_{rg}(S_{wi})$, but is more a function of S_{gr} and the endpoint water relative permeability, $k_{rw}(S_{gr})$. The shape of the relative permeability curves (e.g. gas and water Corey) are considered to be less important.

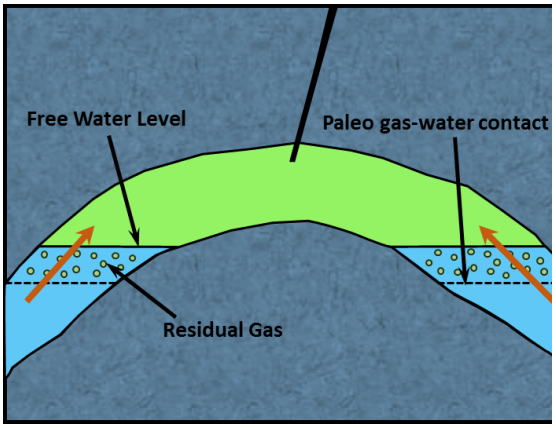

Figure 1: Schematic picture of gas reservoir with one producing well

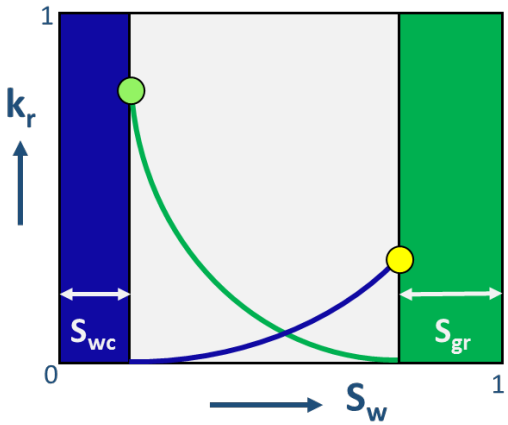

Figure 2: Relative permeability as function of water saturation

PITFALLS

Capillary Pressure

Generally speaking, the capillary pressure (Pc) curves are important to acquire because they have implications on both the volume of hydrocarbon in place and the sweep efficiency in the case of an active aquifer.

Gas In Place (GIP): the drainage Pc curves are usually the most relevant to evaluate the GIP, accounting for the transition zone especially for low-medium permeability range reservoirs. Nevertheless, for some reservoirs, the current Free Water Level (FWL) identified from the gas-brine pressure gradients can be different from the one prevailing several millions years before which is often referred to as paleo contact. In the situation where the paleo contact was shallower than the current contact, the system is still under gas filling process and therefore the drainage mode is still the relevant one (gas saturation increase). In the opposite situation, a paleo contact located deeper than the current contact means that the whole system has experienced a major imbibition process. It is therefore important to keep in mind that drainage Pc curves are not always the relevant curves for

GIP evaluation. There are two types of information that can provide indications about the possible paleo contact:

- non-zero gas saturation below the FWL, from pressure gradient measurements, indicating gas saturation values typically in the trapped gas saturation range (20-40%).
- gas saturation in the transition zone not properly reproducible by a drainage J-function.

An illustration of such paleo contact data is provided in Figure 3. In this case, a strong deviation from the drainage J-function trend was clearly observed in a depth window up to 12 ft above the FWL (left plot). Above this depth, the deviation between imbibition and drainage curves is narrower, in the asymptotic part (right plot) of the Pc curve. In this case, the transition zone impact was of limited extent because of favorable permeability, but it can lead to much more pronounced deviation for lower permeability reservoirs. For flat and extended reservoirs, the volume impact of using a drainage instead of an imbibition curve can be huge, because of this saturation difference in the transition zone. Furthermore, the amount of gas trapped in the residual gas zone, below the present day free water level, will still be influenced by depletion of reservoir pressure and hence, will provide energy to the producing reservoir, via either the brine phase or the gas phase. The residual gas bubbles will expand upon depletion and once a connected path flow is established, the gas will reconnect with the 'free' gas in the reservoir.

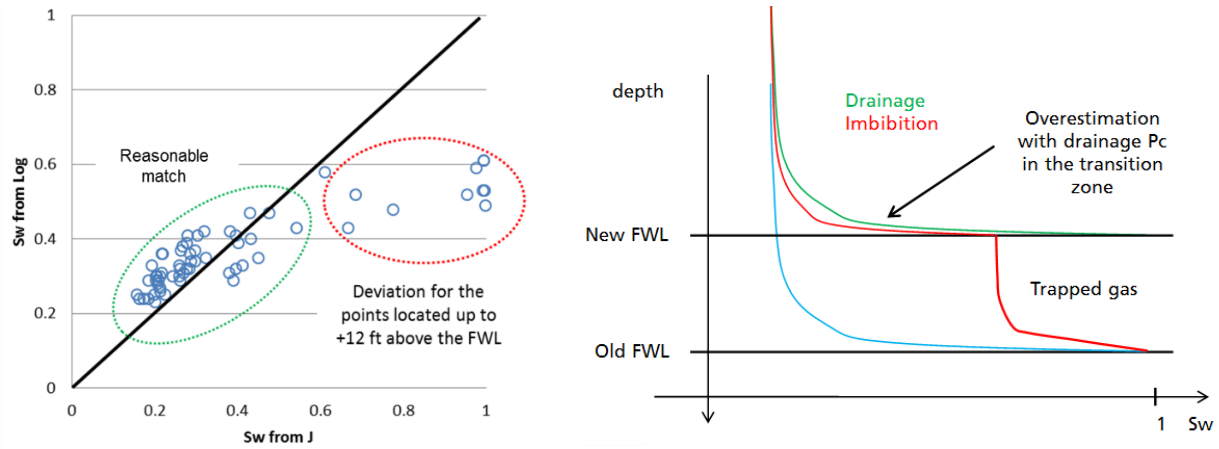

Figure 3: Example of paleo contact detected from a deviation of the saturation behavior in the transition zone

Sweep efficiency: because gas-water systems are always strongly water-wet and displacement is piston-like, the shape of Pc imbibition curve has little impact on the waterflood behavior, in terms of breakthrough time and pressure, except for the S_{gr} endpoint value. At (very) low injection rates, the core may spontaneously imbibe water, leading to negative pressure drops across the core.

In both cases, a preliminary estimate of the imbibition Pc curve can be obtained by rescaling the drainage curve between S_{wi} and S_{gr} as soon as the S_{gr} value is consistent (see next section). It is possible to infer the drainage curve by deriving the J-functions through

various standard techniques: HPMI (High Pressure Mercury Injection), centrifuge or porous plate.

In all the cases, the Pc curves to use for reservoir conditions purposes must account for both stress and interfacial tension using the Leverett formalism. Specific additional experiments are usually required like permeability-porosity as a function of stress and IFT data using either direct values from the pendant - ascending drop technique or estimates from PVT calculation, if the full gas and oil compositions are known. Among the 3 Pc techniques, porous plate is the only one to obtain direct relevant drainage Pc curves, if the experiments are conducted under full reservoir conditions. Usually the 3 approaches compare reasonably well for conventional gas-liquid reservoir systems: permeability > several mD (Sabatier, 1994) and the HPMI - centrifuge corrected curves can often be considered as a fair estimate whilst awaiting the porous plate results, which can take several months.

Residual Gas Saturation: S_{gr} is one of the most important parameters to acquire for an imbibition liquid-gas scenario, because it controls both the final saturation state and the dynamic behavior, since the displacement is piston-like (hence S_{gr} affects the breakthrough time). Representative S_{gr} values may be acquired from coreflood experiments conducted under stress, with some pore pressure to limit gas compressibility effects (see section on relative permeability endpoints). S_{gr} can be calculated by simple material balance (volumetric or gravimetric) and/or direct measurements using *in-situ* saturation monitoring (ISSM), which gives the added bonus of observing saturation as a function of sample length; although, uncertainties can be as high as several saturation units (s.u.), especially at reservoir conditions (Cense *et al.*, 2014). In general, S_{gr} values range between 20 and 40 s.u., where such inaccuracy can lead to errors typically in the range of 3% original GIP. It is therefore of primary importance to use several approaches for QC evaluations.

Firstly, include a compressibility test in the protocol after imbibition, in order to directly evaluate the remaining gas volume in the sample. Close the sample outlet and inject the imbibition test liquid until a predetermined pressure is achieved. Since pressure increase is linked directly to gas compression, induced by the liquid volume increase, it enables determination of the gas volume in place using the perfect or real gas law, dependent upon the fluid system.

$$P^{test}\left(V_{gas}^{ini} - V_{liq}^{inj}\right) = P^{ini}\,V_{gas}^{ini} \qquad V_{gas}^{ini} = \frac{P^{test}\,V_{liq}^{inj}}{(P^{test} - P^{ini})} \qquad S_{gr} = \frac{V_{gas}^{ini}}{PV}$$

With P^{ini} and P^{test} respectively, the initial pressure and stabilized pressure after injection, V_{gas}^{ini} the initial gas volume (prior to compressibility test), V_{liq}^{inj} the volume of liquid injected and PV the pore volume. This simple technique can give an additional and independent evaluation of S_{gr} very rapidly after the experiment.

Secondly, compare the results with published compilations of S_{gr}^{M} (maximum S_{gr} obtained with S_{wi} equal to 0) acquired from various samples (Suzanne, 2003; Pentland, 2010). As S_{gr} must be compared with SgrM, the Land equation (1971) can be used for the conversion, using default values of the Land constant according to the rock type (Irwin and Baticky, 1997).

Thirdly, conduct a large number of ambient conditions S_{gr}^{M} experiments in parallel to the few imbibition coreflood experiments planned. These experiments are simple, fast and relatively cheap to conduct. Clean samples are dried at 60°C and weighed. Immerse individual samples in a beaker of brine for roughly one hour for standard permeability (longer times may begin to introduce artefacts linked to gas dissolution, (Suzanne, 2003)). Alternatively, monitor immersed weight as a function of time, to the point of inflexion. After imbibition, take the samples from the beaker, remove superficial water and weigh. S_{gr}^{M} is calculated as the weight difference from dry state.

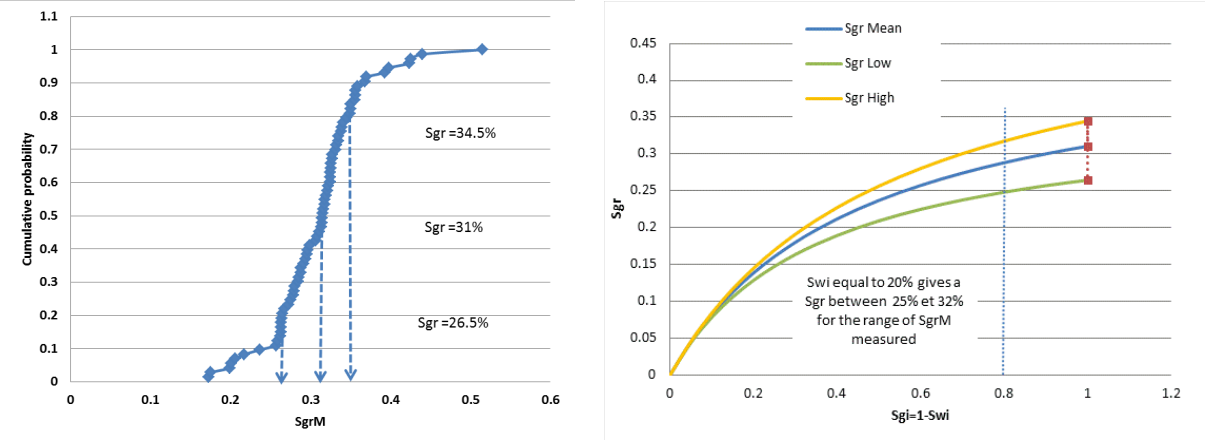

Figure 4: Probability curve of S_{gr}^{M} obtained from 73 measurements (left) and derived S_{gr} values using Land (1971)

An example of this approach is provided in Figure 4 (above), where an S_{gr}^{M} cumulative probability curve was obtained from 73 measurements on the same facies. It enabled definition of P50 and the associated variability. Using the Land equation (Land, 1971) and a representative S_{wi} value (20% considered in this example), it was possible to derive the range of expected S_{gr} values and to compare them with those obtained during the coreflood experiments. Another benefit of this approach is that the cumulative probability curve can be used to define the range of variation of the S_{gr} parameter, if the reservoir model is history matched through an automatic process.

The Brooks & Corey formalism (1966) is very attractive in the case of gas-liquid systems, since there is no ambiguity about the wettability. Drainage Pc data (mercury injection, centrifuge or porous plate) are first matched using the parametric law:

$$\left(\frac{P_d}{P_c}\right)^{\lambda} = \frac{S_w - S_r}{100 - S_r} = S_w^*$$

where P_d is the threshold pressure, λ rules the shape of the curve and represents the throat size distribution, S_r is the residual saturation. Once matched, the drainage gas-liquid relative permeability curves can be deduced in a straightforward manner using the following formulae:

$$K_{rw} = (S_w^*)^{\frac{2+3\lambda}{\lambda}} \quad and \quad K_{rnw} = (1-S_w^*)^2(1-S_w^{*\frac{2+\lambda}{\lambda}})$$

Although not reported explicitly in the literature, the Brooks and Corey approach (1966) can be easily applied to analyze imbibition data just by coupling the non-wetting phase trapping formula introduced by Land (1971) with a Carlson type hysteresis model (Carlson, 1981). For KrgI (imbibition), we use the above equation for drainage (D) in parallel with $K_{rg}I(S_g) = K_{rg}D(S_{gf})$, S_{gf} being the free gas saturation given from Land equation through the relation $S_{gf} = \frac{1}{2}\left[(S_g - S_{gr}) + \sqrt{(S_g - S_{gr})^2 - \frac{4}{C}(S_g - S_{gr})}\right]$

The Land formula must be calibrated to obtain the C constant representative of the facies under concern, where: $\frac{1}{S_{gr}} - \frac{1}{S_{gi}} = C$

Once calibrated (C, S_{wi} and λ), it is possible to assess the imbibition relative permeability curves and especially the endpoints. Figure 5 shows an example of qualitative QC using this approach on the endpoints of gas-brine relative permeability data. The blue and red curves provide the range of the expected $K_{rw}@S_{wi}$ and $K_{rg}@S_{gr}$ values, respectively. In this case, several outliers can be easily detected for further analysis of the raw data and interpretation.

Another practical approach is to compare relative permeability data from independent techniques. When Pc data are obtained from centrifuge, for example, it is recommended to spend some extra time to interpret the relative permeability curve of the displaced fluid in order to compare it with the one obtained from displacement technique (SS or USS). Where good agreement is observed, it adds confidence to the shape of the relative permeability curves, especially at late saturation, as depicted by the example provided in Figure 5 (right).

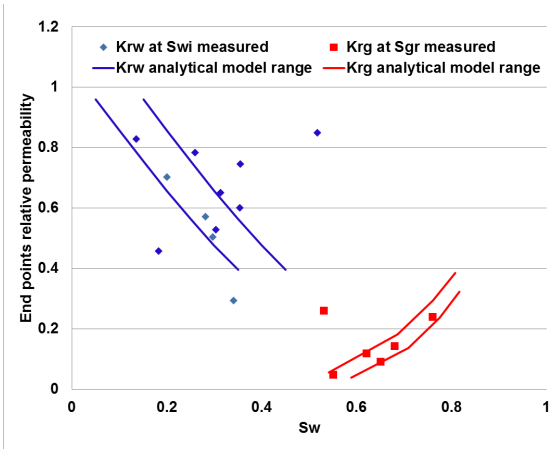

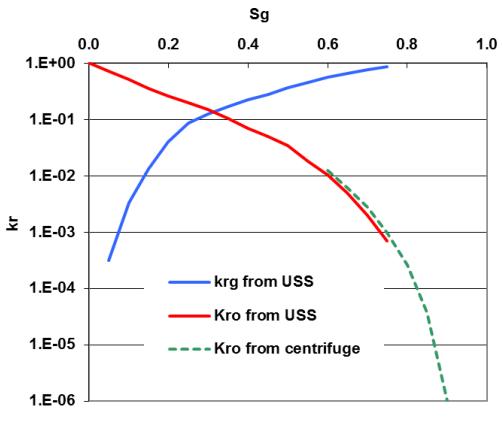

Figure 5: Quality control of endpoint relative permeability using Brooks and Corey type approach (1966) (left) – comparison between USS and centrifuge data for QC purpose (right)

Low Rate Waterflooding – Unsteady State

Bull *et al.*, 2011 presented data indicating that S_{gr} was a function of injection rate and recommended that residual gas measurements be performed at elevated or reservoir pressure to minimize gas compression and diffusion effects. However, many laboratories continue to perform analyses with little consideration of the implications of injection rate, compressibility and disequilibria (i.e. gas and water are not in full equilibrium due to pressure differentials required for flooding). Pore pressure for these tests in commercial labs, is often between 200-300 psi (15-20 bar) because of the pressure limitations of the graduated glass separators used to measure volumetric changes of the fluids. ISSM is always recommended as a secondary, verifying measurement method.

A number of unsteady state waterflood displacements to S_{gr} were reviewed. Pore pressures were 200 psi for all samples. Water injection rates varied from 0.5-4 ml/min, with little correlation to core properties. Figure 6 is a plot of permeability (normalized for area and length) against flow rates employed by a single lab during two projects from the same field, indicating the diversity and ill-considered rates employed. Figure 7 depicts a plot of S_{gr} versus water differential pressure (DP) after breakthrough for these samples. There is an obvious decline in residual gas saturation once DP exceeded 10 psi (5% of the applied pore pressure). This data confirms recommendations to limit differential pressure as a function of applied pore pressure (McPhee *et al.*, 2015), though the book states a more stringent limit of 2% pore pressure.

Low rate flooding experiments are performed to obtain S_{gr} values for cores initialized at representative S_{wi} (by porous plate or by centrifuge). When performing a waterflood on a gas filled core at S_{wi}, the gas volume produced equals the water volume injected until breakthrough. At breakthrough, gas saturation is observed to be residual throughout the core, and thus, no further gas production is expected after breakthrough.

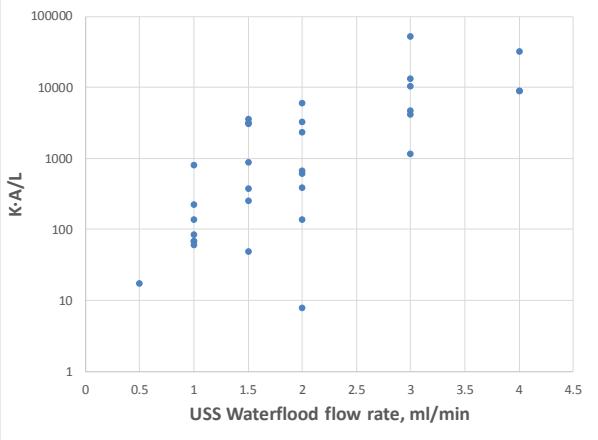

Figure 6: Permeability (normalized for Area & Length) versus Lab applied flow rates.

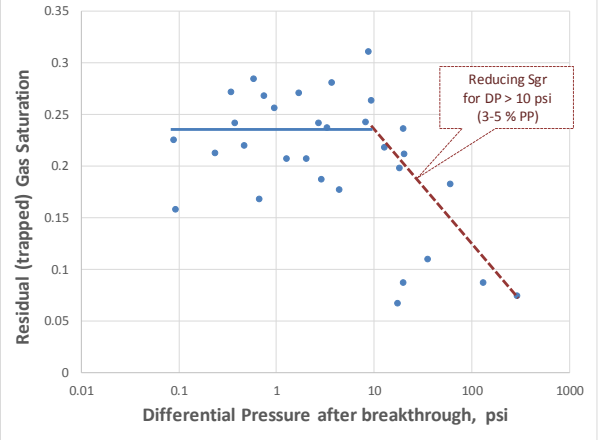

Figure 7: Sgr versus DP measured during post-breakthrough waterflooding

However, in some experiments, gas production continued after breakthrough. Plotting gas production as a function of brine pore volumes injected (PVI), an average (4 experiments) 2.9 ml additional gas was produced after approximately 30 PVI (ca. 400 ml) of brine after breakthrough (see Figure 8 (left)). Gas production was confirmed by ISSM. At breakthrough, the profiles were flat, i.e. the water saturation in the core is constant. After flooding multiple pore volumes, the water saturation has increased throughout the core, but more at the inlet than at the outlet.

Once brine is injected in the core, the pressure increases from 20 bar (back pressure of the whole system) to an injection pressure between 20.01 and 20.08 bar (differential pressure of 0.01-0.08 bar). Due to the higher inlet pressure, more nitrogen can be dissolved in the brine. The dissolved nitrogen will be evolved downstream of the core as pressure drops towards 20 bar again. It will either be trapped as residual gas, or surplus gas will be produced by viscous forces of the flowing brine.

In an attempt to quantifying this effect, an average pressure increase of 0.04 bar (4000 Pa) was assumed. The increased pressure leads to a concentration change of 4000 Pa / ($155 \cdot 10^6$ Pa / (mol/l) [Wilhelm et al. (1977)] = $2.58 \cdot 10^{-5}$ mmol/l. The amount of nitrogen lost during 400 ml of brine flushing through, at the inlet of the core is $1.03 \cdot 10^{-5}$ mmol, at room temperature and 20 bar pressure $1.3 \cdot 10^{-5}$ ml of nitrogen. This volume loss is orders of magnitude lower than the observed loss of 2.9 ml of nitrogen.

Another effect contributing to the gas stripping at the inlet happens when small amounts of gas are dissolved in the by-passing brine, which is under saturated: the size of the trapped gas bubbles is reduced, and as a consequence the local capillary pressure increases as the capillary pressure is proportional to the local curvature of the gas bubbles. This increases the local gas pressure and leads to gas dissolution, further decreasing the bubble size.

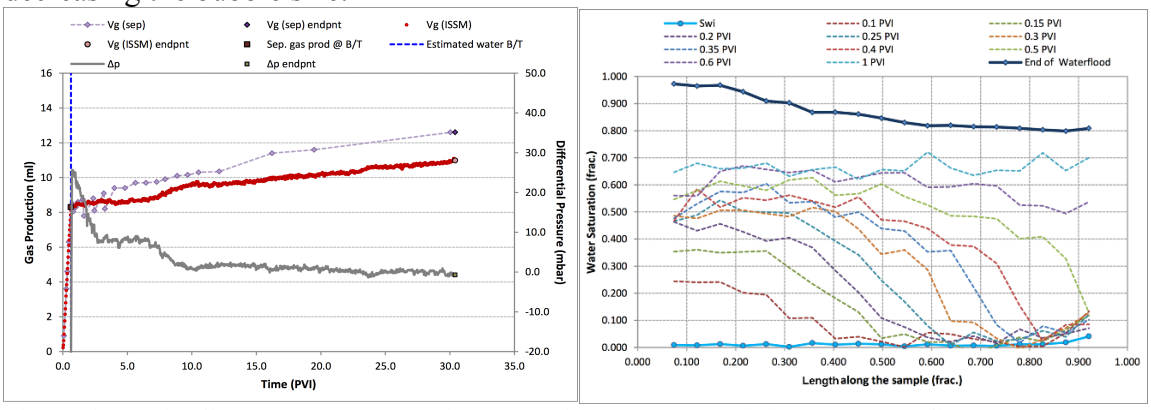

Figure 8: (Left) Gas production as a function of pore volumes injected (PVI). Gas production was measured using gamma ray (red line) & separator (dotted purple line). Pressure drop across the core in grey. (Right) Water saturation as a function of distance from inlet. Flooding from left to right.

In these experiments, the brine-nitrogen system was equilibrated for 24 hours by bubbling the nitrogen through the brine and the pore pressure was 100 bar. In another experiment, where the pore pressure was 5 bar and the equilibration time was 18 days, we did not observe any production of gas after breakthrough, which leads to the conclusion that 24 hours is not long enough to equilibrate nitrogen and brine from atmospheric pressure to 20 bar.

The tail end production of gas is thus considered to be an experimental artifact. The residual gas saturation representative for the reservoir is the residual gas saturation at breakthrough. It is our recommendation that USS waterfloods be performed at equivalent reservoir advancement rates (if the DP limits allow, else lower rates may be required), at limited differential pressure (max 5% of pore pressure) and for a limited injection volume, maximum 2 PVI.

Steady State Waterflooding

Steady state water displacing gas experiments are not generally recommended as a method to acquire imbibition water-gas relative permeability data; unless one is aware of the limited saturation range expected from these analyses and of the potential saturation inaccuracies because of disequilibria effects, or unless one has access to appropriate equipment and expertise, together with sufficient time and budget.

Figure 9 provides two plots from an imbibition water-gas steady state relative permeability test. These plots depict the correlation between anomalous, non-uniform saturation profiles (left) and differential pressures measured during each fractional flow rate of the test (right), plotted as a function of pore volumes water injected (PVI). Water saturation begins from S_{wi} = 0.163 and increases to S_w = 0.505 during the first fractional water flow (f_w=0.003). This is an increase of 34.5 saturation units (s.u.) at a very low fractional flow rate and represents one of the lowest viable fractional rates for most commercial laboratories (equipment and time limitations). Saturation is relatively uniform after this first fractional rate, and after the subsequent two fractions. However, after f_w=0.201, where DP increases above 10 psi, and above 5% pore pressure, a significant decreasing saturation gradient is observed from injection to production face (0 to 1 fractional length). The gradient increases during the next two fractional flow rates because of increased DP and greater water throughput. This results in inaccurate saturation data for the last three fractions and a poorly defined relative permeability saturation range, which defeats the purpose of the steady state method, since a major objective is to define a wider relative permeability saturation range than obtained by the unsteady state method.

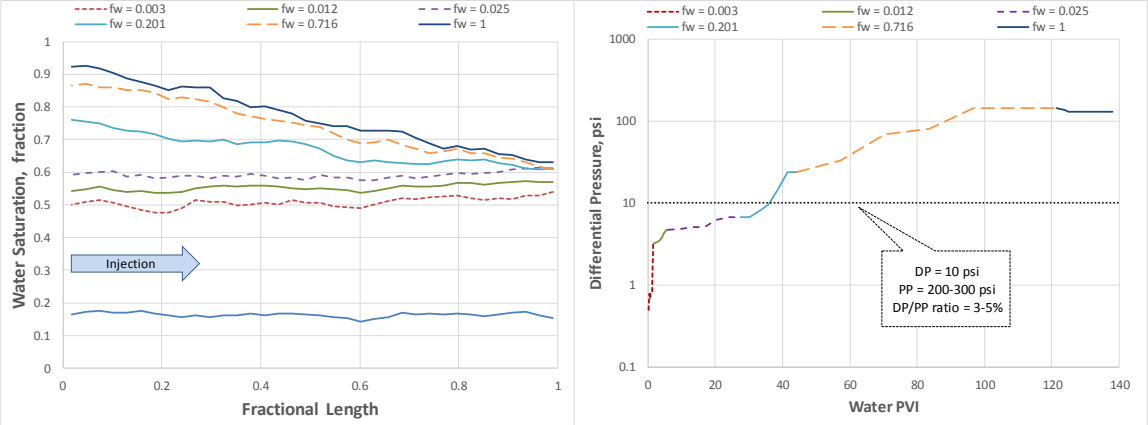

Figure 9: DP versus water PVI during an imbibition steady state waterflood (left). Resultant ISSM profiles during this experiment, depicting disequilibria effects at the sample injection face.

The analyses are controlled strongly by imbibition capillary pressures, resulting in the observed large encroachment of water saturation at very low fractional water flow rates. The large saturation increase is unavoidable. Fractional flow rates require to be some orders of magnitude lower, which would require either, ultra-low water flow rates (hence extremely long experimental times), or higher total injection rates (requiring very high gas injection rates, which risk extending into turbulent flow regimes).

Simulations of these steady state experiments were performed in an attempt to determine potential experimental parameters that might provide reasonable results within the limitations described earlier for standard commercial laboratory equipment, at ambient temperature and pore pressures of approximately 300 psi (20 bar).

Corey functions of N_g=2, N_w=5, endpoint k_{rw}=0.1 and S_{gr}=0.25 were used together with imbibition Pc data, modified from MICP curves, for a sample permeability range from 1-100 mD. Simulation using an initial fractional flow rate of f_w=0.0001, approximately a magnitude lower than the SS experimental data above, resulted in the saturation profiles given in Figure 10, for the 100 mD case. In this case, there was still a significant saturation change (over 35 s.u.) during that first, low f_w step. The first f_w step was estimated to require approximately 10 days to stabilize. A further, magnitude-lower f_w was estimated to require over 30 days to stabilize during the first f_w. Such stabilization times are uneconomical for both laboratory and client company, hence unfeasible. It was also noted that saturation after subsequent f_w steps was observed, at best, to cover a 25 s.u. range.

In addition to these undesirable saturation changes, the high throughput volumes required during a steady state test lead to a greater potential for disequilibria effects. Initially, at low f_w, differential pressure is low because gas viscosity is the main flowing phase; however, as f_w increases, DP will increase and may exceed the DP limits described above. This may be regulated by decreasing the total injection rate at each increasing f_w.

It is therefore recommended that, if employing gas-liquid SS testing (given the inherent issues), DP should be minimized in this manner.

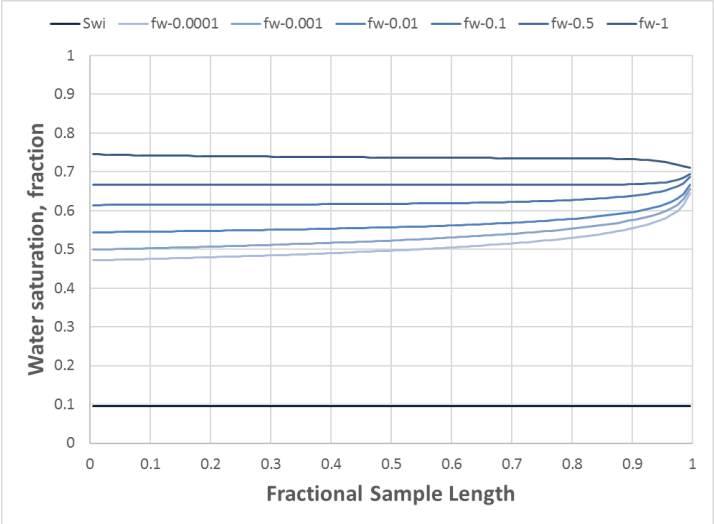

Figure 10: Example of simulated saturation profiles for SS water-gas relative permeability

CONCLUSIONS

In this paper we have discussed common pitfalls that may arise when conducting gas water SCAL experiments. The difference between drainage and imbibition processes can lead to an evaluation of too low gas saturation in place. This may be determined if there is no match between log saturations and those inferred from drainage models or if there is a deviation from J-function saturations. The porous plate technique is recommended as it can measure the Pc curves at full reservoir conditions. However, mercury-air or centrifuge measurements are much quicker to perform, and give reasonably reliable data.

It is recommended to use reservoir equivalent advancement rates (low rate) for corefloods to S_{gr}. Fluid equilibration time, between gas and brine, is important prior to conducting flooding experiments. It is recommended to limit differential pressures during low rate corefloods, and limit injection to two pore volumes. It is recommended to compare and quality control S_{gr} from (low rate) coreflood experiments, using ISSM, other volumetric methods, and published and measured values for S_{gr}^{M}. Relative permeability endpoints should be checked for outliers using an analytical approach that helps in determining confidence intervals.

Water-gas imbibition steady state experiments are not recommended when using the limited equipment of most commercial laboratories, unless one is aware of the limitations and cost implications of performing these tests, or one has equipment and expertise appropriate to acquiring these data.

REFERENCES

1. Brooks, R. H. and Corey, A. T.: "Properties of Porous Media Affecting Fluid Flow", J. Irrig. Drain. Div., (1966), 6, 61.
2. Land, C.: “Comparison of Calculated with Experimental Imbibition Relative Permeability”, Society of Petroleum Engineers Journal, vol. 11, no. 4, pp. 419-425, 1971.
3. Pentland, C.H.: “Measurements of Non-Wetting Phase Trapping in Porous Media”, PhD, Imperial College, November 2010.
4. Sabatier, L.: “Comparative study of drainage capillary pressure measurements using different techniques and for different fluid systems”, SCA-9424.
5. Suzanne, K.: “Evaluation of the trapped gas saturation in water-wet sandstones – Influence of the rock properties and the initial saturation state”, PhD, Ecole des Mines de Paris, February 2003.
6. Honarpour, M. and Mahmood, S.M.: “Relative permeability measurements: an overview”, Journal of Petroleum Technology (1988), SPE 18565.
7. Jerauld, G.R.: “Prudhoe Bay Gas/Oil Relative Permeability”, SPE Reservoir Engineering, 1997
8. Cense, A.W., van der Linde, H.A., Brussee, N., Beljaars, J., Schwing, A.: “How reliable is in situ saturation monitoring (ISSM) using X-ray?”, SCA-2014-09.
9. Wilhelm, E., Battino, R., Wilcock, R.J.: “Low-pressure solubility of gases in liquid water.” J Chem. Rev., **77**, 219–262, 1977.
10. Goodman, J.B., Krase, N.W.: “Solubility of Nitrogen in Water at High Pressures and Temperatures” Industrial and Engineering Chemistry, 1931.
11. Bull, Ø., Bratteli, F., Ringen, J.K., Melhuus, K., Bye, A.L., Iversen, J.E.: “The Quest for True Residual Oil Saturation – An Experimental Approach”, SCA201103
12. McPhee, C., Reed, J., Zubizarreta, I. “Core Analysis: A Best Practice Guide”, chapter 10 about relative permeability, Developments in Petroleum Science, Elsevier, 2015, Volume 64, Pages 519-653.
13. Irwin D.D., Baticky J.P. “The successive displacement process: oil recovery during blowdown”, SPE 36719, November 1997, SPERE Journal.
14. Carlson F.M.: “Simulation of relative permeability hysteresis to the non-wetting phase”, SPE 10157, ATCE, San Antonio, Texas, 4-7 October 1981.

Gas-water steady-state relative permeability determination with two approaches; experimental and digital rock analysis, strengths and weaknesses

R. Farokhpoor[1], E. Westphal[1], N. Idowu[1], P.E. Øren[1], B. Fletcher[2]
[1]FEI Oil and Gas, [2]BG Group, Reading, UK

This paper was prepared for presentation at the International Symposium of the Society of Core Analysts held in Snowmass, Colorado, USA, 21-26 August 2016

ABSTRACT

Digital Rock Analysis (DRA) or pore-scale imaging and modelling have developed significantly in the last decade with the emphasis changing from phenomenological research towards quantitative modelling. The evolution towards more predictive modelling raises questions about the reliability of DRA derived properties compared to experimentally measured data, especially for multiphase flow.

In this work, we compare gas-water relative permeability functions obtained from experimental measurements with those derived from DRA. The steady state tests were performed on single plugs with in-situ saturation monitoring. The experiments showed strong non-uniformity in saturation profiles along the plugs and a numerical approach is used to correct for this artefact.

3D X-ray micro-computed tomography (micro-CT) images of the three sandstone plugs and representative sub-plugs were acquired along with Backscattered Scanning Electron Microscopy (BSEM) images of 2D sections. 3D pore networks were extracted from the sub-plug and process-based models (PBM). Gas-water primary drainage and water-gas imbibition relative permeability curves were calculated on the different networks using a pore network model simulator. The DRA derived relative permeability function displays a large degree of similarity with the experimentally measured one. Comparison of fractional flow curves between the experimental (before bump) and DRA computed results shows a difference of 1.0 to 4.0 saturation units for recovery at breakthrough, suggesting that the observed discrepancies in relative permeability have little implications for practical applications.

INTRODUCTION

Accurate determination of relative permeability is essential in estimating producible reserves and ultimate recovery in reservoir models. Laboratory measurements commonly use flow rates higher than those characteristic of flooding processes in the reservoir to overcome discontinuities in capillary pressure at the boundaries of the core plug. Extensive studies have been performed to minimize this artefact during experiments [1,2]. Numerous approaches have been presented for correcting experimental data using numerical methods, semi-analytical approaches and/or inverse modeling [3-5].

Prediction of multiphase flow properties using DRA has evolved significantly in the last decade and it is becoming a predictive tool in the oil industry. It is generally agreed that

for mixed to oil-wet system, DRA cannot reliably predict multiphase flow properties without detailed representation of contact angles, but for strongly water-wet systems (gas-water systems in this work) DRA results should compare favorably with experimental data. Some authors have compared DRA derived imbibition relative permeability with experimental results for clean sandstones and sandpacks [6-11] but further studies are required for more complicated samples.

In this study, we determined imbibition water-gas relative permeability on three sandstone samples with two approaches. Flow simulations were performed on networks which were extracted from a process-based model and on networks which were extracted from the segmented micro-CT images of the sub-plugs. Comparisons of measured steady-state relative permeability data with predicted results on the same samples show good agreement and differences between the values are within an acceptable range.

Laboratory experimental data

Petrophysical properties of the three core plugs with short lithological descriptions are given in Table 1.

Table 1: Petrophysical and lithological properties of the three core plugs

Plug No.	Depth (m)	Porosity (fraction)	Permeability (mD)	Lithological properties
Plug 1	3186.5	0.233	873	Homogeneous, poorly consolidated, weakly sorted medium to coarse grained sand
Plug 2	4460.14	0.173	1.5	Homogeneous, well sorted fine sandstone
Plug 3	2684.84	0.289	2162	Poorly consolidated, coarse grained sand

Imbibition water-gas steady-state relative permeability experiments were performed on the three core plugs in a core analysis laboratory (Figure 1).

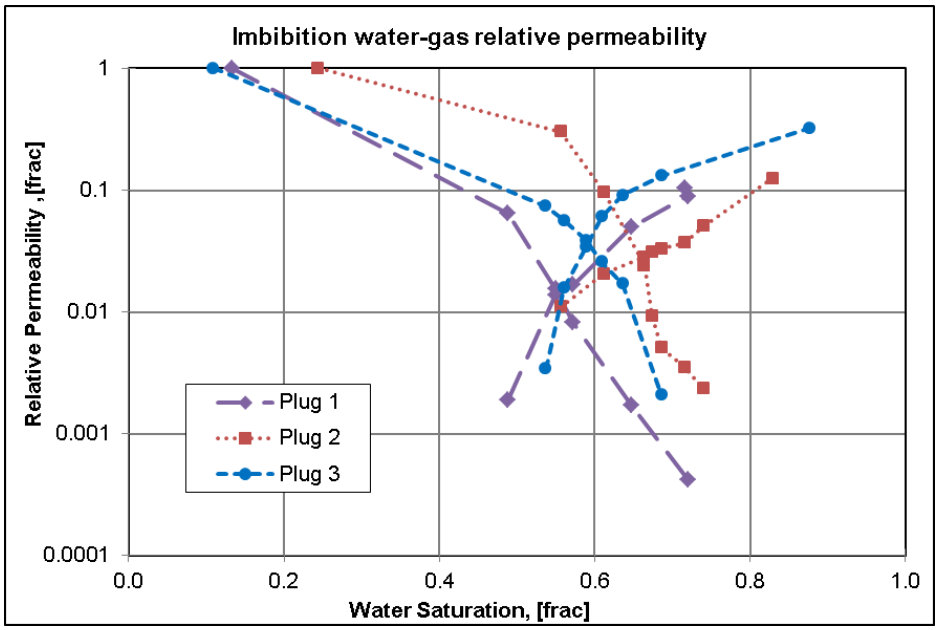

Figure 1: Experimental imbibition water-gas steady-state relative permeability curves

Saturation profiles were mapped during the core plug flooding experiments using an AXRP-300, automated X-Ray relative permeameter. Figure 2 shows that there is a strong non-uniformity in saturation profiles of plugs 1 and 2 while it is less pronounced for plug 3. To correct for this artefact, Sendra simulator was used. The core plug geometry and petrophysical properties were used to build a simple model and to simulate a steady state water-gas imbibition process. The main application is to determine relative permeability from experimental data through an automated history matching of differential pressure (Figure 3-left) and saturation profile. The relative permeability results based on LET [12] correlation are plotted in Figure 3-right.

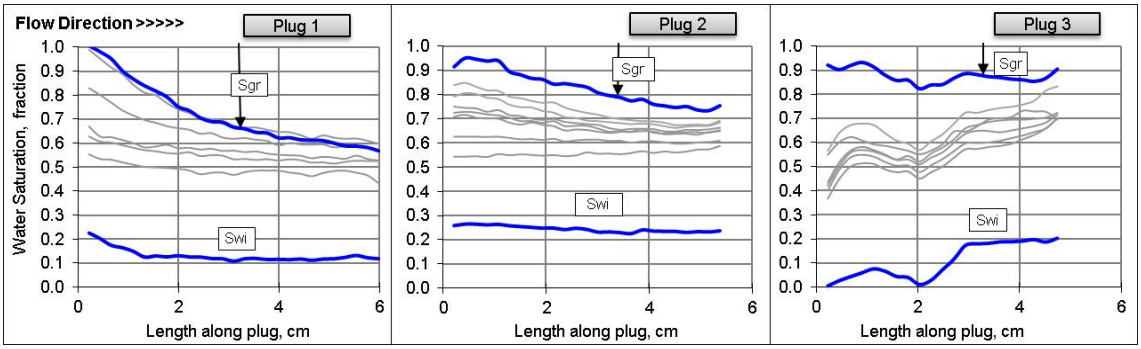

Figure 2: Water saturation profiles along the core plug during flooding experiments

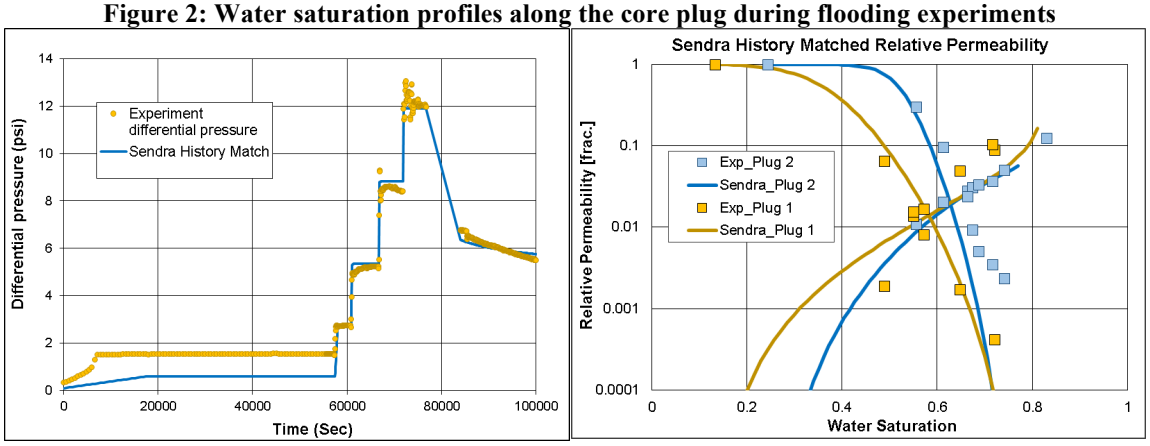

Figure 3: Left) experimental differential pressure and Sendra history matched data for plug 1, Right) comparison of experimental and Sendra relative permeability for plugs 1 and 2

Simulated Sendra results for plug 1 shows that residual gas saturation and water relative permeability are lower compared to the experimental data. In plug 2, the Sendra history matching predicted comparable residual gas saturation and water relative permeability to the experimental data before the bump flood. The main disadvantage of correcting artefact errors using a numerical simulation method is that the results are nonunique and it depends on what correlation has been used.

Digital rock analysis

The workflow used for digital rock analysis can be summarized with the following steps:

1. Overview micro-CT scans of the received core plugs (19µm/voxel)

2. Thin section preparation from a trim end of the core plug and BSEM imaging at multiple scales
3. Image analysis to obtain input data for process-based modelling.
4. PBM construction (capturing relevant rock types).
5. Drilling of a sub-plug (2-5 mm in diameter and 1-2 cm long)
6. Scanning sub-plug by micro-CT at highest possible resolution (1-5 µm/voxel)
7. Processing and generation of rock models from the scanned images
8. Calculation of petrophysical properties (ø, K_{abs}).
9. Extraction of pore network representations from PBM and sub-plug 3D image.
10. Simulation of multiphase flow properties for gas-water system

The workflow is illustrated in Figure 4.

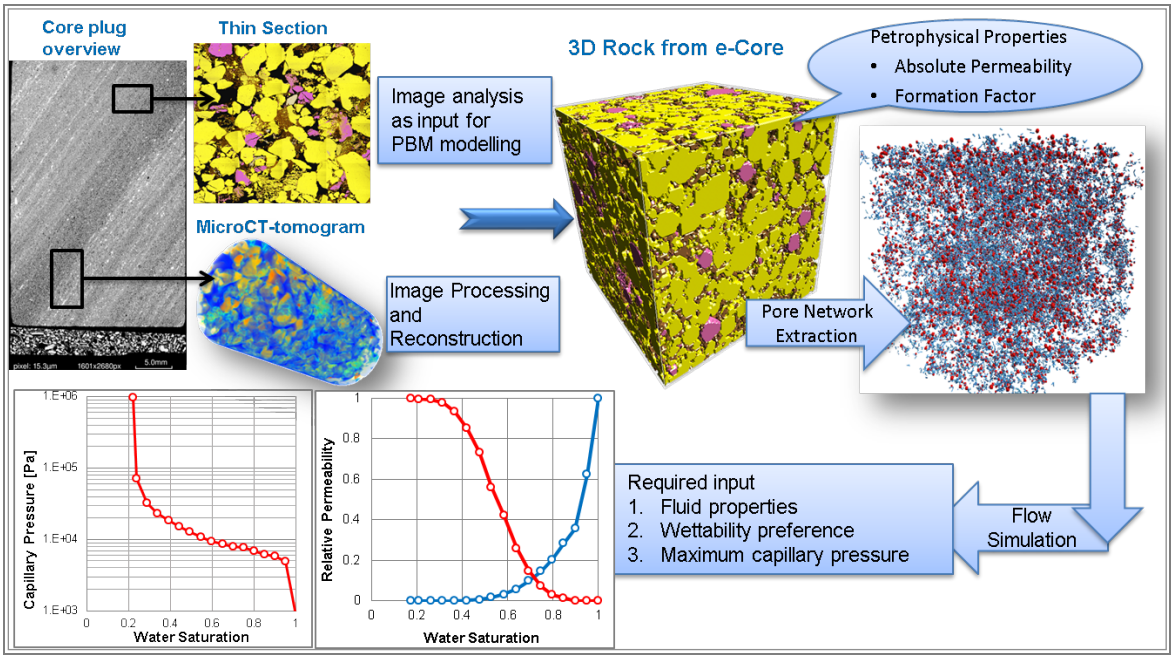

Figure 4: Schematic view of workflow

Imaging

Core plugs of 1.5 inch diameter were scanned on a high resolution micro-CT at 19µm per voxel. The purpose was to:

1. Identify rock types and characterise their distribution and volumes within the core plugs.
2. Select locations for cutting sections through the core plug. Thin sections were prepared and BSEM images were acquired (see Figure 5). These images were used to obtain detailed information on mineralogy, grain size, shape and sorting, pore sizes and any type of clay and cementing minerals.
3. Select location for coring a sub-plug with an attempt to capture a representative elementary volume (REV) from each core plug. Micro-CT scanning of the sub-plugs was carried out on a high-resolution scanner, FEI HeliScan (see Figure 5).

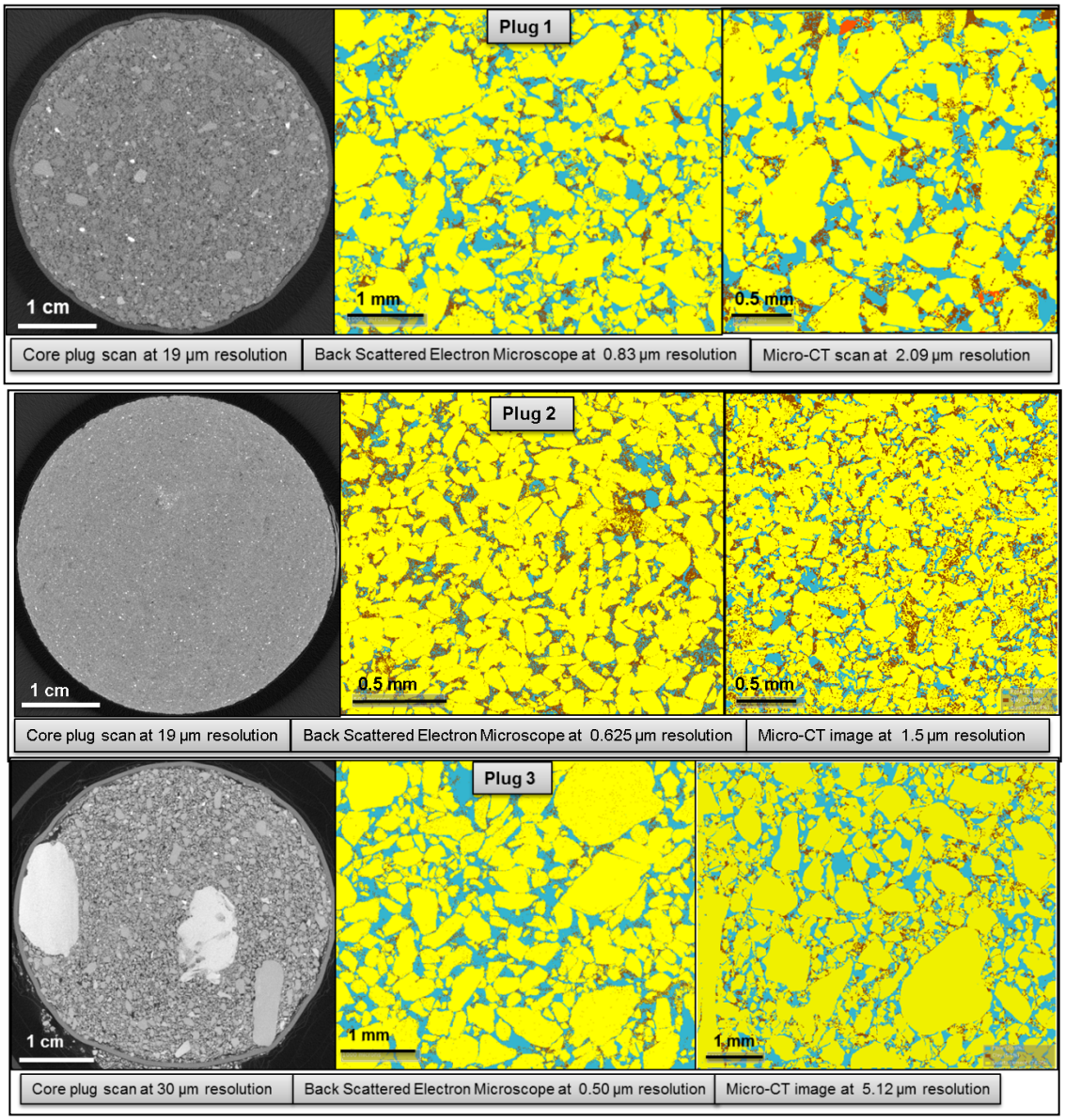

Figure 5: Images of; the core plugs from micro-CT (left), the trim end from BSEM after segmentation (centre), and the sub-plugs from micro-CT. (Yellow color is quartz; orange is feldspar, brown is clay and blue is pore)

Modelling

The BSEM images of the thin section of the core plugs were segmented to produce ternary images of pores; micro-porous phase (clay) and matrix. The ratio of the number of pixels in each threshold bin to the total number of pixels in the image is an estimate for the fraction of the mineral in the rock. For each core plug, one PBM was generated, representing the rock type (RT1) observed in the trim end. For each sample, the proportion of intergranular and micro-porosity, clay content and PBM size and resolution and sub-plug image resolution are given in Table 2.

Table 2: Intergranular and micro-porosity and models size and resolution

Sample	Intergranular porosity (frac)	Micro-porosity (frac)	Clay (%)	PBM size (µm)	PBM resolution (µm)	Sub-plug resolution (µm)
Plug 1	0.206	0.039	6.5	1800	1.0	2.09
Plug 2	0.092	0.080	15.8	720	0.4	1.5
Plug 3	0.248	0.025	6.0	2520	1.4	5.12

Pore-scale resolution 3D models were constructed by PBM, based on the information extracted from the BSEM images. The algorithms applied for the construction of numerical 3D reservoir rock models are based on simulation of the geological processes by which the rock was formed: sedimentation, compaction, and diagenesis [13]. There are several options to place the clay regarding distribution and shape. It can vary from pore lining clay (as often observed in these samples) to more clustered pore-filling clay and to clay from feldspar dissolution. The resulting 3D models are quality checked both visually and statistically against the BSEM images. Figure 6 shows a 3D view of the cubic PBMs for all three plugs.

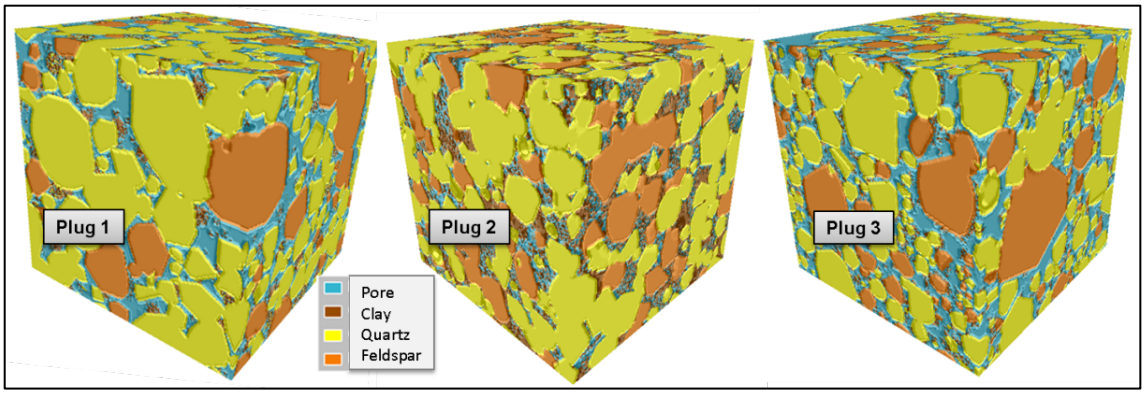

Figure 6: 3D image of process based model for each of the three plugs

The 3D micro-CT scans of the core plug were used to visualize the heterogenity and to select the proper location for one or more subplugs. Micro-CT scan of all three plugs show that one sub-plug is enough to capture the heterogeneity of the plug. To find an REV size for the sub-plug, both pore throat and grain size distribution were considered. BSEM images of the trim ends give useful information about grain size distribution. The minimum diameter for sub-plug is bigger than 15 times the size of the largest grain observed in BSEM. Pore throat size distribution from MICP experiment (if it is available) shows what image resolution is required to be able to capture pore scale phenomenas. For plugs wih smaller pore throat radii, micro-CT scans require higher resolution thus smaller sub-plug is needed (like plug 2).

The micro-CT images of the sub-plugs were segmented according to X-ray attenuation of involved minerals to obtain porosity, micro-porous phase (clay) and matrix. The segmentation was supported by morphological observation. The size of most clay minerals is below the resolution of the images and in most cases it introduces an artefact. Figure 7 shows a 3D view of the micro-CT scans of the sub-plugs and the image dimensions.

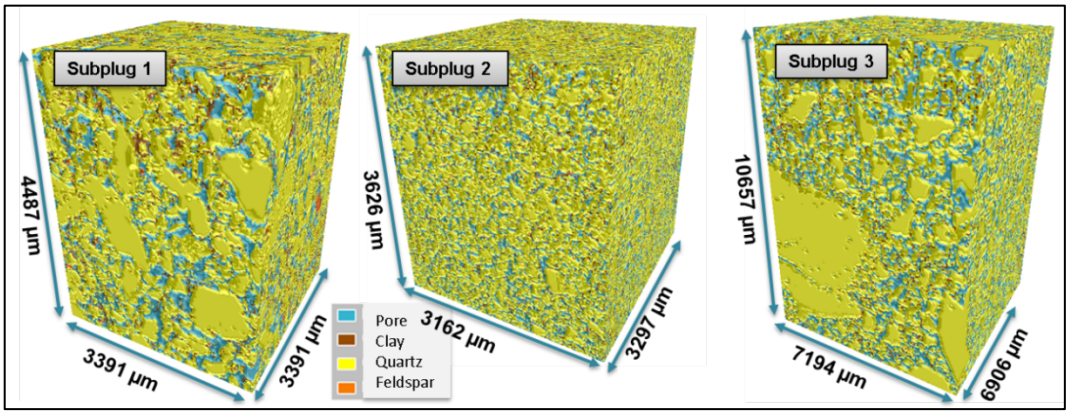

Figure 7: 3D view of sub-plug micro-CT scans

Flow simulation

To perform multiphase flow simulations, the pore space of the reconstructed models is transformed into simplified pore networks, which are used directly as inputs to a network model. Petrophysical properties were calculated for each of the pore scale models, followed by the extraction of their respective pore networks.

The intergranular porosity is given by resolved pores with sizes greater than or equal to the image resolution. The total porosity is the summation of intergranular porosity and sub-resolution porosity (i.e. 0.5-0.6 times the percentage of clay in the rock model). A Lattice-Boltzmann method is applied to solve Stokes' equation in the uniform grid model with maximum 50000 iterations and convergence criteria of 0.005. Flow is driven by a constant pressure gradient through the model. Permeability is calculated with a fluid that does not interact with the rock matrix.

For all samples, calculated porosity is similar to helium porosity and calculated absolute permeability is comparable with Klinkenberg corrected air permeability (see Table 3).

Table 3: Experimental and DRA calculated petrophysical properties

Sample	Helium porosity, (frac)	DRA porosity, (frac)	Klinkenberg permeability, mD	DRA permeability, mD
Plug 1	0.233	0.245	873	1070
Plug 2	0.173	0.172	1.5	0.82
Plug 3	0.289	0.273	2162	1566

The extracted pore networks were used for the simulation of two-phase fluid flow and the calculation of relative permeabilities and capillary pressure curves. The following flow simulations were performed:

- Water-gas primary drainage to initial water saturation (Swi), which is constrained by a maximum capillary pressure of 12.6 bar.
- Water-gas imbibition to residual gas saturation (Sgrw).

The waterflooding process was simulated by assuming the system is strongly water-wet, water index=1.0. The advancing contact angle for water phase was assumed 10-35°.

In all simulations, it is assumed that capillary forces dominate (Nca < 1.0E-6). A detailed account of the methods used for multi-phase flow simulation is given in [14]. Fluid

injection is simulated from one side of the model (usually the x-direction). Thus, the entry pressure is a function of the pore sizes present at the inlet.

Results

Plug 1 is moderately homogeneous and poorly consolidated. Simulated capillary pressure for plug 1 based on the sub-plug and PBM is compared with experimental MICP for a quality control check in Figure 8-left. Capillary pressure corresponding to 2.09 µm resolution in sub-plug is 51675 (Pa) at Sw=0.25. For Sw greater than 0.25, capillary pressure based on the sub-plug is in excellent agreement with the MICP and very good for the PBM (see Figure 8-left). For Sw less than 0.25, there is an insufficient resolution to resolve pores invaded by mercury.

Water-gas imbibition relative permeability simulation results for the PBM and sub-plug are compared with steady state experiments in Figure 9. Simulated water relative permeability for the sub-plug is similar to the steady state experiment but there is a big discrepency in the gas relative permeability.

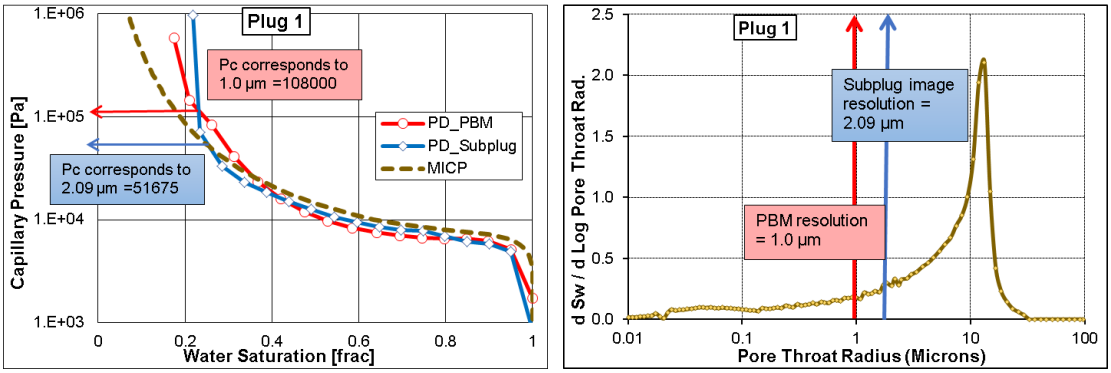

Figure 8: left) Comparison of experimental MICP data with simulated capillary pressure for the PBM and sub-plug, right) pore size distribution from MICP experiment

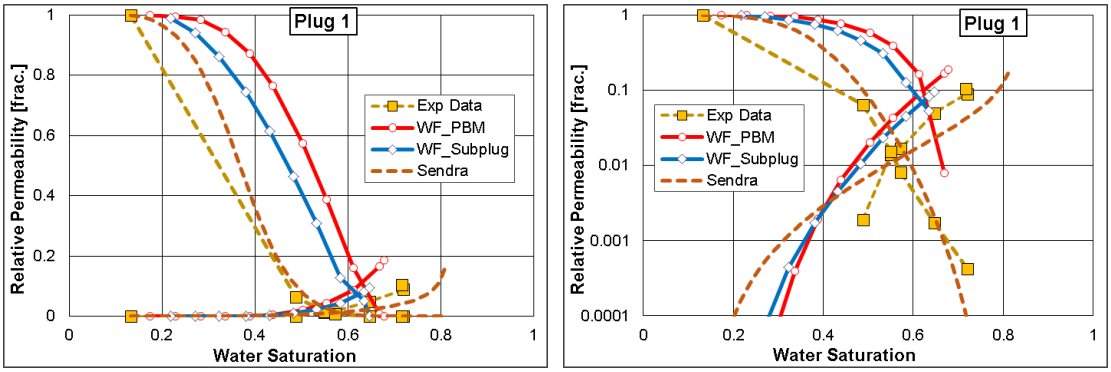

Figure 9: Imbibition water-gas relative permeability curves for the PBM, sub-plug, experimental and Sendra simulation for plug 1

Table 4: Two phase flow results for plug 1

Parameter	Experiment after bump	Experiment before bump	Sendra	PBM	Sub-plug
Swi	0.13	0.13	0.13	0.17	0.21
Sgrw	0.28	0.28	0.19	0.32	0.35
Krw at Sgr	0.105	0.090	0.165	0.187	0.095

Unlike plugs 1 and 3, plug 2 is tight with well sorted, fine grains and is clay rich. The porosity of the plug is 0.17 and almost half of it is micro-porosity (0.08). Experimental MICP pore throat size distribution shows the pore throats are smaller than 1 µm. segmentation of the micro-CT image of the sub-plug (1.5 µm resolution), resulted in a high degree of uncertainity for distinguishing between pores and micro-porous clay patches. As shown in Figure 10, the simulated capillary pressure for the sub-plug is much lower than the experimental MICP while capillary pressure based on the PBM is in excellent agreement with the MICP.

The initial water saturation in the sub-plug simulation is very high, Swi=0.48, and so there is no basis to compare simulated gas-water relative permeability from the sub-plug with the experiment. However, simulated gas and water relative permeability curves and residual gas saturation in the PBM are comparable with the steady state experiment before the bump (see Figure 11).

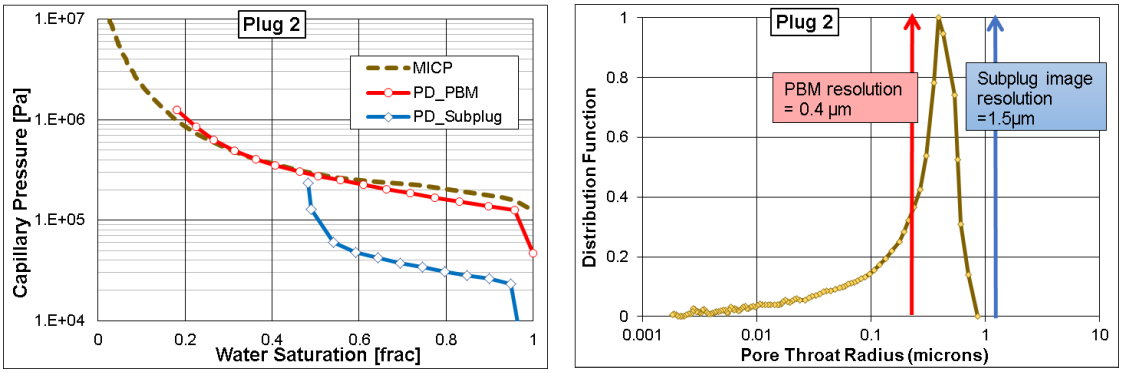

Figure 10: left) Comparison of experimental MICP data with simulated capillary pressure for the PBM and sub-plug, right) pore size distribution from MICP experiment

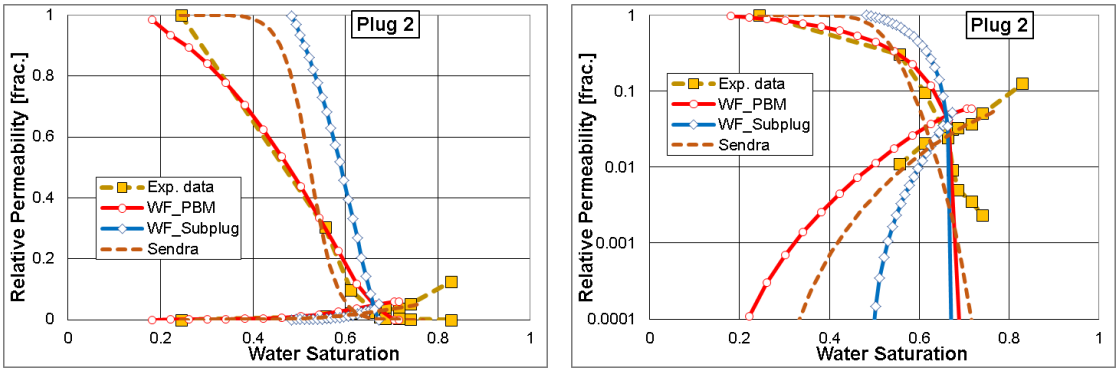

Figure 11: Imbibition water-gas relative permeability curves for the PBM, sub-plug, experimental and Sendra simulation for plug 2

Table 5: Two phase flow results for plug 2

Parameter	Experiment after bump	Experiment before bump	Sendra	PBM	Sub-plug
Swi	0.24	0.24	0.24	0.18	0.48
Sgrw	0.17	0.26	0.23	0.28	0.33
Krw at Sgr	0.125	0.051	0.056	0.059	0.052

Plug 3 is an unconsolidated sandstone and the most porous and permeable sample. Due to the coarseness of the grains, it is difficult to find a REV for a sub-plug. To capture different features, a bigger sub-plug was required compared to the other two samples (see Figure 7). For the bigger sub-plug, the resolution of the micro-CT image is lower, 5.12 µm, thus it is not possible to capture the pores smaller than 5.12 µm. As shown in Figure 12, simulated capillary pressure based on the sub-plug is lower than experimental MICP, especially at lower water saturation. By contrast the PBM simulated capillary pressure is very similar to MICP. Simulated gas and water relative permeability and residual gas saturation based on the PBM is comparable with the steady state experiment before flooding the core plug with high flow rate (see Figure 13).

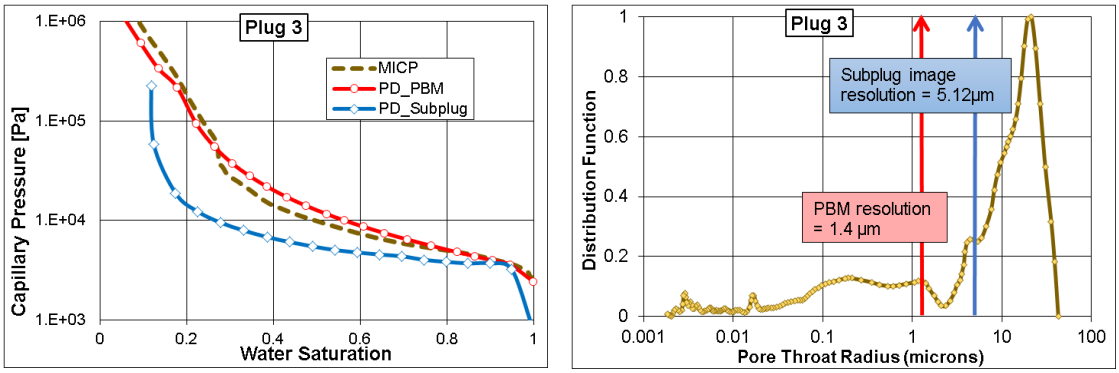

Figure 12: left) Comparison of experimental MICP data with simulated capillary pressure for the PBM and sub-plug, right) pore size distribution from MICP experiment for plug 3

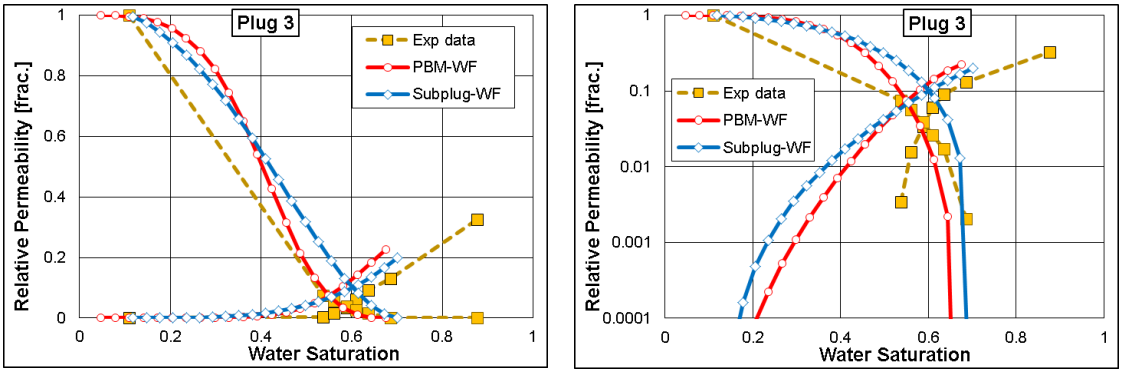

Figure 13: Imbibition water-gas relative permeability curves for the PBM, sub-plug and experiment

Table 6: Two-phase flow results for plug 3

Parameter	Experiment after bump	Experiment before bump	PBM	Sub-plug
Swi	0.11	0.11	0.05	0.12
Sgrw	0.12	0.31	0.32	0.30
Krw at Sgr	0.325	0.131	0.226	0.198

Discussion of Results

For plug 1, the DRA relative permeability on both the sub-plug and PBM show a large degree of similarity with the experimental relative permeability. For plugs 2 and 3, the DRA relative permeability based on the PBM is in good agreement with that from the steady state experiment.

Comparisons of fractional flow curves of experimental and simulated PBM results presented in Figure 14 show differences that range from 1 to 4 saturation unit for recovery at breakthrough (before bump in the experiment). This range is acceptable considering the fact that the initial water saturations are different in the simulations and experiments. With respect to the gas relative permeability, however, there is a big discrepancy in the measured and simulated data. This discrepancy may be due to the fact that there is a suppression of gas connectivity/conductivity due to non-uniform saturation profiles (lower gas saturation at the inlet) shown in Figure 2.

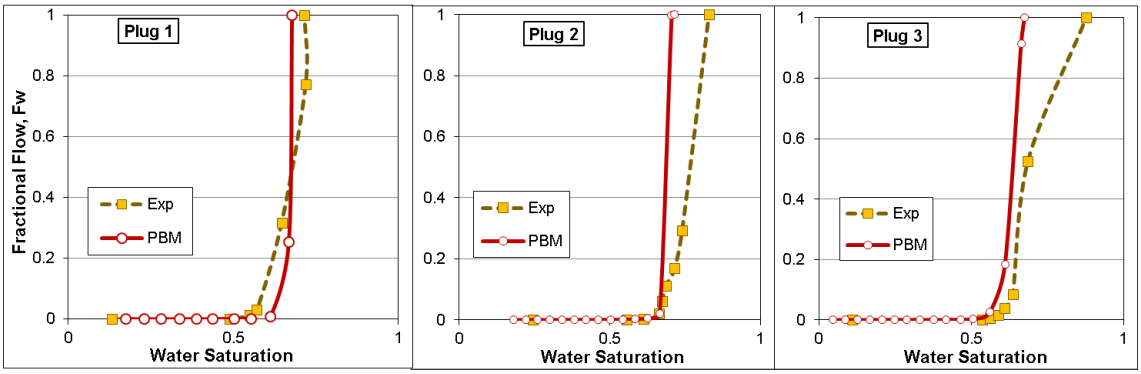

Figure 14: Fractional flow curves for experiment and PBM simulation for all plugs

CONCLUSION

Three sandstone samples were tested to compare gas-water relative permeability data from two different approaches: steady state experiment and DRA. The DRA simulations were performed on the micro-CT image of the sub-plug and on a process-based model. Comparison of fractional flow curves from experiment and DRA shows a good agreement in recovery after breakthrough. The discrepancy in water relative permeability is within an acceptable range and with one exception, the same trend was observed for gas relative permeability.

Non-uniform water saturation along the core plug displays artefacts (disequilibria effects or capillary-end effects) in the coreflood experiments, which can significantly influence the computation of end-point relative permeabilities and saturation. Numerical approaches (like Sendra in this work) can be useful to correct for this artefact, but it doesn't account for the core heterogeneity and also it doesn't give a unique result.

In conclusion, there are complications and uncertainties in both experimental and simulation approaches, but the observed discrepancies have little implications for practical applications.

Significant improvements have been made in sample handling and thin section preparation, the micro-CT imaging technology and image processing tools since this work was completed in 2015.

ACKNOWLEDGEMENTS

We would like to acknowledge BG UK for providing experimental data and allowing the publishing of the results.

REFERENCES

[1] A. L. Chen and A. C. Wood, "Rate effects on water-oil relative permeability," Society of Core Analysts, 2001, SCA2001-19.

[2] R. Gupta and D. Maloney, "Application of the intercept method to correct steady-state relative permeability for capillary-end-effect," Society of Core Analysts, 2015, SCA2015-01.

[3] S. Qadeer, K. Dehghani, D. O. Ogbe and R. D. Ostermann, "Correcting oil/water relative permeability data for capillary end effect in displacement experiments," Society of Petroleum Engineers, 1988, 7423-MS.

[4] F. Hussain, Y. Cinar and P. Bedrikovetsky, "A semi-analytical model for two phase immiscible flow in porous media honoring capillary pressure," Transport in Porous Media, 2012, vol. 92, no. 1, pp. 187-212.

[5] M. H. Krause, J. C. Perrin and S. M. Benson, "Modeling permeability distributions in a sandstone core for history matching coreflood experiments.," Society of Petroleum Engineers, 2009, SPE 126340.

[6] M. Piri and M. Blunt, "Three-dimensional mixed-wet random pore-scale network modeling of two- and three-phase flow in porous media. II. Results," PHYSICAL REVIEW E 71, 2005, vol. 026302, pp. 1-11.

[7] M. Blunta, B. Bijeljica, H. Dongb, O. Gharbia, S. Iglauerc, P. Mostaghimia, A. Palusznya and C. Pentlanda, "Pore-scale imaging and modelling," Advances in Water Resources, 2013, vol. 51, p. 197–216.

[8] B. Raeesi, N. Morrow and G. Mason, "Pore network modelling of experimental pressure hysteresis relationships," Society of Core Analysts, 2013, SCA2013-15.

[9] A. Aghaei and M. Piri, "Direct pore-to-core up-scaling of displacement processes: Dynamic pore network modeling and experimentation," Journal of Hydrology, 2015, vol. 522, p. 488–509.

[10] C. H. Pentland, Y. Y. Tanino, S. Iglauer and M. Blunt, "Capillary trapping in water-wet sandstones: coreflooding experiments and pore-network modeling," Society of Petroleum Engineers , 2010, SPE 133798.

[11] P. Valvatne and M. Blun, "Predictive pore-scale modeling of two-phase flow in mixed wet media," Water Resources Research, 2004, vol. 40, pp. W07406-1-21.

[12] F. Lomeland, E. Ebeltoft and T. Hammervold , "A new versatile relative permeability correlation," Society of Core Analysts, 2005, SCA2005-32.

[13] P.-E. Øren and S. Bakke, "Process based reconstruction of sandstones and prediction of transport properties," Transport in Porous Media, 2002, pp. 311-343.

[14] P.-E. Øren, S. Bakke and O. J. Arntzen, "Extending predictive capabilities to network," SPE Journal, 1998, pp. Vol 3, Issue 4.

COLLABORATION BETWEEN DIGITAL ROCK ANALYSIS AND LABORATORY FOR GENERATION OF MULTIPHASE TRANSPORT PROPERTIES FOR RESERVOIR SAMPLES

Nasiru Idowu[1], Alessio Arena[1], Ben Young[1], Arjen Mascini[1], Kurdistan Chawshin[1], Carley Goodwin[1], Silvano Sommacal[1], Stig Bakke[1], Mark Knackstedt[1], Pål-Eric Øren[1], and Mohammad Piri[2]
[1] FEI Oil and Gas; and [2] University of Wyoming

This paper was prepared for presentation at the International Symposium of the Society of Core Analysts held in Snowmass, Colorado, USA, 21-26 August 2016.

ABSTRACT
We present a collaborative study between FEI digital rock analysis (DRA) services and University of Wyoming on poorly sorted clastic reservoir core materials. The methodology highlights a multiscale approach which features plug/sub-plug scale imaging, and submicron resolution using Backscattered Scanning Electron Microscopy (BSEM) imaging. Pore network models were generated from micron-scale sub-plug images for the resolved porosity and with a process-based reconstruction method (PBM) for the sub-resolution porosity. The pore-scale advancing contact angles were measured *in situ* and used as inputs in the simulator. The simulation results obtained from the different pore networks were upscaled using a steady-state technique for each sample. This approach enables us to generate reliable multiphase transport properties on three bi-modal sandstone reservoir samples. Simulated results are compared with available experimental data.

INTRODUCTION
In the current seemingly unending oil price slump, the oil and gas industry must be innovative and ensure optimal recovery of hydrocarbons from conventional and unconventional reservoirs at minimal costs. This requires a good understanding of the reservoir wettability, reliable static/multiphase transport properties and detailed reservoir characterizations, simulations and management. For gas/water systems [1] and oil/water water-wet cases [2, 3], DRA offers a timely alternative approach to obtain essential multiphase transport data from 3D images of rock samples and/or from simplified pore networks extracted from high resolution images. It also provides the opportunity for fast and meaningful sensitivity studies on discrete and homogeneous core material.

However, most reservoirs are neither water-wet nor oil-wet and determination of the actual wettability distribution is crucial [4]. Amott [5] or USBM [6] tests can provide

quantitative averaged wettability information of a core sample. Contact angle, however, is the most universal measure of the wettability of surfaces [4]. Andrew *et al*. [7] recently presented a method for contact angle measurement from X-ray micro-computed tomography (MCT) of a supercritical CO_2-brine system in a Ketton limestone with simple mineralogy (comprising 99.1% calcite and 0.9% quartz). Qualitative pore-scale distribution of wettability has also been obtained by integrating information from MCT, Field Emission Scanning Electron Microscopy (FESEM), and Quantitative Evaluation of Minerals by SEM (QEMSCAN) [8]. With detailed information on the pore-scale distribution of wettability [8] or the pore-scale distribution of contact angles [7, 9], reliable multiphase flow properties can be generated through DRA for non-water-wet cases.

In this paper, we present a collaborative study between FEI DRA services and University of Wyoming state-of-the-art laboratory to generate single- and multiphase transport properties for three bi-modal sandstone reservoir samples. The pore-scale advancing contact angles were measured *in situ* and ranged from 90^o to 128^o using similar procedure to those stated in [9]. These were used as inputs in a quasi-static pore network simulator [3] and by so doing, we reduced uncertainties associated with wettability characterization at the pore-scale and thereby improved the reliability of the predicted data. We explored one of the strengths of DRA further and generated sensitivity analysis of the predicted data to different scenarios that would otherwise, have taken years to accomplish in the laboratory. Finally, we compared simulated results with available experimental data.

IMAGE ACQUSITION AND ANALYSIS

In the original program, twelve conventional plugs were extracted from unpreserved core material of a clastic reservoir and were characterized texturally and mineralogically. They were imaged by MCT using a HeliScan micro-CT system. Three of these plugs were chosen for the study of multiphase flow properties based on their importance to the reservoir, their specific rock typing and the quality of the reservoir material. An analysis workflow incorporating conventional and imaging laboratory techniques with DRA techniques was designed to obtaining the desired results in a timely manner, while optimizing the costs. A schematic diagram of this workflow is shown in Figure 1.

The three chosen plugs - most relevant to the reservoir-planning scenario - exhibit different depositional facies, degrees of heterogeneity, different sorting and grain size. Differences are also noted when comparing measured RCA data: porosities and permeabilities range from 21% and 768mD for *Plug* 3 to 28% and 16.8mD for *Plug* 1. Petrographically, *Plug 1* is a poorly sorted sandstone/siltstone (fine silt to very fine sand) with abundant microporous pore filling material – Figure 2. The microporous phase is dominated by micro crystalline quartz and illite. The Backscattered Electron (BSE) images indicate that a significant part of the porosity is associated with the microporous phase.

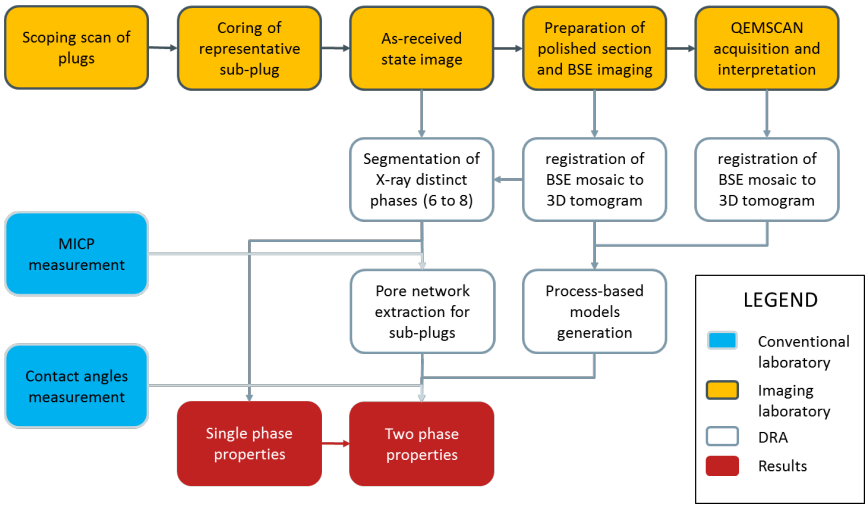

Figure 1. Analysis workflow used for this study

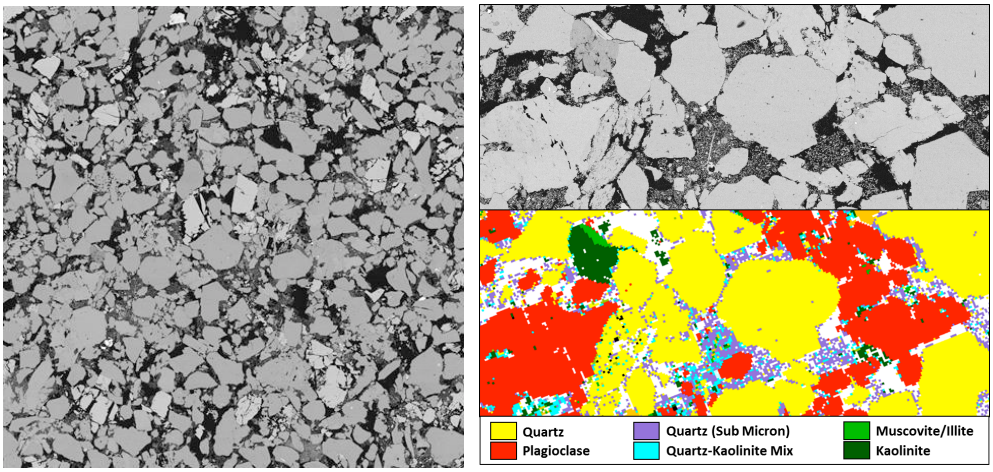

Figure 2. BSE image of plug 1, side length is 1 mm. Right: detail of BSE image and QEMSCAN map showing the mineralogical nature of the pore filling material and framework grains

Plug 2 is a poorly sorted sandstone/siltstone (medium silt to medium sand) with medium to poorly rounded grains with some pore filling microporous phase – Figure 3. The microporous phase consists of kaolinite booklets, micro crystalline quartz, illite and some carbonate/pyrite.

Plug 3 is a sandstone with a distinct unimodal grain size distribution – Figure 4 and Figure 7. Medium to coarse well rounded sand grains are surrounded by coarse silt to fine sand infill. Small amounts of microporous phase are dominated by kaolinite booklets.

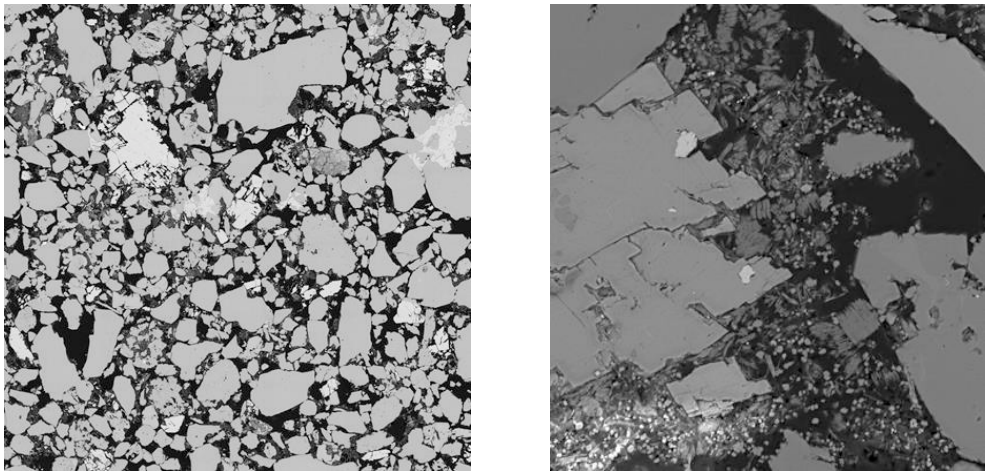

Figure 3. Left: BSE image of plug 2, side length is 2.5 mm. Right: Pore filling material

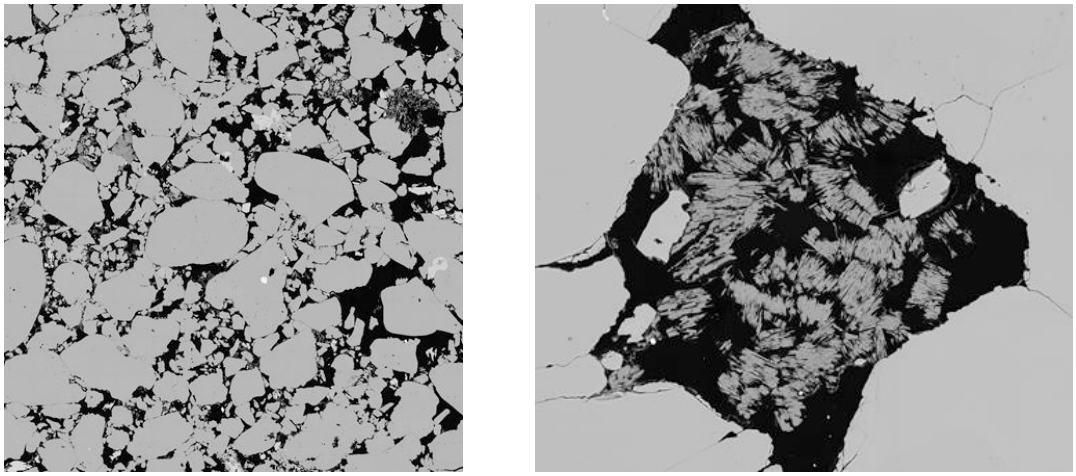

Figure 4. Left: BSE image of plug 3, side length is 5mm. Right: Pore filling kaolinite booklets

The textural differences of those samples led us to use specific coring diameter when extracting representative sub-plugs. This decision was taken in the attempt to capture a representative elementary volume (REV) estimated as 15 times the largest observed grain while maximizing the imaging resolution. Table 1 summarizes the coring diameter, length and image voxel size for each plug. Acquired images were segmented into X-ray distinct phases (up to 8 identified phases) using codes based on the converging active contour algorithm [10]. The dimensions of those images are approximately 1500 voxels in the *x* and *y* direction, and 3000 to 6000 voxels in the *z* direction; the file size is approximate 16 to 32 GB of data per image. One vertical slice for each of the three samples is shown in Figure 5. Table 2 describes the partitioning of the 3D image into porosity, microporous pore filling material, mineral grains and high density inclusions. For each of the samples, we extracted an additional 8mm sub-plug used to generate laboratory MICP data.

Table 1: Sub-plugs extraction/coring diameter, length and image voxel size for each sample

Sample	Coring diameter (mm)	Length (mm)	Voxel size (µm)
Plug 1	3	9	2.2
Plug 2	4	8	2.9
Plug 3	8	16	5.5

Sub-plugs were subsequently embedded in resin and then cut to prepare a polished section. This was imaged and analyzed by electron microscopy techniques such as BSE and Secondary Electron (SE) high magnification imaging. The mosaics of images and mineralogical maps produced in this way were registered back to the tomogram using a proprietary algorithm [11]. This enables one to directly quality check (QC) the image quality and segmentation undertaken on the 3D tomogram to higher resolution BSE data. In Figure 6, a segmented dataset (3 micron voxel sizes) is registered to a BSE image (500 nm pixel size). The segmentation into 8 phases undertaken in the 3D tomogram correlates well to solid, microporous and open porosity regions observed in the BSE images.

Table 2. Results from the segmentation of X-ray distinct phases performed on sub-plug µCT images

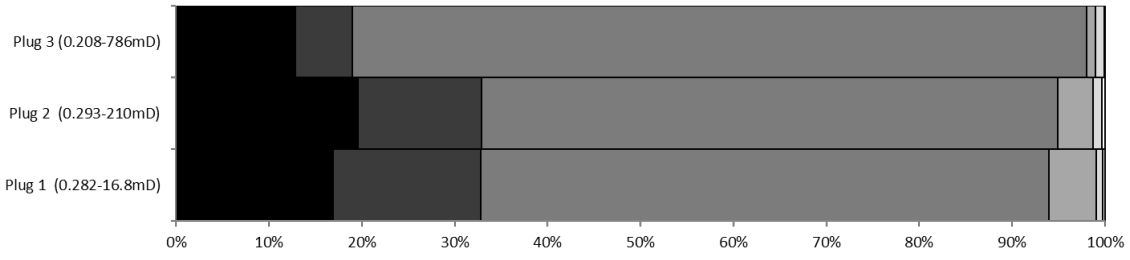

	Plug 1 (0.282-16.8mD)	Plug 2 (0.293-210mD)	Plug 3 (0.208-786mD)
Pores	16.9	19.6	12.8
Pore-filling material	15.8	13.3	6.2
Quartz	61.1	61.9	78.9
Feldspar	5.1	3.8	1
Calcite	0.7	1	0.9
High density minerals	0.2	0.3	0.1

RESULTS

Single-Phase Properties and MICP

We compute absolute permeability via imaged-based single-phase lattice Boltzmann permeability simulation. This technique only considers flow along the resolved pore pathway - through the macropores in the image; the percolation condition was met for all three sub-plugs based on the careful choice of resolution to target for our X-ray tomograms. Estimated porosities and calculated absolute permeabilities were then compared to the experimental laboratory measurement to check the relevance of the sub-region chosen compared to the original plug scale. Comparison of the experimentally derived data and image based results are shown in Table 3.

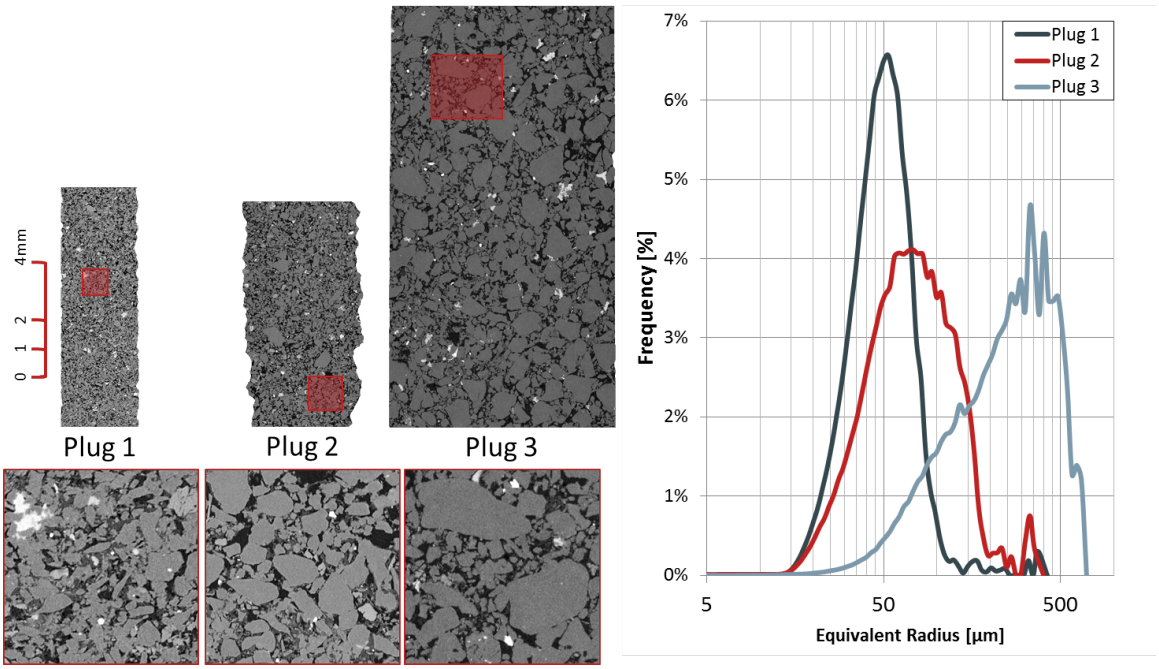

Figure 5. Vertical slices extracted from the sub-plug tomograms, plus zoom in of the highlighted region in red. The scale represented is valid only for the vertical slice. On the right: grain size distribution of the three samples calculated from X-ray tomograms as radius of the equivalent sphere

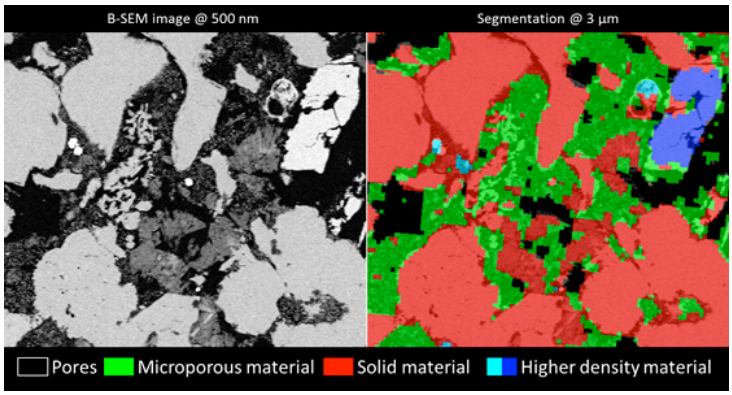

Figure 6. Visual comparison between a BSE image of the polished section prepared within the field of view of the tomogram and the corresponding horizontal slice from the segmentation result

Table 3. Comparison between laboratory measurement and digital results for porosity and absolute permeability for all three samples

Sample	Porosity (fraction)			Absolute permeability (mD)	
	RCA - plug	MICP – sister sub plug	µCT - sub-plug	RCA - Plug	µCT - sub-plug
Plug 1	0.282	0.278	0.246	16.8	62
Plug 2	0.293	0.267	0.287	210	225
Plug 3	0.208	0.18	0.175	786	660

Differences in the RCA plug and μCT sub-plug porosity varies from 0.06 to 3.6 porosity units. *Plug* 1 has the highest difference in porosity and a factor of approximately 3.7 between the measured (on plug) and computed permeability (on sub-plug). These differences may be due to highly heterogeneous nature of *Plug* 1. Measured and computed values for plugs 2 and 3 agree reasonably well. While a QC for prediction of permeability requires one to resolve only the largest hydraulic path, other properties like resistivity, formation factor and two phase properties require one to resolve most of the accessible pore systems. In Figure 7 we report MICP measurements performed on sister plugs to the samples used in the imaging process. The grey vertical lines represent the approximate resolution of the 3D tomograms. This illustrates the porosity that is identified/resolved in the tomogram and is transformed into simplified pore networks [12], which are used directly as inputs to a quasi-static flow simulator [3] for each plug.

Figure 7 also illustrates the significant contribution of the microporous regions to the total porosity. The results mirror the image data acquired in the previous section-- one cannot directly resolve a significant proportion of the porosity in the plugs 1 and 2 from tomography alone and one must incorporate information about the microporous regions in any forward modelling program. For these sub-resolution regions, tomography and segmentation information enables one to identify the spatial distribution of the microporous phase in 3D. The nature of this microporous material is then determined using the high resolution BSE information in (Figure 2 - Figure 4) to develop process and statistically-based methods to mimic the 3D structure of the microporous zones in the image. The PBM algorithms are based on simulation of the geological processes by which the rock was formed; sedimentation, compaction, and diagenesis [13]. Pore networks are also generated for these sub-resolution pores.

Primary Drainage and Waterflooding Simulation Results

Before simulating oil/brine displacement processes and generating the desired transport properties, we first establish for each rock sample whether the extracted pore networks from MCT images and PBM are representative or not. This is achieved by simulating oil/brine primary drainage on the pore networks and then upscaling [14] the resulting network-predicted oil/brine $P_c - S_w$ curves from the different networks for each sample. The upscaled oil/brine $P_c - S_w$ curve for each sample is then compared with measured mercury capillary pressure data on sister samples as shown in Figure 8 for *Plug* 2. The experimental capillary pressure data are scaled to oil/brine $P_c - S_w$ curves using interfacial tensions and contact angles in Table 4. The match between the simulated and measured data is good and confirms that the different pore classes are well captured and the networks are representative.

The oil/brine primary drainage capillary pressure simulation results shown in Figure 8 were stopped at 10 bar to match the entire MICP curves. However, based on the estimated capillary pressure values using oil and brine density and height above the oil-water-contact, the primary drainage simulations were re-run and stopped at a maximum capillary pressure of 2 bar and then followed by waterflooding. The average pore-scale advancing contact

angle of 109° measured *in situ* at University of Wyoming, USA was used as input [5]. For this case, we assume 80% of all pores/throats invaded by oil during primary drainage changed wettability from initial water-wet state to oil-wet condition and investigate sensitivity analysis of the results to different percentages. Oil-wet advancing contact angles for the oil-wet pores/throats are distributed between 100° to 118°. For the remaining water-wet pores/throats, the advancing angles are distributed between 30° to 70°. Figure 8 depicts the primary drainage (PD) and waterflooding (WF) capillary pressure curves and relative permeability results for *Plug* 2. The end-point saturations and relative permeability values for all the three samples are summarized in Table 5.

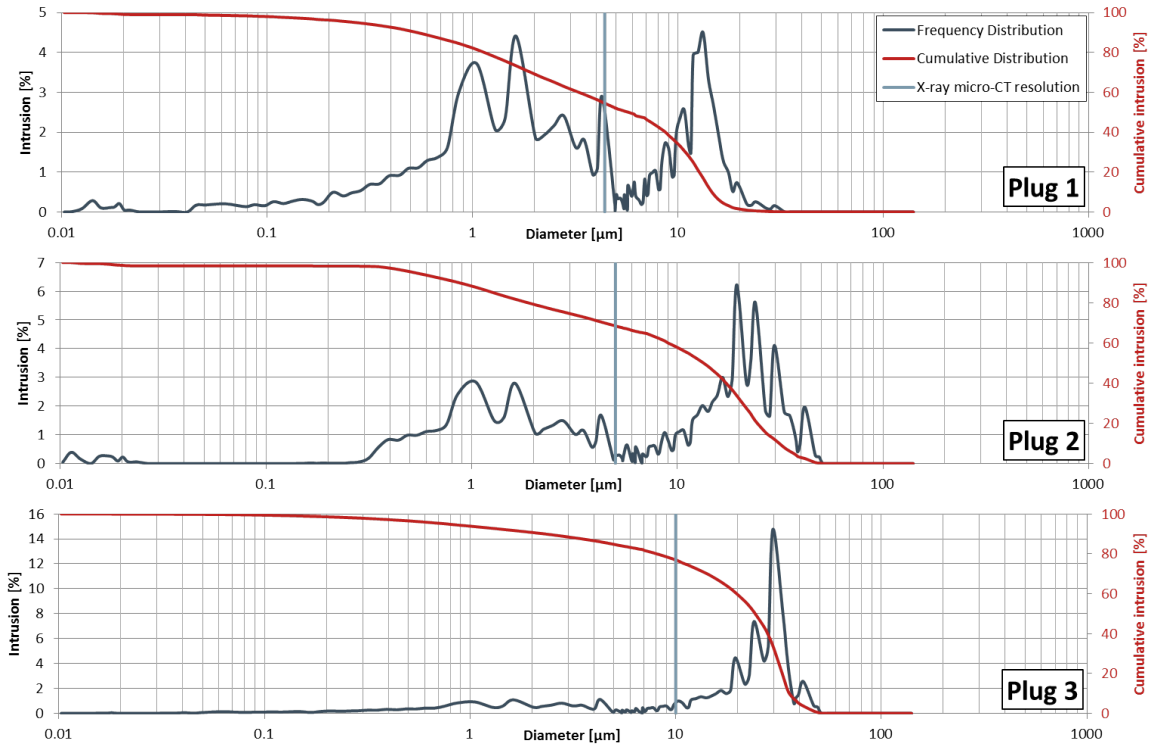

Figure 7 MICP measurement for sister plugs of the three samples studied. The black curve represents the pore size distribution, the red is the cumulative one. The vertical line is the approximate resolution of our tomograms.

Table 4: Input data to flow simulations

Water density	[kg/m^3]	**1000**
Oil density	[kg/m^3]	**700**
IFT$_{oil/brine}$	[dynes/cm]	**30**
IFT$_{Hg/air}$	[dynes/cm]	**480**
Water-wet receding angles	[degr.]	**0° – 10°**
Water-wet advancing angles	[degr.]	**30° – 70°**
Oil-wet advancing angles	[degr.]	**100° – 118°**
Mercury/air contact angles	[degr.]	**140°**
Percentage of oil-wet pores/throats		**80**

Table 5: Measured and simulated end-point saturations and relative permeability values

Property	Measured	Simulated		
		Sample 1	Sample 2	Sample 3
Porosity (fraction)	0.27	0.24	0.25	0.19
Permeability (mD)	130 – 160	93	286	814
Swi (fraction)	0.16	0.18	0.15	0.04
Kro@Swi	0.74	0.98	0.99	0.99
Sorw	0.26	0.32	0.28	0.20
Krw@Sorw	0.28	0.25	0.45	0.40

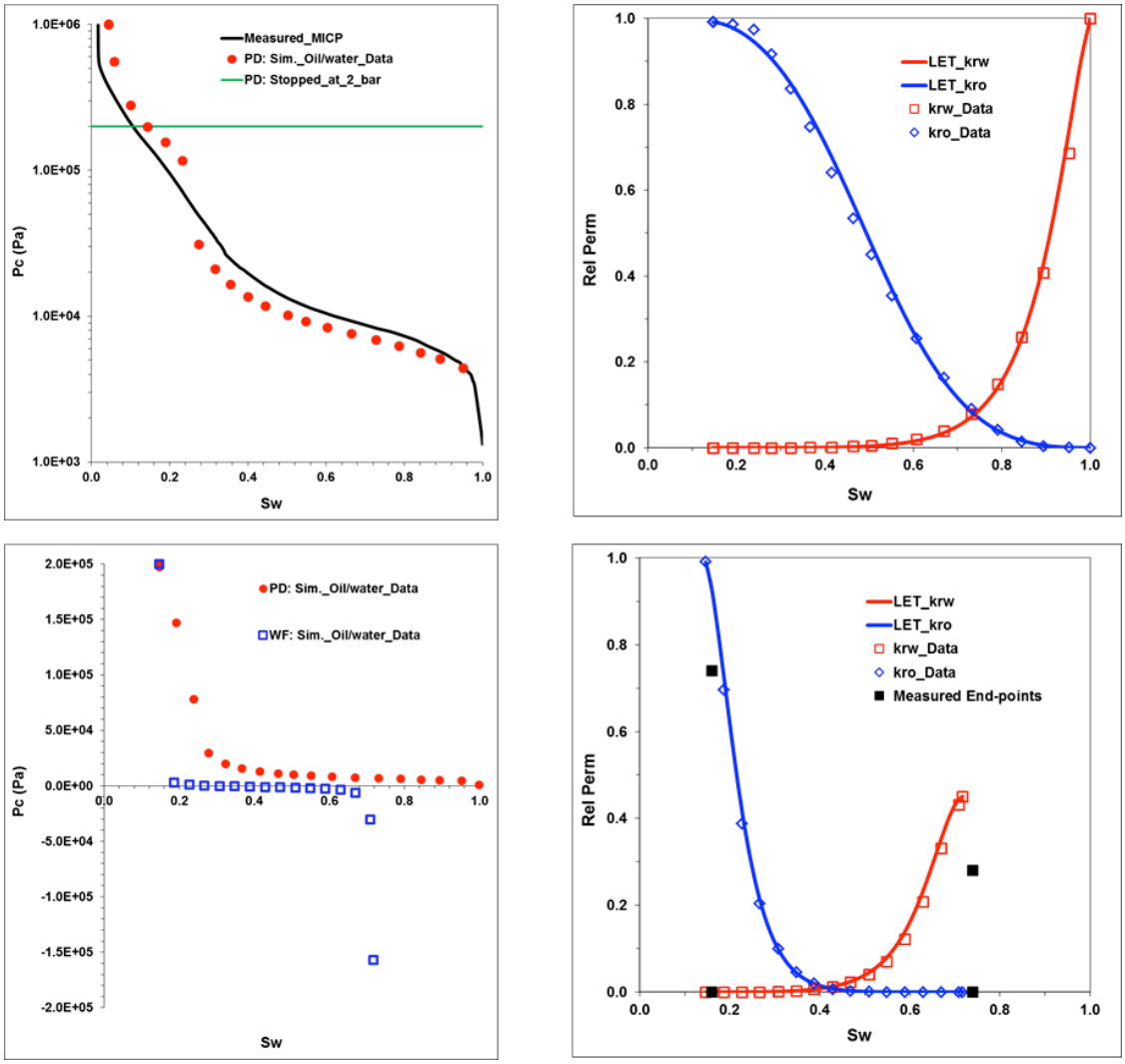

Figure 8: **capillary pressure and relative permeability curves for primary drainage (top) and waterflooding (bottom) for Sample 2.**

Comparison of Simulated Results to Measured Data and Sensitivity Analysis
Capillary pressure and relative permeability data were not measured during the experiments at University of Wyoming. However, porosity, permeability, end-point saturations and end-point relative permeability to water at residual oil saturation were measured on a preserved sample adjacent to sample 2 plug using unsteady-state method. Figure 8 shows the measured end-point values while Table 4 compares the simulated results with measured data. There are good agreements between measured and simulated initial water saturation and residual oil saturation despite the differences in porosity and permeability values. However, lower measured end-point relative permeability values may be due to uncertainties in measured absolute permeability values (130 -160 mD).

DRA enables one to investigate the sensitivity of the simulated results to the percentage of all pores/throats that changed wettability from initial water-wet state to oil-wet condition. We investigated this by running simulations for completely water-wet and oil-wet cases. The percentage of all pores/throats that changed wettability from initial water-wet state to oil-wet condition is 0% and 100% for water-wet and oil-wet case respectively. Oil-wet advancing contact angles for the oil-wet pores/throats are distributed between 140^o to 170^o for the completely oil-wet case while the advancing angles for the completely water-wet case remained the same (30^o to 70^o). The results of the sensitivity analysis compared with the waterflooding results presented in the previous subsection (base case) are shown in Figure 9.

Discussion of Results
The field scale implications of the relative permeability curves depicted in Figure 9 in terms of recovery is investigated using one-dimensional Buckley-Leverett analysis [15]. Assuming oil/brine viscosity ratio of 2, Figure 10 shows recovery as a function of pore volume of water injected. This figure highlights the importance of using appropriate multiphase transport data generated with correct pore-scale distribution of wettability. This will ensure good planning and forecasting and optimal recovery of hydrocarbons at minimal costs.

CONCLUSIONS
Uncertainties associated with wettability characterization at the pore-scale during DRA can be eliminated by the use of *in situ* contact angle measurements. Integration of detailed information on the pore-scale distribution of contact angles with topologically equivalent networks can guide network modelling of multiphase transport properties and considerably improve reliability of predicted results. For non-water-wet systems, we advocate an analysis workflow that incorporates conventional and imaging laboratory techniques with DRA techniques for generation of desired multiphase transport properties.

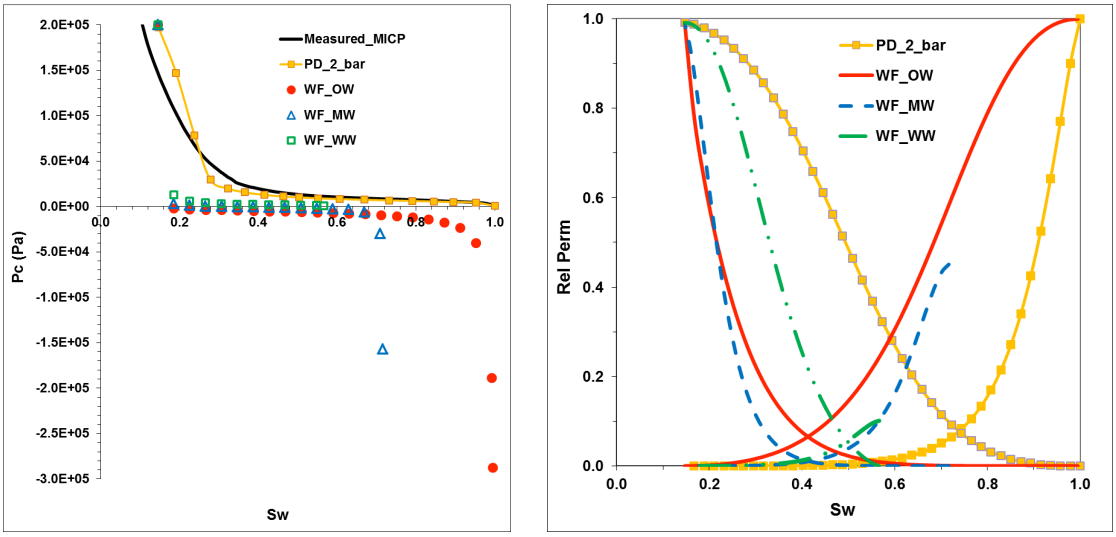

Figure 9: Capillary pressure and relative permeability sensitivity analysis waterflooding results for oil-wet (WF_OW), base case – mixed-wet (WF_MW) and water-wet (WF_WW)

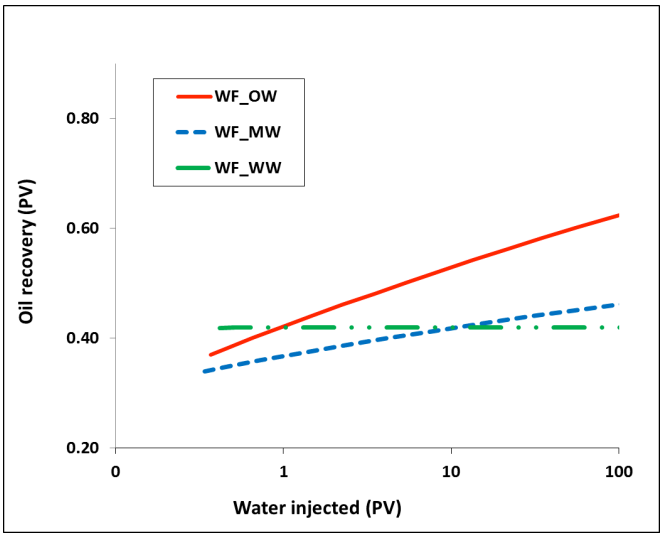

Figure 10: Oil recovery in pore volume (PV) versus PV of water injected using 1-D Buckley-Leverett analysis for the relative permeability curves depicted in Figure 9

ACKNOWLEDGMENTS

The authors acknowledge FEI Oil and Gas Business for permission to publish this paper and Hess Corporation, USA for allowing us to publish these data on their samples.

REFERENCES

1. Farokhpoor, R., Westphal, E., Idowu, N., *et al*., "Gas-water steady-state relative permeability determination with two approaches: experiment and digital rock analysis, strengths and weaknesses", Paper SCA2016-Temp_137, Proceedings of the 2016 SCA Symposium, Snowmass, Colorado, USA, 21 - 26 August, 2016.

2. Bakke, S., and P.E. Øren, "3-D pore-scale modelling of sandstones and flow simulations in the pore networks," *SPE Journal*, (1997), **2**, 136-149.
3. Øren, P.E., S. Bakke, and O.J. Arntzen, "Extending Predictive Capabilities to Network Models", SPE Journal, (1998), **3**, 324-336.
4. Morrow, N.R., "Wettability and its Effects on Oil Recovery", *J. Pet. Tech.* (1990), **42**: 1476-1484.
5. Amott, E., "Observations Relating to the Wettability of Porous Rock", *Trans. AIME*, (1959), **216**: 156-162.
6. Donaldson, E.C., Thomas, R.D. and Lorenz, P.B., "Wettability Determination and its Effect on Recovery Efficiency", *SPE Journal*, (1969) **9**: 13-20.
7. Andrew, M., Bijeljic, B., and Blunt, M.J., "Pore-scale Contact Angle Measurements at Reservoir Conditions Using X-ray Microtomography", *Advances in Water Resources*. (2014), **68**: 24-31.
8. Idowu, N., Long, H., Øren, P.E., *et al*., "Wettability analysis using micro-CT, FESEM and QEMSCAN and its applications to digital rock physics", Paper SCA2015-010, Proceedings of the 2015 SCA Symposium, St. John's Newfoundland and Labrador, Canada 16-21 August, 2015.
9. Aghaei, A., and Piri, M., "Direct pore-to-core up-scaling of displacement processes: Dynamic pore network modelling and experimentation", Journal of Hydrology, (2015), **522**, 488-509.
10. Sheppard, A.P., Sok, R.M. and Averdunk, H., "Techniques for Image Enhancement and Segmentation of Tomographic Images of Porous Materials", Physica A (2004), 339 (1-2), 145-151.
11. Latham, S, Varslot, T and Sheppard, A., "Image registration: Enhancing and Calibrating X-ray Micro-CT Imaging", Paper SCA2008-35, Proceedings of the 2008 SCA Symposium, Abu Dhabi, UAE, 29 October – 2 November, 2008.
12. Idowu, N., Nardi, C., Long, H., *et al*., "Pore-Scale modelling: Effects of network properties on predictive capabilities", Paper SCA2012-35, Proceedings of the 2012 SCA Symposium, Aberdeen, Scotland, UK, 27-30 August, 2012.
13. Øren, P.E. and Bakke, S., "Process Based Reconstruction of Sandstones and Prediction of Transport Properties", *Transport in Porous Media*, 2002, **46**, 311-343
14. Lopez, O., Mock, A., Øren, P.E., *et al*., "Validation of Fundamental Carbonate Reservoir Core Properties Using Digital Rock Physics" Paper SCA2012-19, Proceedings of the 2012 SCA Symposium, Aberdeen, Scotland, UK, 27-30 August, 2012.
15. Buckley, S.E., and Leverett, M.C., "Mechanisms of fluid displacement in sands", Trans. AIME, (1942), **146**, 107–116

AN IMPROVED INSIGHT INTO LOW-SALINITY WATERFLOODING: IN-SITU CHARACTERIZATION OF WETTABILITY ALTERATION AT ELEVATED PRESSURE AND TEMPERATURE CONDITIONS

M. Khishvand, A.H. Alizadeh, I. Oraki Kohshour, M. Piri
Department of Petroleum Engineering, University of Wyoming, Laramie, WY 82071, USA
This paper was prepared for presentation at the International Symposium of the Society of Core Analysts held in Snowmass, Colorado, USA, 21-26 August 2016

ABSTRACT

Low-salinity waterflooding (LSWF) is known as one of the most effective improved oil recovery techniques that could result in significant additional recovery compared to conventional high-salinity waterflooding (HSWF). Although numerous laboratory studies have confirmed the effectiveness of LSWF under specific conditions, they have mostly failed to present explicit evidences on the pore-level mechanisms that are responsible for the observed improvement in recovery. In this study, we investigated LSWF production mechanisms using X-ray micro-computed tomography (micro-CT) and examined recovery trends at the pore scale. Two core-flooding experiments were performed on miniature reservoir sandstone core samples at elevated pressure and temperature conditions. The preserved core samples (5 mm in diameter) were cut and then saturated to establish reservoir initial saturation conditions. The samples were subsequently waterflooded with low- and high-salinity brines and imaged using a micro-CT scanner. Micro-CT images were then used to obtain fluid saturations and three-dimensional maps of fluid occupancy during each experiment. High-resolution micro-CT images were also analyzed to measure pore-scale contact angles and study in-situ wettability and its impact on oil mobilization during different stages of waterflooding process.

The results highlight a significantly improved performance in LSWF compared to that of HSWF. The LSWF test showed more prolonged oil recovery response and gradual recovery at later stages while the HSWF recovery stabilized much earlier. Pore-scale contact angle measurements yielded direct evidence of wettability alteration from weakly oil-wet toward weakly water-wet conditions during LSWF; however, no considerable changes were observed in in-situ contact angles during the HSWF. Investigation of fluid occupancy maps along with in-situ characterization of wettability allowed us to establish a significantly better understanding of pore-scale mechanisms responsible for improved recover by LSWF.

INTRODUCTION

Waterflooding has been frequently implemented as an improved oil recovery (IOR) method to maintain reservoir pressure and sweep oil toward production wells. This technique was first practiced in 1880 [1] and since then has been adopted as one of the

most widespread methods for oil recovery. Due to the success of this IOR scheme in numerous oilfields, a large number of studies have targeted different aspects of waterflooding. Yildiz and Morrow [2] found that reservoir wettability and composition of injected and connate brines considerably affect waterflood recovery. These findings immediately inspired scientists to focus on composition and salinity of injected brine as the only controllable parameters to obtain higher waterflood efficiency. Primary research on outcrop Berea sandstone samples revealed that reducing salinity of the injected brine had a substantial effect on the amount of trapped oil saturation [3 and 4]. This method, so called low-salinity water flooding (LSWF), soon became one of the most promising IOR techniques. It was observed that LSWF resulted in remarkably higher recoveries in both sandstone [5] and carbonate [6] rock samples. In some cases, single well tracer tests [8] proved the favorable laboratory results. LSWF can be performed under secondary mode (at initial water saturation) or tertiary mode (at waterflood residual oil saturation). Either way, it may offer notably higher recovery efficiency compared to high-salinity waterflooding (HSWF). During the last decade, numerous laboratory tests have been conducted to evaluate the effectiveness of LSWF, investigate conditions under which LSWF succeeds, and describe displacement mechanisms governing LSWF recovery. The observations have demonstrated that the success of LSWF is greatly influenced by the original reservoir wettability and fluids present in the pore space (i.e., connate brine and crude oil). Tang and Morrow [3] reported three conditions that are necessary, but not sufficient, to observe low-salinity effect (LSE). These include significant clay content, presence of connate water, and exposure to crude oil to make a mixed-wet condition. Although some studies have shown the LSE for clay-free sandstone [9] and carbonate samples [7], these three conditions are universally pervasive to select candidate reservoirs for LSWF.

To perform successful LSWF, the underlying displacement mechanisms responsible for LSE must be comprehensively understood. Over the years, many research studies have been devoted to probe physical phenomena and displacement mechanisms that explain the higher recovery of LSWF and enrich the fundamental understanding of the LSE; but still, no consistent and systematic answers have been presented [3]. Results of core-flooding experiments, such as saturation trends, effluents analysis, and pressure drop data have been used to provide some indirect evidences supporting mechanisms of the LSWF process. Most of these studies have discussed several main hypotheses supporting the observed increases in recovery during LSWF. The most well-known mechanisms are detachment and migration of mixed-wet clay fines [2] and associate wettability alteration [3, 10, and 11], multicomponent ion exchange (MIE) between the low-salinity brine (LSB) and clay surfaces [4 and 12], mineral dissolution [13], and saponification [7]. Among these, wettability alteration (due to limited release of mixed-wet clay fines and/or MIE) from mixed-wet toward increased water-wetness is one of the most supported and frequently suggested mechanisms. When an oil-wet rock surface is exposed to LSB, water destabilizes the clays, acts as a wettability modifier, and changes the wettability toward increased water-wetness. This indeed allows oil to be displaced from the oil-wet pores [11]. Although there have been some attempts based on pore-scale theoretical

models to explain the pore-scale subtleties of this phenomenon [11], no rigorous pore-scale experimental observations have been presented in this regard, and hence pore-scale explanation of displacement mechanisms that govern higher recovery of the LSWF remain as a question that has yet to be answered.

For years, scientists have performed macro-scale tests to probe the above-mentioned mechanisms, but have not been able to directly observe the rock-fluid interactions, such as wettability alteration, and dynamic reactive interplays occurring at the pore scale. This, perhaps is the most significant shortcoming of those studies. Recently, however, image-based techniques such as micro-computed tomography (micro-CT) imaging has been employed to eliminate the drawbacks associated with macro-scale tests. Micro-CT imaging is a technology by which a rock sample is imaged to map its internal morphology and pore-scale fluid occupancy during different flow processes [14-16]. Using this new technology, one can look inside the pore space during LSWF, monitor potential changes in wettability and saturation trends, and obtain direct observations of governing mechanisms for the LSE. A few research groups have attempted to take advantage of microtomography along with scanning electron microscope (SEM) imaging technique to observe mineral dissolution and fines migration during LSWF [9 and 13] and some successes have been achieved. However, due to technical difficulties and limitations of experimental procedures used, microtomography has not been used to investigate potential in-situ wettability alteration and its associated displacement events as, perhaps, the most important mechanism responsible for LSE.

In this work, we endeavoured to exploit micro-scale images generated during LSWF experiments to investigate wettability alteration and provide observational clues tying the in-situ wettability with governing displacement mechanisms. An extensive laboratory study was deployed on reservoir sandstone samples and using reservoir crude oil at reservoir conditions. We assembled a unique miniature core-flooding apparatus, which could be employed to perform experiments at reservoir conditions while the core holder is placed inside a micro-CT scanner and the sample is imaged in the course of the experiments. We carried out two sets of experiments (one HSWF and one LSWF) to first examine the efficiency of the LSWF compared to that of HSWF in reservoir sandstone samples, and secondly to investigate the potential wettability alteration during LSWF in order to develop a better understanding of the pore-scale displacement mechanisms responsible for LSE. We used an effective approach to directly measure in-situ contact angles in individual pores. In-situ wettability data along with spatial distribution maps of fluid phases were used to shed light on the displacement events responsible for LSE.

Experimental

In this section, we describe the rock samples and fluids used to perform the experiments. We then discuss the experimental setup utilized to conduct the tests followed by the experimental procedure.

Rock Samples

We performed the core-flooding experiments on nominally 5-mm diameter and 50-mm long miniature reservoir sandstone core samples labeled as Samples A and B. The samples were taken parallel to bedding from a 110-mm diameter preserved reservoir core sample. The parent core sample was loosely consolidated and extra effort was made to drill smooth miniature core samples. Air was used as a coolant to minimize disturbances to the samples. All samples were dry-cut, instantly placed into the core holder, and then undergone their corresponding experimental procedure. Additionally, a 25.4-mm core plug (Sample C) and an end trim (Sample D) were cut from the same parent core. Sample C was used to measure initial water saturation (S_{wi}) using dean-stark method. Dean-stark measurement showed S_{wi} of 13% for the preserved core after drilling. This sample was then solvent-cleaned and its porosity and permeability were measured. Sample D was used for XRD analysis that showed about 6% clay content, mainly kaolinite. The presence of connate water and the significant clay content suggested that this rock might be a good candidate for LSWF. For Samples A and B, porosity was measured using micro-CT images. Uniform porosity distributions (see Figure 1) verified the homogeneity of the samples. Geometrical and petrophysical properties of the rock samples are listed in Table 1.

Fluids

High-salinity brine (HSB) was synthetized using sea water formulation with a total dissolved solid (TDS) of 40,300 ppm. The synthetic brine was prepared by including most of the ions in order to replicate the sea water composition as closely as possible. This brine was then diluted with a ratio of one-fiftieth and utilized as the LSB. The oil phase was reservoir stock tank oil (i.e., dead crude oil). Crude oil was filtered through a 0.5-μm filter before use to remove residue and debris. We then added 6 vol. % diiodomethane as X-ray dopant to ensure sufficient contrast between the crude oil and aqueous solution in X-ray images. Since we used ethane in the course of the experiments, one could argue possible asphaltene precipitation when the crude oil came into contact with ethane. To investigate this, we mixed 10 cc of the crude oil with 50 cc of ethane in a high-pressure cell and frequently shacked the container at experimental conditions (i.e., 1000 psi and 60 °C) for a day. The fluid mixture was then removed and the precipitated asphaltene was measured. The test showed 0.29 wt.% of asphaltene precipitation, which was negligible and did not introduce any adverse uncertainties into the experiments. Density and viscosity of all fluids were either measured at experimental conditions or estimated from data available in the literature [18-20]. Fluid properties are summarized in Table 2.

Experimental Setup

We employed a unique experimental apparatus to carry out the micro-scale core-flooding tests at elevated pressure and temperature conditions. The core-flooding was integrated with a high-resolution micro-CT scanner to image the core samples in the course of the experiments. The experimental setup composed of four dual cylinder Quizix^{TM} pumps, a miniature core holder, a micro-CT scanner, Rosemount pressure transducers, and

appropriate heating systems. All wetted parts of the core-flooding system were made out of Hastelloy™, titanium, and other corrosion resistant material. Figure 2 exhibits a schematic diagram of the flow system used in this study. Pumps 1 and 2 withdrew brine and oil, respectively, from buckets, and injected them into the core samples. Fluids could be pressurized with their respective pumps and passed through controllable heat exchangers to reach desired temperatures prior to injection. Pump 3 received the effluents at desired constant pressures and kept the pore pressure stable. A net overburden pressure was maintained during all experiments using Pump 4. The custom-built core holder was fabricated from composite materials with minimum X-ray absorption. It had nozzles that directed the fluids from Pumps 1 and 2 into the core and from the core to the back pressure pump (i.e., Pump 3). A special heating system was coupled with the core holder and the flooding system to heat up the flooding vessels during the experiments. All lines were insulated to maintain the fluid temperature and minimize potential flow distortions due to the changes in the temperature. Further details of the core-flooding system can be found elsewhere [17].

Experimental Procedure

To conduct each experiment, the core sample was first cut and instantly loaded in the miniature core holder. A low (for easier access to the pore space) net confining pressure was applied. The sample was then flooded with ethane to remove bulk air from the pore space. The ethane flooding was performed at 100 psi back pressure and at moderately low gas flow rates to minimize the risk of vaporization of the connate brine. The sample was then scanned to capture a reference image. Afterward, pore pressure was reduced and the dead crude oil was introduced into the sample. When crude oil breakthrough and removed some of the bulk ethane, pore and net confining pressures were simultaneously increased to 800 and 900 psi, respectively. At this step, temperature of the system was gradually increased to 60 °C. These temperature and pressure conditions were fixed until the end of the experiment. The oil was allowed to remove ethane thoroughly with a miscible displacement process. Once the flow of oil was established, oil injection was continued for a day with a very low flow rate to ensure no ethane was left in the pore space. The core was frequently scanned for any evidence of hydrocarbon gas. When zero gas saturation was confirmed by the CT images, a scan was run to determine the initial water saturation profile along the sample. Thereafter, the core was flooded with desired brine at a pre-specified flow rate of 0.004 cc/min. The flow rate was equivalent to capillary numbers of 1.42E-07 and 1.48E-07 for LSWF and HSWF tests, respectively. Brine was injected with increments of 0.5 pore volume (at the outset of the experiment) and 1 pore volume (at the end). After each increment, we halted brine injection and the system was let come to rest. The middle section of the core sample, hereafter referred to as field of view (FOV), was then scanned. The final stage of each waterflood was achieved when the fluid occupancy no longer changed even by doubling the brine flow rate. Image sets were then reconstructed as form of stacked slices and prepared for analysis.

IMAGE ANALYSIS

The tomographic images obtained during the experiments were analyzed to map fluid occupancy and measure trapped oil saturation as well as fluid-rock properties. The image set captured at each stage of the experiments was segmented after registration with the reference image. The segmented data was used to characterize in-situ wettability by means of oil-brine contact angle measurement. This provided a platform to study the potential wettability alteration in the rock and the displacement mechanisms responsible for the LSWF recovery. A detailed explanation of the segmentation method and the procedure for contact angle measurements can be found elsewhere [14-16].

RESULTS AND DISCUSSION

In this section, we present the results of the micro-scale LSWF and HSWF experiments performed on Samples A and B. For each experiment, we used pore-scale fluid occupancy maps generated utilizing the micro-CT images to study displacement mechanisms and resulting saturation trends. This allowed us to highlight the efficiency of the LSWF compared to that of HSWF in the targeted rock samples. Furthermore, we characterized in-situ wettability at different stages of each flow process to probe potential wettability alteration during the LSWF. Finally, we attempted to connect the in-situ wettability alteration and its consequent pore-scale displacements with the saturation trends observed.

Pore-Scale Fluid Occupancy and Saturation

Figures 3 and 4 exhibit pore-scale fluid occupancy maps of the core samples subjected to the LSWF and HSWF, respectively. Each figure contains several images corresponding to different stages of each flow test and exemplifies the displacement events taking place in the pore space. As seen in Figures 3a and 4a, the pore space was dominantly occupied by oil before the commencement of the waterfloods. Oil almost entirely filled the large and medium-sized (mostly oil-wet) pores. Water, however, resided in very small (mostly water-wet) pores and crevices. This fluids arrangement established the initial mixed-wet conditions of the samples. As waterflooding initiated (Figures 3b for the LSWF and 4b for the HSWF), in both samples, water invaded into fully and partially oil-filled elements by two mechanisms. It displaced oil through imbibition from water-wet pores (with an order of smallest to largest) and upon drainage from oil-wet pores (with an order of largest to smallest). This could be realized when one compares Figures 3b and 4b with 3a and 4a. Water, initially, invaded into small water-wet pores (squares) and large oil-wet pores (circles) while medium-sized pores remained oil-filled. In other words, the oil clusters sitting in the medium-sized pores were the last ones to be mobilized by water. As waterflood proceeded (Figures 3c and 4c), water had more accessibility to the entrance of the oil-filled pores and hence, it invaded into a greater number of them including some medium-sized ones. Meanwhile, oil gets trapped in some pore elements depending on wettability and fluids present in the neighbouring elements. Finally, the waterfloods ended at a point that the remaining oil was entirely trapped (i.e., disconnected). This point, known as waterflood end point, signified the efficiency of the waterfloods. Comparison between Figures 3c and 3d and 4c and 4d revealed that the end point was

established after about 5 pore volumes of water injection (PVWI) for the HSWF; however, in the case of the LSWF, end point was obtained much later and pronounced changes in oil occupancy were observed even in late stages (until about 10 PVWI).

To determine the end points and examine the efficiency of the LSWF, saturation values were calculated over the FOVs for both waterfloods. The results are presented in Figure 5 for stages with the most considerable variations. Before waterflooding, initial oil saturations ($S_{oi} = 1 - S_{wi}$) were homogenous along the FOV and had very similar average values for both samples (about 0.91 and 0.90 for Samples A and B, respectively). These values were also consistent with the S_{oi} measured using dean-stark method for Sample C (i.e., 87%). After 5 PVWI, oil saturations were reduced in both samples with similar trends resulting in *remaining* oil saturations (S_{or}) of 0.46 and 0.45 for Samples A (LSWF) and B (HSWF), respectively. This in fact indicated similar initial recoveries of the LSWF and HSWF. Upon continuation of the waterfloods, for the HSWF, S_{or} stabilized and no further considerable oil production was observed, even with an increase in flow rate to 0.006 cc/min; therefore, this point was considered as wateflood residual oil saturation (S_{orw}) for the HSWF. In contrast, for the LSWF, S_{or} continued to reduce significantly at the later stages of waterflooding (until 10 PVWI) resulting in a S_{orw} of 0.30. These observations demonstrated that the LSWF had a considerable gradual recovery at later stages whereas the high-salinity production stabilized much earlier. These differences in recovery trends, known as LSE, are in line with our earlier observations of water-displacing-oil events in medium-sized pores occurred during the late stages of the LSWF (Figure 3d). We believe that when low-salinity brine contacted the rock surface, it changed the wettability toward increased water-wetness (see more details listed later in this section). The wettability alteration might be attributed to either migration of clay minerals or multiple ion exchange [3 and 5]. LSB gradually altered the wettability of the rock and as a consequence facilitated invasion of water into medium-sized oil-filled pores (see the rectangular area shown in Figure 3d). To verify this hypothesis, one would need to investigate whether wettability alteration does take place during the LSWF and how the potential alteration impacts oil displacement. In the next section, we explore this by means of in-situ wettability measurement and pore-scale investigation of displacement events motivated by potential wettability alteration.

In-Situ Characterization of Wettability Alteration

We accomplished a detailed analysis of the micro-scale images to find potential changes in wettability during different flooding scenarios. For each flooding step, the segmented data was analyzed to measure oil-water contact angles. The detailed methodology of the contact angle measurement can be found elsewhere [15 and 16]. We limited our measurements to contact angles at main terminal menisci (i.e., oil-water interfaces at the center of pore-throat junctions). Since we imaged the samples after the fluids were let to come to rest, contact angle measurements were considered to give equilibrium values. One should note that it was impractical to measure contact angles in very small (mainly water-wet) pores because the amount of oil present in those pores was extremely small. Contact angle measurement results presented in Figure 6 are for three stages of each

waterflood (i.e., after 0.5, 5, and 10 PVWI). Contact angle values show a distribution for each stage, which might be attributed to local mineral heterogeneity and microscopic surface roughness. As it can be observed, initial contact angle values (i.e., after 0.5 PV) showed similar distributions as well as mean values for the LSWF and HSWF. The average values of about 115 and 117 degrees for the LSWF and HSWF, respectively, verified a weakly oil-wet condition in the preserved samples. This figure also demonstrates that contact angles did not change during the course of HSWF, while substantial changes toward increased water-wetness occurred during the LSWF (from 115 to 89°). As the LSWF proceeded, LSB may have reacted with the clay minerals lining the rock surface. It has been hypothesized that LSB may detach the mixed-wet clay particles from the pore walls [3] and exchange divalent ions (such as Ca^{2+}) with the clays [5]. Both mechanisms may have contributed to the observed reduction in the oil-water contact angle. The bimodal graphs shown in Figure 6 (after 5 and 10 PV LSWF) indicate that contact angle could change significantly in some pores whereas others might show only slight alterations compared to their initial wettability condition. This might arise from several key factors such as different contact time and contact areas with the LSB as well as variable clay content of the pores.

Additional analysis of the pore-scale contact angles could further corroborate the displacement events that were discussed earlier as a consequence of wettability alteration during LSWF. Figure 7 depicts two-dimensional views of fluid occupancy in an individual pore and the corresponding measured contact angles after 0.5, 5, and 10 PVWI. This figure illustrates that water had access to the entrance of an oil-filled element in all stages, but interestingly, the pore was only invaded by water when the contact angle decreased. This can be explained by threshold capillary pressure concept [11]. Upon changes in wettability from 127 (after 0.5 PVWI) to 99 (after 5 PVWI), the threshold water pressure needed for the drainage process (i.e., water-displacing-oil in this oil-wet pore) was reduced, which in turn enabled water to proceed in the pore and displace the oil in the later stages (i.e., between 5 and 10PVWI). We believe that these changes in wettability and subsequent invasion of water into medium-sized oil-wet pores directed the gradual production of oil at late stages of the LSWF and were responsible for higher oil recovery of the LSWF. This study provided, for the first time, direct evidences of wettability alteration due to LSE and associated pore-scale mechanisms governing the greater recovery established by LSWF.

CONCLUDING REMARKS

In this study, we performed a LSWF and a HSWF micro-scale experiments on preserved reservoir sandstone core samples with reservoir fluids and at elevated pressure and temperature conditions. The preserved samples were cut and saturated using a special procedure to establish initial reservoir saturation. The samples were then flooded under secondary mode using brine with different salinities. We imaged the fluid occupancy in the pore space and used the images to characterize oil saturation and in-situ wettability as well as probing the physical mechanisms responsible for LSE.

The results indicated waterflood residual oil saturations (S_{orw}) of 0.30 and 0.45 for the LSWF and the HSWF, respectively. These observations highlighted the significant performance of LSWF compared to HSWF in our study. LSWF showed more prolonged oil recovery response (gradual recovery at later stages) while the HSWF recovery curve stabilized much earlier. Analysis of micro-CT images enabled us to measure pore-scale contact angles to examine wettability alteration of the rock surface. These measurements coupled with pore-scale fluid occupancy maps revealed that when the rock surface was exposed to low-salinity brine, the average oil-water contact angle gradually reduced toward neutral-wet condition (i.e., from 115 to 89), which in turn lowered the threshold water pressure needed to displace oil in the oil-wet pores. As a consequence, water invaded into more oil-filled pores and increased recovery at the later stages of the LSWF.

ACKNOWLEDGEMENTS

We gratefully acknowledge financial support of Hess Corporation and the School of Energy Resources at the University of Wyoming.

REFERENCES

1. Carll J. F., "The geology of the oil regions of Warren, Venango, Clarion and Butler Counties", Report III, Harrisburg, Pennsylvania, 1880.
2. Yildiz, H. O., Valat, M., and Morrow, N. R., "Effect of brine composition on wettability and oil recovery of a Prudhoe Bay crude oil", *Journal of Canadian Petroleum Technology,* (1999), 38, 01.
3. Tang, G. Q., and Morrow, N. R., "Salinity, temperature, oil composition, and oil recovery by waterflooding", *SPE Reservoir Engineering,* (1997), 12, 04, 269-276.
4. Morrow, N. R., and Buckley, J., "Improved oil recovery by low-salinity waterflooding", *Journal of Petroleum Technology*, (2011), 63, 05, 106-112.
5. Lager, A., et al., "Low salinity oil recovery - An experimental investigation", *Petrophysics,* (2008), 49, 01.
6. Fathi, S. J., Austad, T., and Strand, S., "Water-based enhanced oil recovery (EOR) by "smart water": Optimal ionic composition for EOR in carbonates", *Energy & Fuels*, (2011), 25, 11, 5173-5179.
7. Jerauld, G. R., et al., "Modeling low-salinity waterflooding", *SPE Reservoir Evaluation & Engineering,* (2008), 11, 06, 1000-1012.
8. McGuire, P. L., et al., "Low salinity oil recovery: An exciting new EOR opportunity for Alaska's North Slope", SPE Paper 93903 *presented at the SPE Western Regional Meeting*, 30 March-1 April 2005, Irvine, California.
9. Fogden, A., et al., "Mobilization of fine particles during flooding of sandstones and possible relations to enhanced oil recovery", *Energy & Fuels*, (2011), 25, 4, 1605-1616.
10. Austad, T., RezaeiDoust, A., and Puntervold, T., "Chemical mechanism of low salinity water flooding in sandstone reservoirs", SPE Paper 129767 *presented at the SPE Improved Oil Recovery Symposium,* 24-28 April 2010, Tulsa, Oklahoma.

11. Sorbie, K. S., and Collins, I., "A proposed pore-scale mechanism for how low salinity waterflooding works", SPE Paper 129833 *presented at the SPE Improved Oil Recovery Symposium*, 24-28 April 2010, Tulsa, Oklahoma.
12. Lebedeva, E. V., and Fogden. A., "Micro-CT and wettability analysis of oil recovery from sand packs and the effect of waterflood salinity and kaolinite", *Energy & Fuels*, (2011), 25, 12, 5683-5694.
13. Pu, H., et al., "Low-salinity waterflooding and mineral dissolution", SPE Paper 134042 *presented at the Annual Technical Conference and Exhibition*, 19-22 September 2010, Florence, Italy.
14. Alizadeh, A.H., et al., "Multi-scale experimental study of carbonated water injection: An effective process for mobilization and recovery of trapped oil", *Fuel*, (2014), 132, 219-235.
15. Khishvand, M., Akbarabadi, M., and Piri, M., "Micro-scale experimental investigation of the effect of flow rate on trapping in sandstone and carbonate rock samples", *Advances in Water Resources*, (2016), in press.
16. Khishvand, M., Alizadeh, A.H., and Piri, M., "In-situ characterization of wettability and pore-scale displacements during two- and three-phase flow in natural porous media", *Advances in Water Resources*, (2016), under revision.
17. Alizadeh, A.H., and Piri, M., "The effect of saturation history on three-phase relative permeability: An experimental study", *Water Resources Research*, (2014), 50, 1636-64.
18. Morrow, N. R., "Interfacial phenomena in petroleum recovery", *Surfactant Science Series*, V26, CRC Press, 1990.
19. Kestin, J., Khalifa, H. E., and Correia, R. J., "Tables of the dynamic and kinematic viscosity of aqueous NaCl solutions in the temperature range 20-150°C and the pressure range 0.1-35 MPa", *Journal of physical and chemical reference data*, (1981), 10, 1, 71-88.
20. Amin, R., and Smith, T. N., "Interfacial tension and spreading coefficient under reservoir conditions", *Fluid phase equilibria*, (1998), 142, 1, 231-241.

Table 1- Geometrical and petrophysical properties of the rock samples used in this study.

Sample	Experiment	D & L (mm)	Porosity (%)	Air permeability (mD)
A	LSWF	4.6 & 52	28.32	-
B	HSWF	4.64 & 51	28.97	-
C	Dean-Stark	25.4 & 80	28.37	165
D	XRD analysis	End trim	-	-

Table 2- Physical properties of the fluids used in this study.

Fluid	Experiment	Viscosity at 60°C and 1000 psi (cP)	Density at ambient condition (g/cc)
Low-salinity brine	LSWF	0.3664*	0.999
High-salinity brine	HSWF	0.3836*	1.029
Crude oil	HSWF and LSWF	3.48	0.857

*Estimated from data available in the literature [18-20].

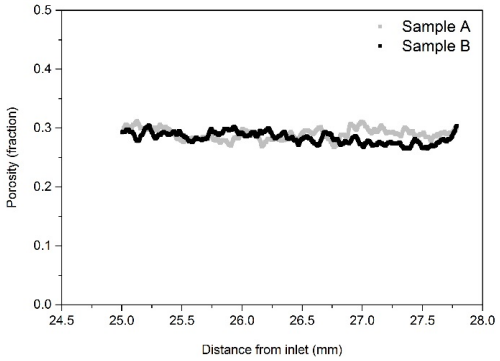

Figure 1 - Porosity distributions along the length of Samples A and B obtained using micro-CT images.

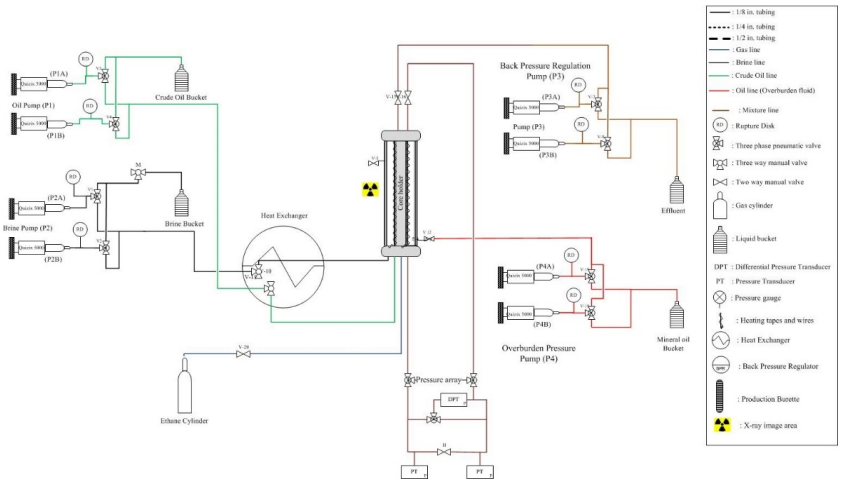

Figure 2 - A schematic diagram of the core-flooding apparatus used in this study.

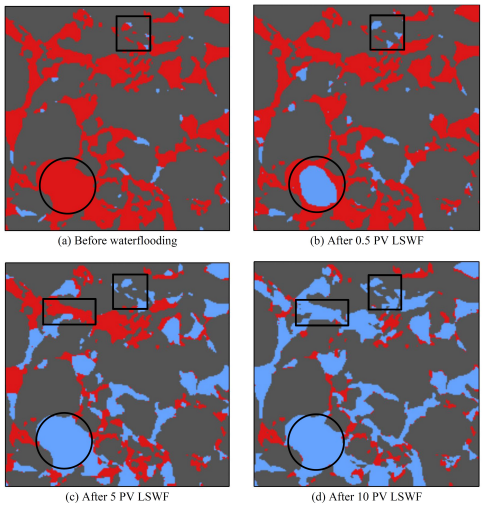

Figure 3 - Visualization of pore-scale fluid occupancies generated at different stages of LSWF experiment (resolution = 1.64 µm; blue: water, red: oil, and gray: solid).

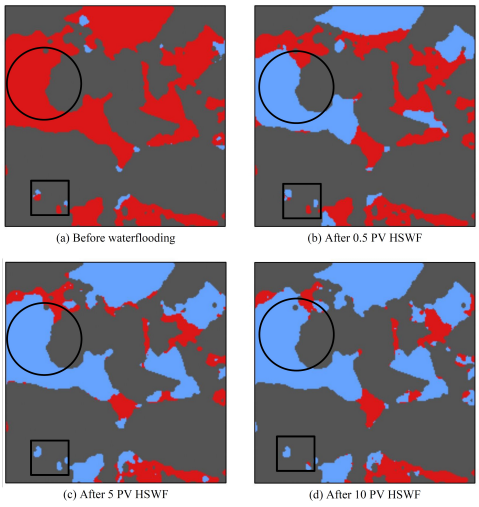

Figure 4 - Visualization of pore-scale fluid occupancies generated at different stages of HSWF experiment (resolution = 1.64 µm; blue: water, red: oil, and gray: solid).

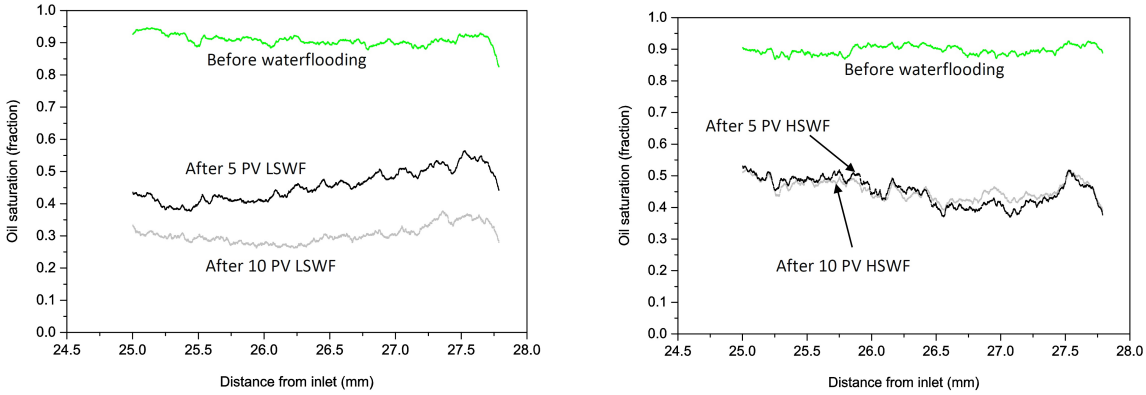

Figure 5 - Oil saturation distributions along the FOV at different stages of LSWF (left) and HSWF (right) tests.

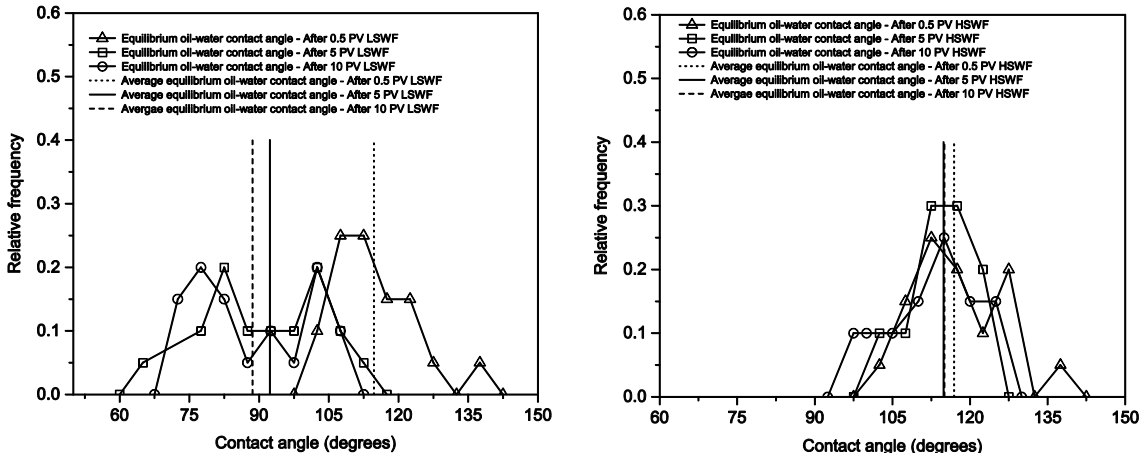

Figure 6 - Histograms of in-situ contact angle distributions during different stages of LSWF (left) and HSWF (right) tests.

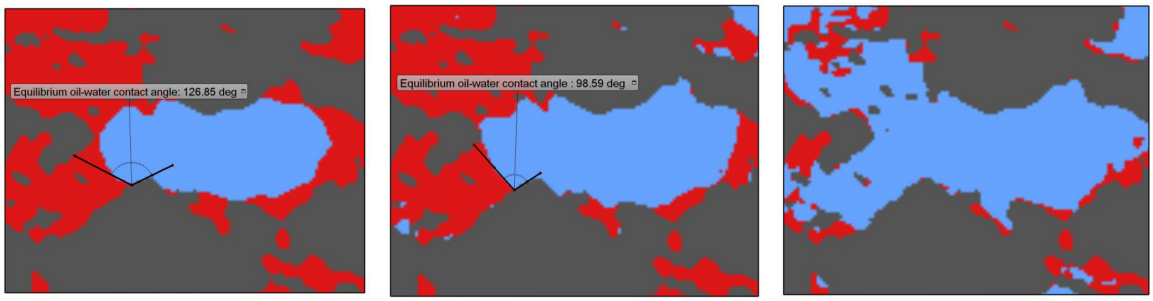

(a) After 0.5 PV LSWF (b) After 5 PV LSWF (c) After 10 PV LSWF

Figure 7 - Two-dimensional cross-sectional views of pore-scale fluid occupancy during primary LSWF test performed on a preserved reservoir sandstone sample (resolution = 1.64 μm; blue: water, red: oil, and gray: solid). The images show changes in wettability during the LSWF and the subsequent invasion of water into an oil-filled pore.

WETTABILITY EFFECTS ON OSMOSIS AS AN OIL MOBILIZATION MECHANISM DURING LOW SALINITY WATERFLOODING

S.B. Fredriksen[1], A.U. Rognmo[1], K. Sandengen[2], and M.A. Fernø[1]
[1]Department of Physics and Technology, University of Bergen, Norway
[2]Statoil ASA, Rotvoll, Trondheim, Norway

This paper was prepared for presentation at the International Symposium of the Society of Core Analysts held in Snowmass, Colorado, USA, 21-26 August 2016

ABSTRACT
This experimental study identifies osmosis as an oil mobilization mechanism during low salinity waterflooding using capillary tubes and micromodels with different wetting properties. Oil-wet capillary tube tests verify that oil acts as a semi-permeable membrane for water transport when separating brines of different salinity. Osmotic oil mobilization was investigated using two-dimensional silicon-wafer micromodels for direct optical visualization of fluid interactions. Water diffusion was identified as the main transport mechanism at strongly water-wet conditions and capillary equilibrium. Osmosis was observed at both strongly water-wet and oil-wet conditions influenced by the pore-level distribution of oil and water. At strongly water-wet conditions osmosis displaced oil by expanding water-in-oil emulsions. At oil-wet conditions low salinity water was transported by osmosis to otherwise inaccessible regions of high-saline brine. Osmotic oil mobilization is a fluid-fluid interaction and should therefore be present in both sandstone and carbonate reservoirs. The experimental results support this and provide evidence of osmotic water transport and oil mobilization under various wettability conditions.

INTRODUCTION
Low salinity waterflooding (LSW) denotes injection of diluted brine concentrations in either secondary or tertiary recovery mode to increase oil recovery. Whereas conventional waterflooding uses formation brine or seawater predominantly to maintain reservoir pressure, LSW improves microscopic sweep by injecting water with diluted salt concentrations [1]. LSW has been reported to enhance oil production in a series of coreflood experiments [2], and has been tested in various field operations, see *e.g.* [3]. There is a consensus that an optimal wetting preference exists at which LSW is favorable for oil recovery. LSW is generally expected to shift reservoir wettability towards more water-wet conditions.

The initial research on LSW emphasized on fluid-rock interactions and the mechanisms that alter wettability of a rock surface. Coreflood results in sandstone provided a variety of theories aiming at defining the low salinity effect (LSE), as summarized by Sheng [4]. One of the more accepted hypotheses is the concept of multi-component ion exchange

(MIE), where inorganic Ca^{2+} and Mg^{2+} cationic exchange, between the negatively charged sandstone and the injected low salinity water, replace organic polar components at the rock surface to shift wettability towards water-wet [5]. The influence of cationic exchange was partially confirmed by others, who also reasoned that a major contribution was reduction of ionic brine strength [3]. Reduced ionic strength lowers the cationic screening potential that result in electrostatic repulsion and expansion of the electrical diffuse double layers surrounding clay and oil particles. Oil is desorbed from the surface and the initial wetting state is altered [3].

When exposed to LSW, and contrary to the established hypotheses [3, 5], an increase in recovery is also demonstrated in carbonates [6, 7]. Carbonate reservoirs are preferentially oil-wet due to a net positively charged surface [8]. According to Ligthelm *et al*. [3], reducing the ionic brine strength should yield greater attraction between organic polar components and the positive carbonate surface causing stronger oil-wet conditions, not a shift towards water-wet. The capability for multi-component cationic exchange is also restricted considering the positively charged rock. The general understanding is therefore that the underlying mechanism of LSE is yet to be found or that various mechanisms exist for different crude-oil/brine/rock systems [4, 9, 10].

Osmosis had been largely overlooked as a plausible mechanism for improved oil recovery during LSW [10]. Osmosis is a thermodynamic driving force for water transport caused by a difference in chemical potential between two aqueous solutions separated by a semi-permeable membrane [11]. In their initial work, Sandengen and Arntzen [10] observed oil displacement when separating high –and low-saline solutions by an oil membrane. A further investigation using oil-wet and water-wet micromodels showed that the osmotic effect was influenced by water connectivity and it was believed that osmotic gradients could not be established at water-wet conditions [12]. More recently, however, it was found that osmosis may be active as a transport mechanism in water-wet systems [13].

Current experimental data, obtained in micromodels, support the theory of osmosis as a mechanism for pore-scale oil mobilization regardless of the crude-oil/brine/rock system. Osmosis may therefore contribute to oil mobilization in both sandstone and carbonate reservoirs. The experimental analysis herein confirm this hypothesis and compose a collective theory identifying osmosis as one of the contributing mechanisms for oil mobilization at pore-scale during LSW.

EXPERIMENTAL

Previous work on osmosis using water-wet capillary tubes could not clearly identify if water transport occurred through the oil bulk or by film-flow induced by interfacial tension [10]. In this study, oil-wet PTFE tubes are used to isolate and verify water transport by osmosis through the oil bulk. In addition, silicon-wafer micromodels replicating the two-dimensional pore-structure of natural sandstone are used to qualitatively observe fluid-fluid interactions when performing wettability studies on

osmotic oil mobilization during LSW. The strongly water-wet nature of the models is ideal for investigating osmosis by isolating known processes that occur during LSW *i.e.* wettability alteration towards more water-wet.

Fluids

Synthetic high-saline brines were made by adding given quantities of analytical-grade chemicals to deionized water (DIW), while pure DIW was used as low-saline brine. Oils were either toluene or crude oil (from a North Sea chalk reservoir). Toluene was used because of high water solubility to accelerate flux during osmosis. Colorants such as Oil Red O (red), Erinoglaucine disodium salt (blue) and Quinoline Yellow WS (yellow) were added at a concentration of ~0.05 wt% to optically distinguish the fluids at pore-scale by microscope. An overview of the fluids used and their characteristics are given in **Table 1**.

Table 1 – Chemical composition and characteristics of brines and oil phases.

Fluid ID	Composition	Ionic strength[1)] [M]	Osmotic pressure[2)] [bar]	Standard molar entropy[3)] [J/mol]	Interfacial tension w/Oil A [mN/m]
Brine A	5.0 M NaAc	5.0	124	138.2 (s)	14.0
Brine B	5.0 M NaCl	5.0	124	95.06 (aq)	25.3
Brine C	5.0 M $CaCl_2$	12.5	124	123.87 (aq)	22.5
Brine D	1.0 M NaCl	1.0	25	95.06 (aq)	20.4
DIW	Deionized water	0	0	69.95 (aq)	N/A
Oil A (Toluene)	C_7H_8	N/A	N/A	N/A	N/A
Oil B (Crude)	53 wt.% HC 35 wt.% aromatics 12 wt.% resins 0.9 wt.% asphaltenes	N/A	N/A	N/A	N/A
HMDS	>97% purity	N/A	N/A	N/A	N/A

1) Assume complete dissociation [14].
2) Assume non-electrolyte by Van't hoff equation [14]. Provides the maximum osmotic pressure that can develop in a solution when separated from deionized water.
3) The entropy contribution from one mole of substance at standard conditions [15].

Oil-wet capillaries for verifying osmotic water transport

To verify osmotic water transport a series of capillary tube tests were performed using oil-wet polytetrafluoroethylene (PTFE) tubes. The oil-wet nature restricts film flow along the surface, and water transport should occur only through the oil-phase by the osmotic gradient. Oil A was injected into the tube followed by high-saline Brine A and DIW on either side. A baseline without an osmotic gradient was also established using two water droplets of high-saline Brine A. The PTFE tubes were plugged and placed in an oven at 50 ºC for 20 days. Droplet movement was monitored and pictures were taken to document the process.

Micromodels for studying wettability effects on osmotic oil mobilization

Silicon-wafer micromodels representing natural sandstone were used to investigate the potential for osmotic oil mobilization by LSW at various wettability conditions. The

strongly water-wet micromodels replicate a porous network in connection to adjacent channels acting as fractures. One micromodel was prepared using high-saline Brine D as connate water and Oil B as the oil-phase. At strongly water-wet conditions the high-saline brine adhered to the pore walls and was continuous throughout the porous network. Another system was prepared to represent oil-wet conditions. Here, Brine C was used as the high-saline phase and Oil A as the oil-phase. The micromodels were rendered oil-wet using Hexamethyl-diasilazane (HMDS) according to the modification procedure described elsewhere [12].

When preparing the micromodels they were 100% saturated with Brine C or D as connate water. Oil drainage was performed using either Oil A or B. After drainage, secondary waterflooding was conducted using high-saline brine allowing spontaneous imbibition to act as the main driving force until capillary equilibrium was reached. Baseline tests were run prior to performing LSW through the adjacent channel establishing a salinity contrast to the matrix high-saline brine. LSW was maintained at a flow rate of 1ml/day to represent dynamic conditions through a fracture network with water transport to the matrix dominated by small-scale diffusion processes.

A microscopic setup was used for pore-level visualization. Experiments were performed at ambient temperature and pressure with the micromodels placed horizontally on the microscope platform. Syringe pumps were connected to fluid distribution ports for brine and oil injection. Field-of-view was carefully selected showing parts of the matrix and adjacent flow channel. A camera and computer with associated imaging-software connected to the microscope captured time-lapse-pictures for documentation and post-image processing. LSW lasted between 7 to 14 days for each test.

RESULTS

Osmotic water transport in oil-wet capillary tubes

The effect of a salinity gradient on water transport through a semi-permeable oil membrane using oil-wet capillary tubes is shown in **Figure 1**. The two image sequences show water transport of low-saline water (yellow) through the oil-phase (red) into the adjacent high-saline solution (white) over time. With a salinity gradient present (image 1), all of the low-saline water was transported through the oil-phase into the high-saline brine after 20 days. The increased volume and color-shift indicates the direction of water transport from the low salinity water to the high-saline brine. Without a salinity gradient water transport was not observed (image 2), although some volume changes occurred due to slow dissolution of water in toluene causing the high-saline droplets to shrink.

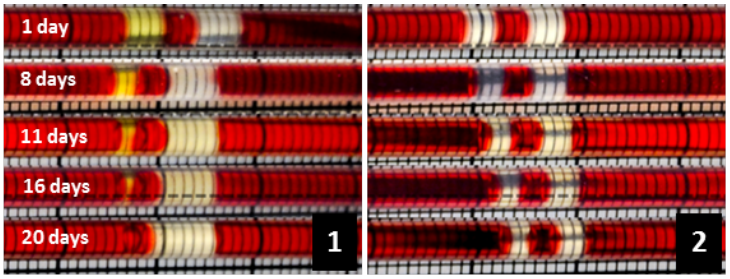

Figure 1. Osmotic water transport in oil-wet capillary tubes. The yellow phase is low salinity water, the red is the oil-phase and white is the high-saline brine. Time lapse images (1, 8, 11, 16 and 20 days) are shown from top to bottom. **1)** Osmotic gradients cause the low salinity water (yellow) to shrink as water is transported through the oil phase into the high-saline solution. **2)** The baseline result (*i.e.* high-saline solution only) showed no osmotic water transport only a slight dissolution of water into toluene.

The interfacial tension (IFT) between oil and water varies with salinity, and decreases upon dilution until reaching a minimum IFT at a critical salt concentration [16]. Hence, when two solutions with different salinity are separated by an oil-phase, an uneven balance is created across the oil-phase that may lead to convective water transport. IFT was measured for a combination of brines with Oil A (*cf.* Table 1). To determine water transport as an effect of osmosis only, combinations of Brine A, B and DIW were used in capillary-tube tests. Brine A has a lower IFT compared to Brine B and behaves qualitatively different in terms of capillary forces, but the two brines have the same ionic strength and osmotic gradient (*cf.* Table 1).

Table 2 provides an overview of the capillary tube tests performed with configurations of high – and low saline solutions separated by oil. Expansion of the reference solution is defined by "+", contraction by "-" and no change is termed "0". In all cases the observed results matched the direction of water transport predicted theoretically by osmosis.

Table 2 – Water transport in oil-wet capillary tube tests. The experimental results are correlated with theoretical predictions from interfacial tension and osmosis.

Reference solution	Opposing solution	Theoretical Prediction Osmosis	Theoretical Prediction Interfacial tension	Experimental Observation
Brine B	Brine B	0	0	0
Brine B	Brine A	0	-	0
Brine B	DIW	+	-	+
DIW	DIW	0	0	0
Brine A	DIW	+	+	+
Brine A	Brine A	0	0	0

Wettability effects on osmotic oil mobilization

Oil mobilization during LSW occurs in response to forward osmosis when a system is partially saturated with high-saline brine and oil [17]. Both strongly water-wet and oil-wet silicon-wafer micromodels were used to evaluate the influence of wettability on osmotic oil mobilization. To create a salinity contrast to the high-saline connate brine

LSW was injected through the adjacent fracture only. No fluid displacement was observed in baseline experiments, where the salinities of injected and connate brine were equal.

Strongly water-wet conditions

At strongly water-wet conditions the initial high-saline brine adhered to the pore walls creating a continuous water layer. Due to water connectivity and ceased capillary imbibition the main transport mechanism was water diffusion from the low salinity phase through film-flow diluting the high-saline connate brine. The increasing water-volumes within the porous network resulted in a redistribution of fluids and capillary trapped oil was viscously displaced into the fracture to give way for the preferred water phase. **Figure 2** shows how diffusion of low salinity water mobilized oil in a strongly water-wet system.

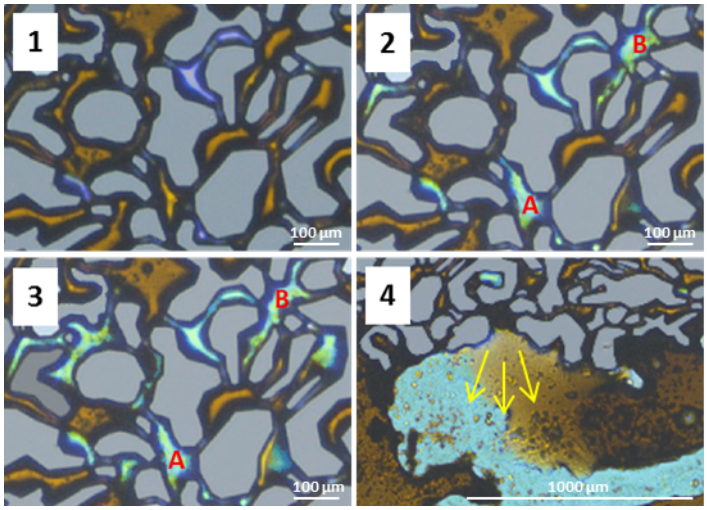

Figure 2. Low salinity water diffusion and oil mobilization. Oil B (crude oil, brown), Brine D (blue), DIW (turquoise) and rock grains (grey). Image 1-3 shows several pores, and Image 4 shows the fracture located below (different length scale). **1)** Initial fluid distribution. **2)** Diffusion of DIW through pore A and film-flow into pore B displacing oil to adjacent pores. **3)** Continued DIW oil displacement from several interconnected pores. **4)** Fluid redistribution leads to oil displacement into adjacent fracture (yellow arrows).

The osmotic effect was observed in small high-saline brine-droplets dispersed within the oil-phase indicated by the yellow arrows in **Figure 3**, image 1. These water-in-oil emulsions started to grow due to osmotic water transport during LSW and accumulated into larger emulsions by coalescence and Ostwald ripening. This growth was not observed without a salinity gradient (*i.e.* baseline). The continuous aggregation (image 2) embodied most of the oil-phase, slowly displacing it towards the lower channel and into connecting pore throats.

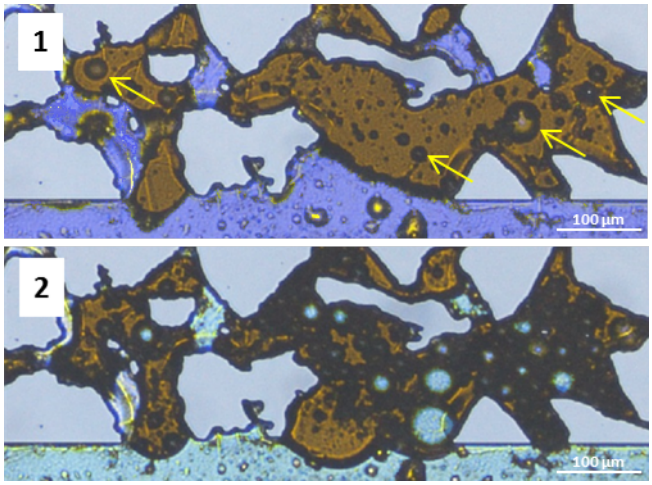

Figure 3. Oil displacement by osmotic water-in-oil expansion. Oil B (crude oil, brown), Brine D (blue), DIW (turquoise) and rock grains (grey). **1)** The fluid distribution prior to performing LSW. An oil-phase is located in the pore network in contact to the adjacent channel. Dissolved droplets of high-saline brine within the oil are indicated by the yellow arrows. **2)** During LSW, the water-in-oil emulsions start to grow and the aggregation of emulsions displace the oil-phase.

Oil-wet conditions

At oil-wet conditions, osmotic gradients were established when the low salinity water contacted the oil-phase leading to swelling of capillary trapped high-saline brine. **Figure 4** shows expansion of capillary-trapped brine (blue) and subsequent oil (orange) mobilization by osmosis. As the capillary trapped connate brine expanded the oil was displaced towards the flow channel as indicated by the yellow arrows in image 2. The oil-phase was mobilized into the fracture when the viscous pressure from brine expansion exceeded the capillary pressure withholding oil in matrix (image 3).

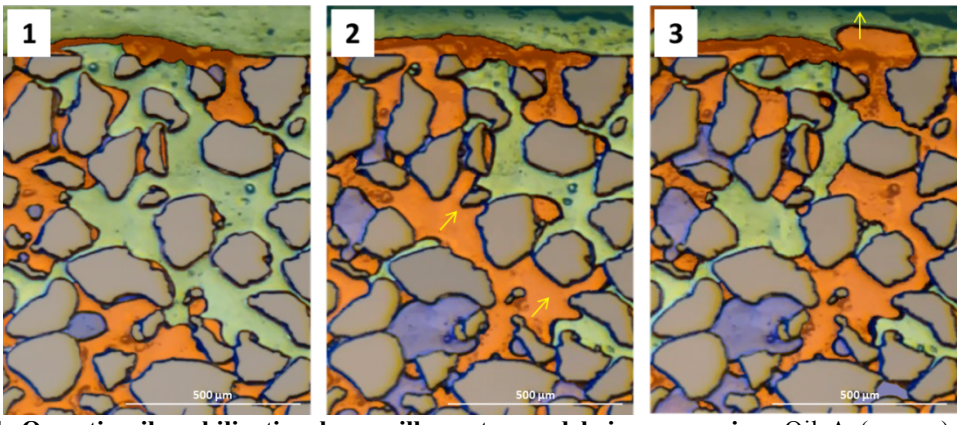

Figure 4. Osmotic oil mobilization by capillary- trapped brine expansion. Oil A (orange), Brine C (blue), DIW (turquoise) and rock grains (grey). **1)** Fluid configuration after initiating LSW. Capillary trapped regions of high-saline brine are found within the oil-phase. **2)** The high-saline regions start to expand in response to osmotic induced water transport mobilizing oil towards the fracture by the yellow arrows. **3)** Oil is produced from the porous medium and into the nearby flow channel.

DISCUSSION

Verification of osmotic water transport in capillaries

The oil-wet capillary tube tests represent a situation where stagnant pockets of connate water, either through snap-off or bypassed, are surrounded by oil. The direction of water transport observed in **Figure 1** matched prediction by osmosis, and suggests limited influence of salinity effects on IFT. This is also corroborated by previous qualitative observations in water-wet micromodels [10]. Rate of oil mobilization by osmosis depends, among other factors, on the thickness of the oil-phase. It can be compared to the diffusion rate by Fick's law, given the diffusion coefficient by the Stokes-Einstein (SE) equation. SE assumes that water diffusion is inversely proportional to the oil-phase viscosity. However, when water moves through an oil-phase without hydrogen bonding the smaller water molecules diffuse faster than predicted [18], and additional considerations are required to describe the waterflux.

The pore-scale osmotic effect observed in capillary tubes is relevant during spontaneous imbibition, where oil production is determined by capillary forces without viscous flow. It is believed that the osmotic effect may contribute favorably during core-scale spontaneous imbibition of low salinity water by expanding volumes of high-saline brine and mobilizing oil out of the core.

Verification of water diffusion in micromodels

Water diffusion was observed as the main transport mechanism at strongly water-wet conditions by the connectivity between fracture bulk-flow and matrix brine. The transport is induced by the chemical potential gradient between the high- and low-saline phases. The potential is defined as the sum of Gibbs free energy for all components in the solution. When salts are mixed with water to form high-saline brine the components spontaneously dissolve into electrically charged ions due to the resulting increase in entropy [11] (*cf.* Table 1). Heat is released during the dissolution process and the Gibbs free energy of the solution, *e.g.* the energy available to do work, is reduced. Low salinity water (DIW in this work) has a higher chemical potential than high-saline brine, and water will move from regions of high to low potential as observed in **Figure 2**. The system is stabilized when Gibbs free energy reaches a minimum for the system as a whole. Hence, water will diffuse to re-establish thermodynamic stability.

Oil mobilization by water diffusion

It was mainly the diffusion of solvents (*i.e.* water) that diluted the high-saline brine in matrix to equilibrate the difference in chemical potential. Ion-dipole forces between salt ions and water molecules reduce the diffusion of solutes as they are stronger than the induced hydrogen bonds between water molecules [19]. Water diffusion was initially identified as a dilution mechanism causing film-expansion and droplet growth during LSW [13]. It was reasoned that the accumulation of water in local water-films increased the water pressure leading to viscous oil displacement into nearby flow channels. Research by Stoll *et al*. [20] emphasized that in absence of significant viscous and capillary forces, wettability modifiers must initially diffuse under its own concentration

gradient into the matrix to activate its chemical process. The results in **Figure 2** support these findings and illustrate how propagation of water may re-distribute the fluids in matrix, displacing oil from pore-to-pore and towards the fracture.

Verification of osmotic water transport in micromodels

Oil mobilization was observed at both strongly water-wet and oil-wet conditions, with water transport to otherwise inaccessible regions of high-saline brine and water-in-oil emulsions (**Figure 3** and **4**). Osmosis is the transport of water when high- and low-saline brines are separated by a semi-permeable membrane that is permeable to pure water, but impermeable to ions [11]. To balance the chemical potential gradient, *e.g.* osmotic gradient, the solvent must have equal values in the two brines by having the two brines at different pressures [14]. Hence, water is transported from the low-saline brine through the membrane to compensate for the reduction in chemical potential of the high-saline brine. The osmotic pressure within the high-saline brine increase with addition of water molecules, and transport stops when the osmotic pressure balances the flow induced by the osmotic gradient.

Semi-permeable membrane characteristics of oil

The semi-permeable properties of oil depend on the intermolecular forces acting between the solute, solvent and hydrocarbon compounds present. The capacity for oils to bind with hydrogen depends on the hydrocarbon composition. Mineral oils with chains of alkanes have zero dipole moment and hence no capacity to hydrogen bond [18]. Asphaltenes and some aromatics present in most crude oils have structures to create weak hydrogen couplings that influence the flux of water [21, 22]. Hence, an oil-phase with a higher fraction of non-polar alkanes should have better membrane properties and act as a more efficient conduit for water molecules under the influence of osmotic gradients.

Wettability effects on osmotic oil mobilization

At strongly water-wet conditions, isolated high-saline brine existed only as water-in-oil emulsions that expand during LSW by aggregating inside the phase. Researchers have drawn special attention to the growth of water-in-oil emulsions: some explain it as a result of surface-active components arranging micelles transporting water molecules to inaccessible brine, see *e.g.* [23], whereas others have suggested that the water transport is caused by osmosis [15-13]. In addition, it has been shown that water-in-oil emulsions can grow without the presence of surface-active components by using mineral oil during LSW [15]. It is therefore suggested that the growth of water-in-oil emulsions is a result of osmosis, supported by results from the present (**Figure 3** and **4**) and previous work [13].

Water-in-oil emulsions are present in this work independent on wettability. The stability of water-in-oil emulsions depend on the composition of the oil-phase. Oil B, *i.e.* crude oil, contains asphaltenes that help stabilize emulsions [24]. Mineral oils containing non-polar alkanes, as used in the oil-wet system, are not interfacially active and cannot form stabilized films around the water-droplets at the oil/water interface [24]. As long as there are compounds present that can form stable films, emulsions should develop.

An oil-wet system represents the most ideal for osmosis as it holds a number of suitable membranes and confined volumes of high-saline brine for oil mobilization (**Figure 4**). Several isolated regions of high-saline brine started to expand and the fluids within matrix were redistributed as observed in images 1-2. As a result oil was mobilized into the nearby flow-channel (**Figure 4**, image 3).

The calculations of osmotic pressure in Table 1 indicate a high potential for viscous pressure build-up during LSW. These theoretical values are unlikely to develop within the pore-space due to the imperfect membrane properties of the oil. In corefloods the reported pressure response is usually transient or modest at best when injecting low salinity water [1, 7, 10, 25]. If osmosis is a significant contributor to the overall trend one would observe a general increase in pressure followed by a slow decrease as the gradient is gradually balanced, see *e.g.* [25]. However, a relationship cannot be drawn between the pressure gradients reported in literature and osmosis.

Osmosis as low salinity effect on reservoir scale

LSE is more relevant at oil-wet conditions as the general understanding is that LSW shifts wettability towards more water-wet increasing oil recovery. However, it has been documented that LSE improves oil recovery without the necessary conditions, see *e.g.* [1, 25]. The variety of circumstances under which LSE may or may not be observed suggests that more than one mechanism may be in play [1]. In the present work, osmosis is observed independent on oil/brine/rock interactions and should therefore be applicable to both oil and water-wet systems.

In a highly flooded water or mixed-wet reservoir it is suggested that enclosed volumes and emulsions of connate water will swell in response to osmosis. Re-mobilization of oil will occur at pore-level until the oil-films either ruptures or thermodynamic stability is re-established. However, it is not likely that the effect will greatly reflect on total recovery. A fractured, oil-wet reservoir (*i.e.* **Figure 4**) would be an ideal system for osmosis to have a significant impact on oil recovery. In a fractured system osmosis will act as a driving force for water transport into the oil-wet matrix. Osmosis may contribute positively to open pathways that increase the water relative permeability, aiding other effective low salinity mechanisms to take place, such as wettability alteration in otherwise inaccessible regions of the matrix, and for oil to be produced into high permeable flood zones.

As osmosis occur independent on wettability is likely to be present in both sandstone (water-wet) and carbonate (oil-wet) formations. To properly determine what effect osmosis will have on recovery, one could use model systems where wettability alteration is excluded. This could help to better quantify the extent of osmosis during LSW. The present work identifies osmosis as a pore-level LSE that improves microscopic sweep in combination with other low salinity mechanisms.

CONCLUSIONS

- Oil-wet capillary tube tests verified osmotic water transport as oil-bulk diffusion from a solution of low salinity to a solution of high salinity due to the semi-permeable characteristics of oil.
- The work performed substantiate osmosis as an underlying low salinity effect for oil mobilization at pore-level by identifying osmotic water transport at both strongly water-wet and oil-wet conditions during low salinity waterflooding.
- Osmotic water transport mobilized oil by either swelling water-in-oil emulsions or expanding otherwise inaccessible regions of capillary trapped high-saline brine.
- At strongly water-wet conditions and capillary equilibrium water diffusion by film-flow was the main transport mechanism for oil mobilization.
- The osmotic effect is influenced by fluid distribution of oil and water. It is independent of system wettability and should therefore be present as a pore-scale oil mobilization mechanism in both sandstones (*e.g.* water-wet) and carbonates (*e.g.* oil-wet) during LSW.

ACKNOWLEDGEMENTS

The authors would like to thank the Norwegian Research Council for financial support.

REFERENCES

[1]. Morrow, N. and Buckley, J. "Improved Oil Recovery by Low-Salinity Waterflooding," *Journal of Petroleum Technology*, (2011) **63**, 05, 106-112.
[2]. Tang, G. and Morrow, N. "Salinity, Temperature, Oil Composition, and Oil Recovery by Waterflooding," *SPE Reservoir Engineering*, (1997) **12**, 04, p. 269-276.
[3]. Lightelm, D., Gronsveld, J., Hofman, J., Brussee, N., Marcelis, F. and van der Linde, H. "Novel Waterflooding Strategy by Manipulation of Injection Brine Composition," *Society of Petroleum Engineers*, (2009).
[4]. Sheng, J. "Critical review of low-salinity waterflooding," *Journal of Petroleum Science and Engineering*, (2014) **120**, p. 216-224.
[5]. Lager, A., Webb, K., Black, C., Singleton, M. and Sorbie, K. "Low Salinity Oil Recovery – An Experimental Investigation[1]," *Society of Petrophysicists and Well-Log Analysis*, (2008) **49**, 01, p. 28-35.
[6]. Romanuka, J., Hofman, J., Ligthelm, D., Suijkerbuijk, B., Marcelis, A., Oedai, S., Brussee, N., van der Linde, H., Aksulu, H. and Austad, T. "Low Salinity EOR in Carbonates," *Society of Petroleum Engineers* (2012).
[7]. Yousef, A., Al-Saleh, S., Al-Kaabi, A. and Al-Jawfi, M. "Laboratory Investigation of the Impact of Injection-Water Salinity and Ionic Content on Oil Recovery From Carbonate Reservoirs," *SPE Reservoir Evaluation & Engineering*, (2011) **14**, 05, p. 578-593.
[8]. Chilingar, G. and Yen, T. "Some Notes on Wettability and Relative Permeabilities of Carbonate Reservoir Rocks, II," *Energy Sources* (1983) **7**, 01, p. 67-75.
[9]. Suijkerbuijk, B., Hofman, J., Ligthelm, D., Romanuka, J., Brussee, N., van der Linde, H. and Marcelis, A. "Fundamental investigations into wettability and low salinity flooding by parameter isolation," *Society of Petroleum Engineers* (2012).
[10]. Sandengen, K. and Arntzen, O. "Osmosis During Low Salinity Water Flooding," *EAGE 17th European Symposium on Improved Oil Recovery* (2013).

[11]. Allen, J. *Biophysical Chemistry*, Wiley-Blackwell, Singapore (2009) p. 47-51, 54-56, 73, 94-95, 120-123.
[12]. Sandengen, K., Kristoffersen, A. and Melhuus, K. "Osmosis as Mechanism for Low-Salinity Enhanced Oil Recovery," *SPE Journal*, (2016) p.1-9.
[13]. Fredriksen, S., Rognmo, A. and Fernø, M. "Pore-Scale Mechanisms during Low Salinity Waterflooding: Water Diffusion and Osmosis for Oil Mobilization," *Society of Petroleum Engineers*, (2016).
[14]. Mortimer, R. *Physical Chemistry*, Academic Press, United States of America (2000), p. 168-170, p. 248-249.
[15]. The National Institute of Standards and Technology (NIST). "*NIST Standard Reference Database 69; NIST Chemistry WebBook*," U.S. Secretary of Commerce, United States of America (2016).
[16]. Moeini, F., Hemmati-Sarapardeh, A., Ghazanfari, M., Masihi, M. and Ayatollahi, S. "Toward mechanistic understanding of heavy crude oil/brine interfacial tension: The roles of salinity, temperature and pressure," *Fluid Phase Equilibira* (2014) **375**, 01, p. 191-200.
[17]. Cath, T., Childress, A. and Elimelech, M. "Forward osmosis: Principles, applications, and recent developments," *Journal of Membrane Science* (2006) **281**, 1-2, p. 70-87.
[18]. Su, J., Duncan, B., Mornaya, A., Jutila, A. and Needham, D. "The effect of hydrogen bonding on the diffusion of water in *n*-alkanes and *n*-alcohols measured with a novel single microdroplet method," *The Journal of Chemical Physics*, (2010) **132**, 04, p. 0445061-8.
[19]. Person, E., Golden, D. and Royce, B. "Salting Effects as an Illustration of the Relative Strength of Intermolecular Forces," *Journal of Chemical Education* (2010) **87**, 12, p. 1332-1335.
[20]. Stoll, W., Hofman, J., Ligthelm, D., Faber, M. and van den Hoek, P. "Toward Field-Scale Wettability Modification – The Limitations of Diffusive Transport," *SPE Reservoir Evaluation & Engineering* (2008) **11**, 03 p. 633-640.
[21]. Spiecker, P., Gawrys, K. and Kilpatrick, P. "Aggregation and solubility behavior of asphaltenes and their subfractions," *Journal of Colloid and Interface Science* (2003) **267**, 01, p. 178-193.
[22]. Levitt, M. and Perutz, M. "Aromatic Rings Act as Hydrogen Bond Acceptors," *Journal of Molecular Biology* (1988) **201**, 04, p. 751-754.
[23]. Emadi, A. and Sohrabi, M. "Visual Investigation of Oil Recovery by Low Salinity Water Injection: Formation of Water Micro-Dispersions and Wettability Alteration," *Society of Petroleum Engineers* (2013).
[24]. Kokal, S. "Crude-Oil Emulsions: A State-Of-The-Art Review," *SPE Production and Facilities* (2005) **20**, 01, p. 5-13.
[25]. Cissokho, M., Boussour, S., Cordier, P., Bertin, H. and Hamon, G. "Low Salinity Oil Recovery on Clayey Sandstone: Experimental Study," *Society of Core Analysists* (2009).

Micro-CT study of the Impact of Low Salinity Waterflooding on the pore-scale fluid distribution during flow

W.-B. Bartels[1, 2], M. Rücker[1, 3], S. Berg[1], H. Mahani[1], A. Georgiadis[1, 8], N. Brussee[1], A. Coorn[1], H. van der Linde[1], A. Fadili[1], C. Hinz[4], A. Jacob[4], C. Wagner[5], S. Henkel[6], F. Enzmann[4], A. Bonnin[7], M. Stampanoni[7], H. Ott[3, 9], M. Blunt[3], S.M. Hassanizadeh[2]

[1] Shell Global Solutions International B.V., Kesslerpark 1, 2288 GS Rijswijk, The Netherlands
[2]Earth Sciences department, Utrecht University, 3584 CD Utrecht, The Netherlands
[3] Department of Earth Science and Engineering, Imperial College London, SW7 2AZ UK
[4] Geosciences Institute, Johannes Gutenberg-University, Becherweg 21, 55099 Mainz, Germany
[5] Math2Market GmbH, Stiftsplatz 5, 67655 Kaiserslautern, Germany
[6] Institute of Geosciences, Friedrich Schiller University Jena, Burgweg 11, 07743 Jena, Germany
[7] Swiss Light Source, Paul Scherrer Institute, CH-5232 Villigen, Switzerland
[8] Department of Chemical Engineering, Imperial College London, SW7 2AZ UK
[9] Department of Petroleum Engineering, Montanuniversität Leoben, A-8700 Leoben, Austria

This paper was prepared for presentation at the International Symposium of the Society of Core Analysts held in Snowmass, Colorado, USA, 21-26 August 2016.

ABSTRACT

Many studies indicate that the recovery of crude oil by waterflooding can be improved in both sandstone and carbonate rocks by lowering the salinity of injected water. This so-called low salinity effect is thought to be associated with the change of the wetting state of rock towards more water wet. However, it is not very well understood how wettability alteration on the pore level could lead to an increase in production at the Darcy scale. Therefore, this study aims at direct pore scale observation of the wettability-change-driven fluid reconfiguration related to a low salinity (LS) flood at the length scale between a single pore and the Darcy scale (i.e. pore network scale). We investigate the low salinity effect in real time and in 3D using synchrotron beamline-based fast X-ray computed tomography during flow experiments.

Cylindrical outcrop rock samples of 20 mm length and 4 mm diameter were initialized by first saturating them with high salinity (HS) brine and then with crude oil. Subsequently, they were aged at 30 bars and 70°C for one week in order to establish wettability states assumed close to reservoir conditions. The synchrotron beamline-based fast tomography allowed us to image the pore scale fluid distribution at a spatial resolution of 3 μm and (under flowing conditions) at time intervals of 10 s for a full 3D image.

The micro-CT flow experiments were conducted on both sandstone and carbonate rocks, all in tertiary mode, i.e. by first performing a HS water flood i.e. forced imbibition (as base-line) followed by a LS waterflood, both at identical field relevant flow rates. The real-time imaging shows a saturation change during the HS waterflood which approaches a stable equilibrium at its end. When switching to low salinity water, we observe a

change in average saturation and pore scale distribution of both fluids, which is distinctly different from the stabilizing saturation during HS flooding. Compared to the end of the HS flood, during the LS flood in both sandstone and carbonate rock, the oil moves from pore throats to the center of pore bodies. This movement is indicative of a pore scale wettability transition from a mixed wet to a more water wet state. This process involves (re)connection and disconnection of the oil phase as it moves through narrow pore throats which is characteristic of ganglion dynamics.

INTRODUCTION

Low salinity waterflooding (LSF) is an enhanced oil recovery/improved oil recovery (EOR/IOR) technique which mobilizes more oil by modifying and/or lowering the ionic composition of the injected brine. For sandstones, the range at which additional production occurs lies between 1500 and 5000 ppm. Lower salinities may lead to formation damage due to fines migration and plugging. For carbonates, the LS threshold at which the low salinity effect (LSE) occurs lies much higher. There are even cases reported for sea water; see [1] and references therein for a short overview. In addition, the exact brine chemistry is deemed more important for carbonates than for sandstones. The LSE is often described phenomenologically by wettability alteration to a more water-wet state. However, the mechanisms behind the alteration are not fully understood.

Several mechanisms have been proposed in the literature; however, there is no general consensus on the dominant mechanism or mechanisms; see e.g. [2-5]. Moreover, the evidence supporting a particular mechanism is often indirect or inferred from the experimental measurements; and in some cases the evidence is even contradictory. If we examine the body of literature, in general it can be divided into two groups. On the one hand there are studies looking at contact angle changes and detachment of crude oil from mineral surfaces i.e. at sub pore scale. On the other hand there are experiments which look for incremental production of crude oil in core flooding experiments. However, it is not clear how a contact angle change on the sub pore scale leads to additional Darcy scale oil production. There is a gap between the (sub) pore scale and the Darcy scale in which hardly any research has been conducted. Incremental oil production on the Darcy scale requires a change in configuration of oil on the scale of multiple pores, i.e. the pore network scale. The details of this change of oil saturation distribution on the pore network scale is expected to close the gap between surface science and reservoir engineering concepts and provide the links between proposed mechanisms and Darcy scale observation.

In order to investigate the effect of LSF on the configuration of oil on this intermediate pore network scale under flowing conditions, we use synchrotron based fast X-ray tomography.

MATERIALS AND METHODS

Rock samples and brines

For the experiments in this study, we used Berea sandstone [6] combined with reservoir dead crude “S” (density $\rho = 0.87$ g/cm^3, viscosity $\eta = 7.87$ mPa·s, at T = 20°C) and

Ketton as carbonate rock with reservoir dead crude "C" (ρ = 0.83 g/cm3, η = 4.30 mPa·s, at T = 20°C). The samples were 20 mm long and 4 mm in diameter and embedded in heat-shrunken PEEK (Polyether Ether Ketone) tubes. As HS brine, we used 200 g/L KI (potassium iodide, ionic strength 0.602 mol/L) and as LS water, 27 g/L KI (ionic strength 0.081 mol/L).

Experimental workflow

A rock sample was first cleaned using isopropanol and then shrunken in PEEK. When handling the core, nitrile gloves were used at all times to prevent altering the wettability of the rock upon touch. The sample was then fully saturated with HS brine under vacuum. Subsequently, it was mounted on the flow cell as used in [7, 8] to establish initial water and oil saturation in the sample. When the sample was saturated with HS brine and crude oil, the initial wettability state was established by aging it submerged in crude oil at 30 bars and 70°C for one week. The experimental set-up we used has been described in [7, 8], where the two cylinders of the in-situ pump were used for fractional flow experiments. In this study, the cylinders were filled with HS brine and LS water, respectively, to conduct tertiary LS flooding experiments.

The flooding and X-ray saturation monitoring experiments were performed at the TOMCAT beamline of the Swiss Light Source (Paul Scherrer Institute) which is a fast synchrotron-based X-ray computed micro-tomography facility. In this study, a "pink beam" configuration with a finite X-ray energy spectrum was used. This setting caused significant beam hardening. The flow rate in both high and low salinity experiments was 30 µl/min (equivalent to ~12 ft/day) and injection always occurred from bottom to top. The field of view (FOV) was chosen 2 mm above the inlet, and dimensions of the monitored area were approximately 4 mm laterally and 3 mm along the principal axis of the sample. A full 3D image with a voxel size of 3 µm was obtained within about 7 s. The transition from HS flooding to LS flooding was monitored continuously for 5 min. In addition, images from 30 minutes before to 30 minutes after the transition were recorded at a rate of 1 image/min.

Image processing

The images were reconstructed using the Paganin method [9, 10] since the end result was found superior to that of the attenuation contrast reconstruction method, as shown in **Figure 1**.The reconstructed micro-CT images were filtered, segmented, and processed with the software package AVIZO 9.0 and 8.1 (FEI). A combination of gradient images and watershed segmentation led to satisfactory results. After segmentation, the binarized images are analyzed further.

RESULTS AND DISCUSSION

Potential Imaging Artifacts

The processed grey scale images before segmentation, such as the one for the oolitic carbonate rock shown in **Figure 2**, show a clear contrast difference between grains, the doped brine (at HS), and a dark phase which should contain the oil. However, a more

detailed inspection reveals a grey- scale variation and a structure inside the darkest phase, see
Figure 3, which occurs systematically for all samples studied. That raises the suspicion that a third fluid phase may be present and brings up several questions about

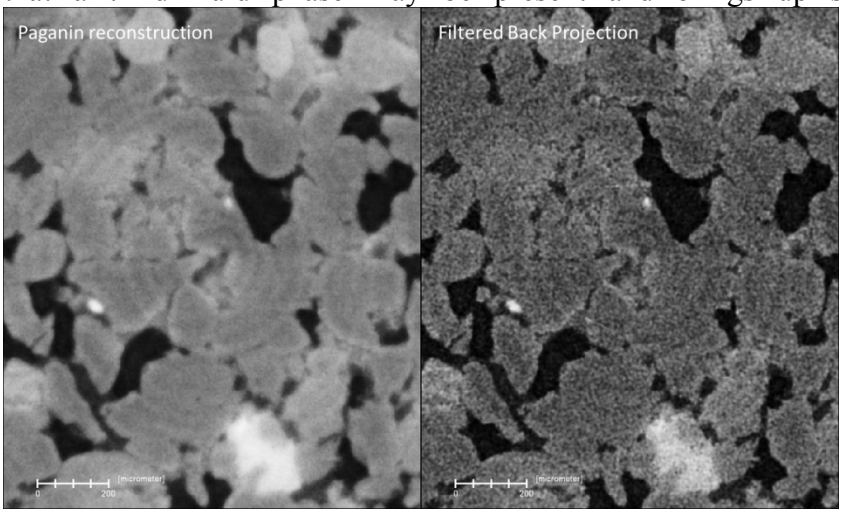

Figure 1: Difference in image quality by reconstructing Berea sandstone with Paganin (left) and Filtered Back Projection (right) algorithms. There is a clear difference in noise level and contrast between the two methods. The scale bar indicates 200 micrometer.

significance and interpretation of the images and the origin of the phases that are visible. This is discussed in the following sections.
Possible explanations for the apparent presence of three phases are:
A) artefacts related to reconstruction, filtering and beam hardening,
B) trapping of gas during sample preparation,
C) gas formation due to X-ray exposure,
D) degassing of crude oil due to X-ray exposure,
E) discoloration of a part of the brine phase due brine-rock interaction such as ion exchange and adsorption
F) formation of oil/water structures.
Some of these possibilities are more likely than others. The questions that arise are: is this an artifact that invalidates the experiment as such (items B-D) or an artifact that complicates the data analysis (A); are the experiments in principle valid; or are we actually dealing with a relevant phenomenon (E-F).
Note that we have observed these effects in all our synchrotron beamline LSF experiments in both sandstone and carbonate samples. Explanations B, C and D relate to the origin of the darkest phase, suggesting that the intermediate phase is oil and the bright phase is HS brine. Explanations D and E assume that the intermediate phase is the anomalous phase i.e. something other than oil or brine. Below, we provide a detailed assessment of each explanation.

A) Artefacts related to reconstruction, filtering and beam hardening

Our data shows significant beam hardening. To what extent this effect translates into gray scale variations and structures within pores is not clear. In addition, glow from the HS brine phase and from the grains may elevate the gray levels of the darkest phase in the pore space. Still, the darkest phase seems to be much brighter than the exterior, indicating that it cannot be a gas phase.

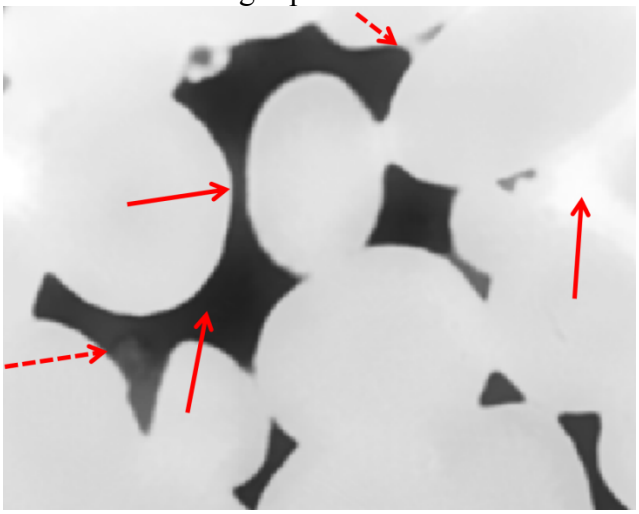

Figure 2: Different gray values in the pore space of oolitic carbonate rock. We distinguish between bright, intermediate and dark phases. In some cases, interfaces are visible, see dashed arrows.

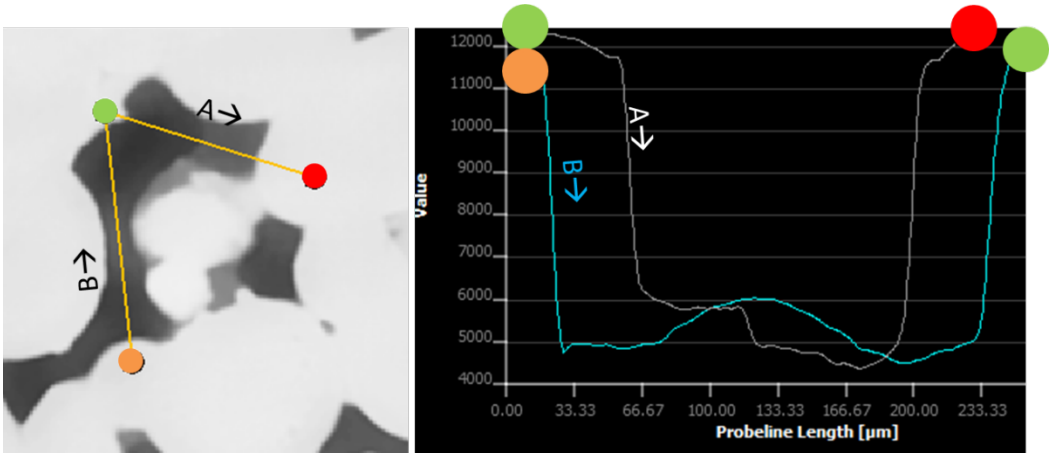

Figure 3: Stepped change in gray value and gradual changes in gray value overlap making segmentation difficult. This example was taken from carbonate rock.

B) Trapping of gas during sample preparation

After the preparation of the samples at Shell laboratories, micro-CT scans with a benchtop instrument (ZEISS Xradia 520 Versa) were made. Benchtop machines use a much broader and higher energy X-ray spectrum but at several orders of magnitude lower intensity. In those scans, no such variation in the darkest phase was observed; at least, the formation of a separate gas phase could be ruled out. After preparation of the samples, in-house micro-CT scans only revealed two sets of gray levels: that of HS brine (bright) and oil. In cases that air and/or gas had been accidentally trapped in the pore space, this was

clearly recognizable in the in-house scans and these samples had been excluded from further analysis. However, imaging at the synchrotron beamline – approximately after one week of aging –revealed the situation shown in **Figure 2** in all samples. So, unless a gas phase forms (C, D) upon exposure to the much higher intensity synchrotron beam, explanation (B) can be ruled out.

C) Gas formation due to X-ray exposure

In previous beamline experiments, the formation of bubbles has been observed, but it was also found that occurrence and magnitude of the effect depended on beam energy, intensity, type of fluid, and dopant concentration. While the reason was ultimately not clear, a photochemical effect was discussed as the most likely cause. In order to assess whether the darkest phase in **Figure 2** could be in-situ formed gas bubbles, we conducted a long-time exposure experiment to see if the specific beam settings used in this study would lead to bubble formation as well. Similarly to previous studies, we observed bubble formation in the (doped) brine phase, as shown in **Figure 4**, but no formation of gas bubbles in the oil phase were observed. Morphology and growth kinetics of the bubbles are very different from the structure in the darkest phase in **Figure 2**. In addition, if the bubbles have a photochemical origin, one would expect the process to occur or intensify when freshly doped HS brine was injected in the system. Examining saturation of the dark, intermediate and bright phase versus time displayed in **Figure 7** does not show such an increase. Therefore, (C) is also very unlikely.

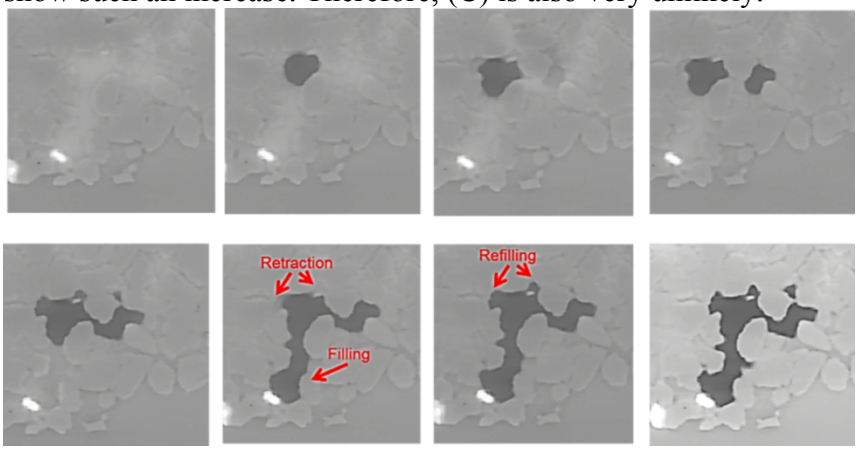

Figure 4: Bubble formation in sandstone only filled with strongly doped HS brine. There was no flow during this experiment. The images are taken with intervals of 10 seconds.

D) Degassing of crude oil

When the temperature is increased or the pressure is decreased, light hydrocarbon components present in the crude oil may come out of solution and form gas bubbles. However, the temperature during transport and experimentation did not increase by more than 2 °C. In addition, the pressure was constant. Given that both crude oils were "dead crude" (i.e. degassed crude) with the bubble point being far away from conditions in the experiment, (D) is very unlikely.

E) Discoloration of part of the brine phase

Some of the intermediate grey levels could represent brine with a reduced concentration of contrast agent KI. One might speculate that such a compositional change might have occurred through brine-rock interactions, such as ion exchange reactions with the solid, or adsorption. However, the laws of thermodynamics would prohibit any spontaneous de-mixing. Another counter-argument is that when the intermediate grey level is classified as a brine phase, it implies very low initial oil saturation. In addition, if the intermediate grey levels are interpreted as a separate phase, then the observation of a "contact angle" with the brine phase would rule out an aqueous phase even though the phase is mostly located in the corners of pores.

F) Formation of oil/water structures

Oil-brine mixing tests revealed that the crude oils used in this study can form oil/water structures, such as emulsions, when in contact with brine. This is shown in **Figure 5**.

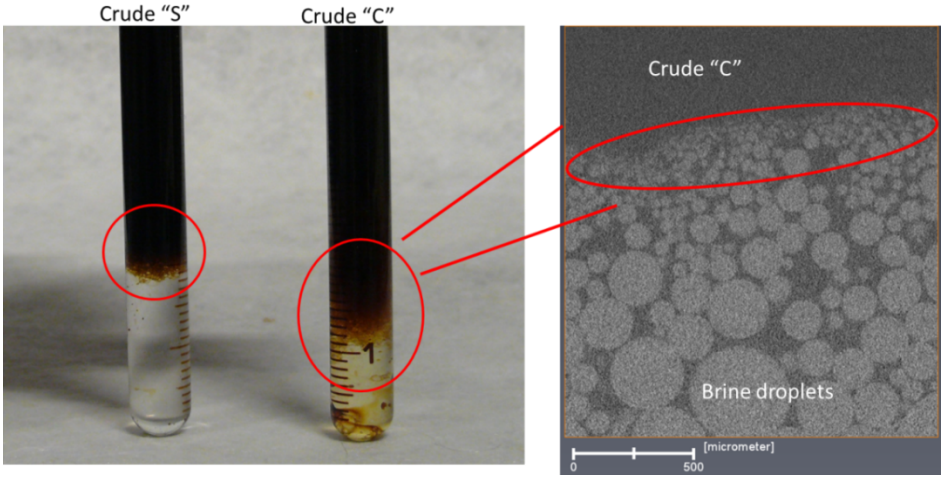

Figure 5: Different degrees of oil/water structure formation for crude "S" and "C". The right hand side shows a benchtop micro-CT scan of the interface between crude "C" and emulsion. The encircled portion of this image shows droplets below the imaging resolution.

Such structures have also been described by others [11-13]. The gray values of these oil/water structures would lay in between that of the pure phases. Any micro-structure i.e. individual droplets may be significantly blurred given the limited spatial resolution of the micro-CT and imaging artifacts discussed in (A).

In summary, the development or presence of a gas phase (explanations B-D) and the presence of a second brine phase (E) seem unlikely. Certainly, imaging and reconstruction artifacts occur (A) and if these are solely responsible for the variation of grey levels, all should be lumped into the oil phase. But the formation of oil/water structures (F) could occur as observed in tube tests under similar conditions (see **Figure 5**). Because of the potential connection of gray-scale feature to a LSE [12, 13] it might therefore be beneficial to treat it until further clarification as a separate phase.
In the following we will discuss the response to LS and focus in particular on the aspects that are robust against the considerations A-F. Therefore we will focus on the behavior of the darkest phase.

Response to High Salinity

During HS flooding, we see the oil phase clusters disconnecting and reconnecting, which indicates a ganglion dynamics flow regime as observed already in 2D micro-models [14] and other micro-CT imbibition experiments [8], [15], [16]. However, we see oil-filling events covering pore bodies in the mixed-wet condition as shown in **Figure 6**. We did not observe this in previous studies under water-wet conditions.

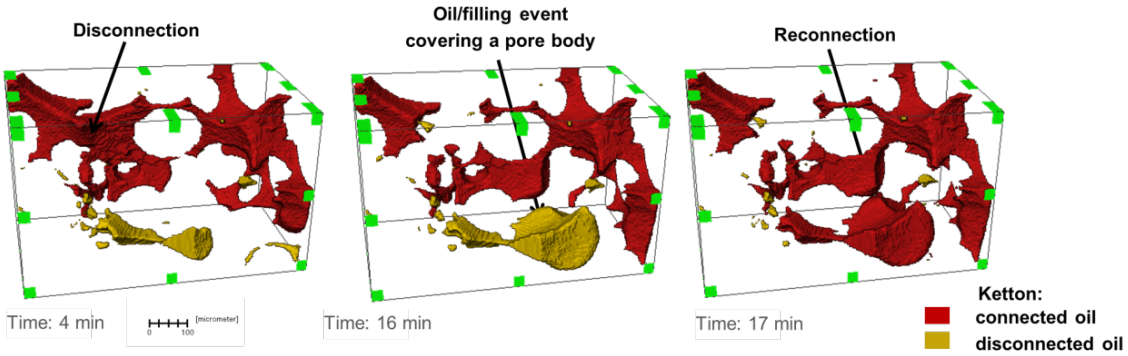

Figure 6: 3D rendering of pore filling event in carbonate (Ketton) rock in HS.

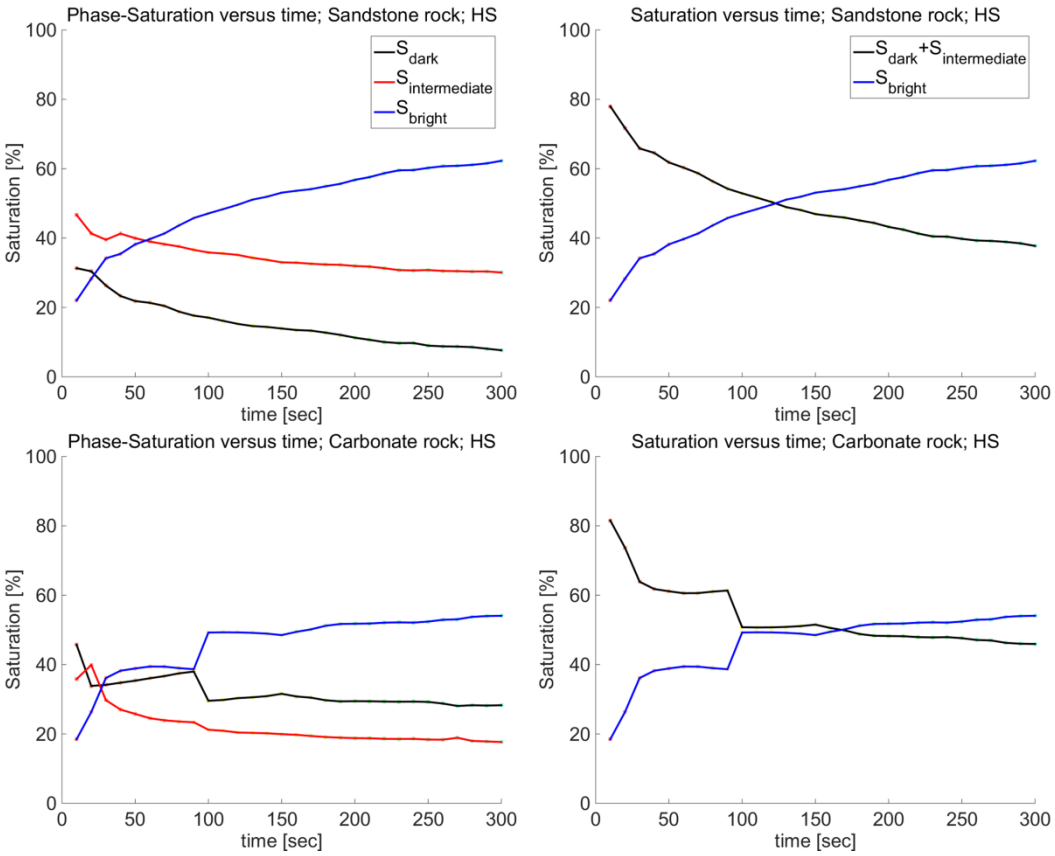

Figure 7: Saturation versus time plots for a HS flood in sandstone and carbonate. The decrease of the darkest phase suggests that it cannot be gas that is created because of X-ray exposure. The initial

saturations suggest that the intermediate gray phase and the dark phase should be considered as the same phase.

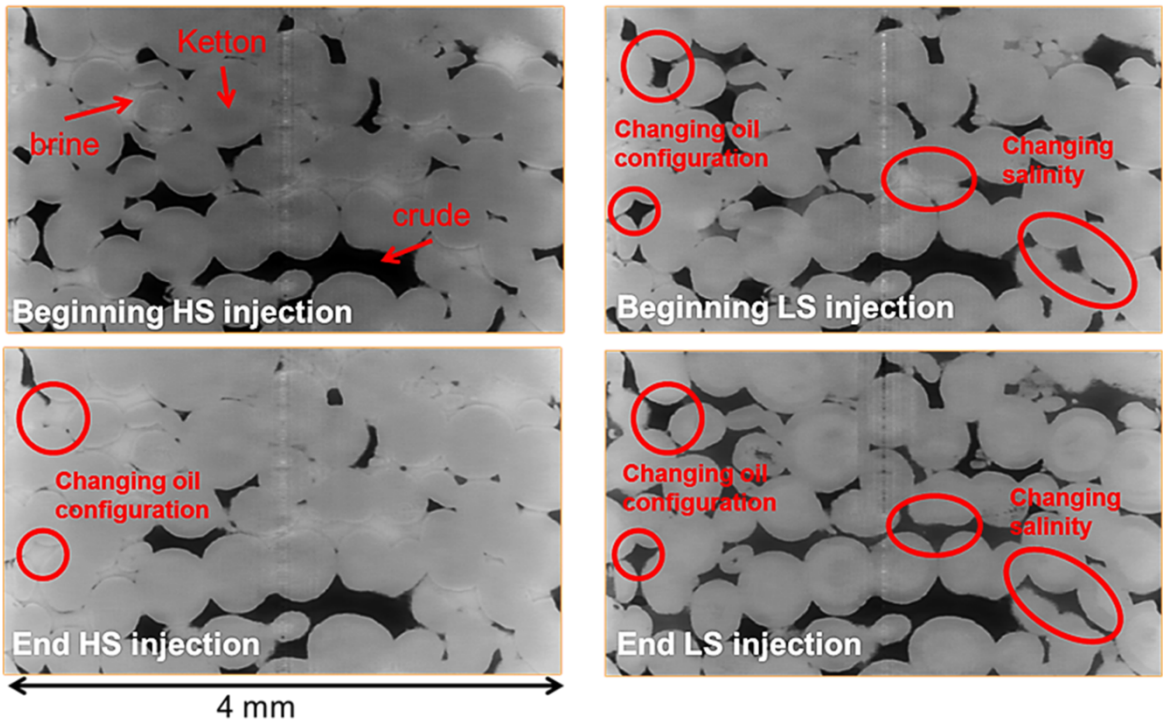

Figure 8: When changing from HS to LS, a clear redistribution of oil can be seen from the pore throats to the pore bodies. This is seen most clearly in Ketton rock (Carbonate).

Response to Low Salinity

The first observation in the images captured during LS is that we can track the change in salinity as the concentration of contrast agent decreases as seen in **Figure 8**. Secondly, we see a change in oil configuration as the oil phase moves from smaller to larger pores at the transition from HS to LS, also shown in **Figure 8**. This is indicative of a wettability alteration towards more water wet, as is expected in a successful LSF experiment. For sandstone, this is intriguing since the salinity level used here is much higher than the generally accepted salinity range of 1500-5000 ppm in which the macroscopic (Darcy) LSE has been typically observed.

Pore filling events

We also observe ganglion dynamics during the LS flood. During LS flooding, we clearly see that the extent of oil displacement is much larger than at the final stages of the HS flood, as illustrated in **Figure 9**. This indicates that the LS water did mobilize more oil, which may have come from the upstream part of the sample outside the FOV. This oil saturation increase in the FOV can be temporary (a transient effect) and could be related to oil banking by LS. The oil bank could eventually be produced from the sample.

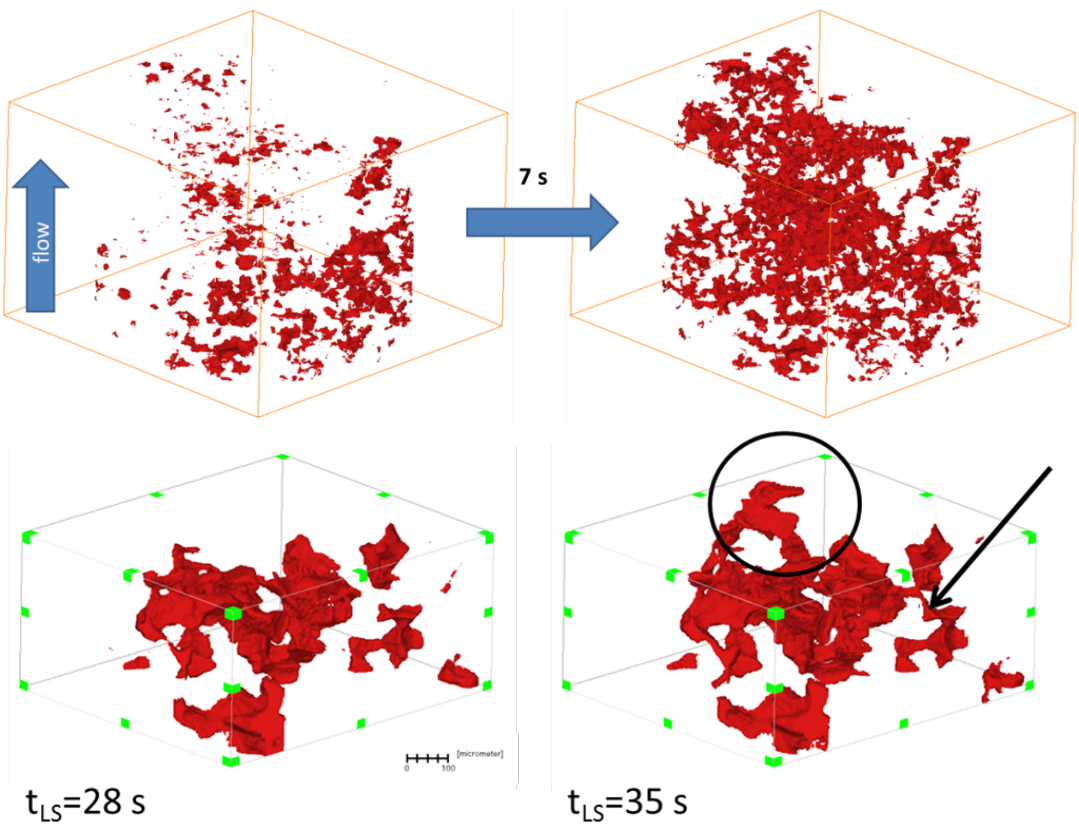

Figure 9: Top: Increase in the darkest phase in 7 seconds in Berea sandstone during LS flooding. This magnitude of increase cannot be caused by gas. In addition, this increase is occurring after the saturation of all phases stabilized during HS flooding, see **Figure 7**. Bottom: Cluster dynamics during LS flow in Berea sandstone. Scale bar indicates 100 micrometer. The circle indicates growth of the oil cluster and the arrow indicates a (re)connection point. Flow is from bottom to top.

CONCLUSIONS

We have observed an additional oil/water structure or a third phase and are not sure of its nature and origin. Further tests need to be conducted to verify whether this oil/water structure is a (micro-) emulsion. Regardless of the occurrence of this structure, we still can draw the following conclusions regarding the LSF experiments.

- We reached a stable saturation during HS flooding.
- During LS injection, we observed the following:

i) There is oil redistribution from pore throats to pore bodies, which would correspond to a shift of wettability to a more water wet system.

ii) There is an increase in the overall oil saturation in the investigated FOV. This is most likely the mobilized or re-connected oil from upstream and is indicative of a low-salinity effect. The increase of oil saturation can be transient and may be

related to oil banking by LS. The oil bank, because of high saturation and high relative permeability, may eventually be produced from the sample.

Additionally:

- For sandstones, the LSE occurred at relatively high salinities.
- We observed filling events covering multiple pores in both rock types, which we believe to be specific to the mixed wet state of the system.
- We see ganglion dynamics in both HS and LS regimes but in LS we also see remobilization of crude oil.

ACKNOWLEDGEMENTS

We would like to acknowledge the staff of the TOMCAT beamline at the Swiss Light Source of the Paul Scherrer Institute, Villigen, Switzerland for support during the execution of this work. We thank Alex Schwing and Rob Neiteler for the design of the flow set-up and instrumentation, Fons Marcelis for sample preparation, Kamaljit Singh for supplying the Ketton rock and Axel Makurat for helpful discussions and leadership support. We gratefully acknowledge Shell Global Solutions International B.V. for permission to publish this work.

REFERENCES

1. Mahani, H., A. Keya, S. Berg, W.-B. Bartels, R. Nasralla and W. Rossen, “Insights into the Mechanism of Wettability Alteration by Low-Salinity Flooding (LSF) in Carbonates”, *Energy and Fuels* (2015), **29**, 1352-1367.
2. Aladasani, A., B. Bai, Y.-S. Wu and S. Salehi, “Studying low-salinity waterflooding recovery effects in sandstone reservoirs”, *Journal of Petroleum Science and Engineering* (2014), **120**, 39-51.
3. Morrow, N., and J. Buckley, “Improved Oil Recovery by Low-Salinity Waterflooding”, *Journal of Petroleum Technology*, SPE-129421 (2011).
4. Myint, P., and A. Firoozabadi, "Thin liquid films in improved oil recovery from low-salinity brine." *Current Opinion in Colloid & Interface Science* (2015) **20**, 2, 105-114.
5. Lager, A., K. Webb, C. Black, M. Singleton and K. Sorbie, “Low Salinity Oil Recovery – An Experimental Investigation”, *Petrophysics* (2008), **49**, 1, 28-35.
6. Berg, S., H. Ott, S.A. Klapp, A. Schwing, R. Neiteler, N. Brussee, A. Makurat, L. Leu, F. Enzmann, J.O. Schwarz, M. Kersten, S. Irvine and M. Stampanoni, “Real-time 3D imaging of Haines jumps in porous media flow”, *Proceedings of the National Academy of Sciences* (2013), **110**, 10, 3755-3759.
7. Armstrong, R., H. Ott, A. Georgiadis, M. Rücker, A. Schwing and S. Berg, “Subsecond pore-scale displacement processes and relaxation dynamics in multiphase flow”, *Water Resources Research* (2014), **50**, 9162–9176.

8. Rücker, M., S. Berg, R. Armstrong, A. Georgiadis, H. Ott, L. Simon, F. Enzmann, M. Kersten and S. de With, “The fate of oil clusters during fractional flow: trajectories in the saturation-capillary number space”, *SCA2015-007*.
9. Paganin, D., S. Mayo, T. Gureyev, P. Miller and S. Wilkins, "Simultaneous phase and amplitude extraction from a single defocused image of a homogeneous object." Journal of microscopy (2002) **206**, 1, 33-40.
10. Marone, F., and M. Stampanoni, "Regridding reconstruction algorithm for real-time tomographic imaging." Journal of synchrotron radiation (2012), **19**, 1029-1037.
11. Rezaei, N., and A. Firoozabadi, “Macro- and Microscale Waterflooding Performances of Crudes which form w/o Emulsions upon Mixing with Brines”, *Energy & Fuels* (2014), **28**, 2092-2103.
12. Sohrabi, M., P. Mahzari, S. Farzaneh, J. Mills, P. Tsolis, S. Ireland, “Novel Insights into Mechanisms of Oil Recovery by Low Salinity Water Injection”, This paper was prepared for presentation at the SPE Middle East Oil & Gas Show and Conference held in Manama, Bahrain, 8-11 March 2015, *SPE-172778-MS*.
13. Fredriksen, S., A. Rognmo and M. Fernø, “Pore-Scale Mechanisms During Low Salinity Waterflooding: Water Diffusion and Osmosis for Oil Mobilization”, paper prepared for presentation at the SPE Bergen One Day Seminar held in Bergen, Norway, 20 April 2016, *SPE-180060-MS*.
14. Avraam, D. and A. Payatakes, “Flow regimes and relative permeabilities during steady-state two-phase flow in porous media”, *Journal of Fluid Mechanics* (1995), **293**, 207-236.
15. Berg, S., R. Armstrong, A. Georgiadis, H. Ott, A. Schwing, R. Neiteler, N. Brussee, A. Makurat, M. Rücker, L. Leu, M. Wolf, F. Kahn, F. Enzmann and M. Kersten, “Onset of oil mobilization and non-wetting phase cluster size distribution”, *SCA2014-022*, (2014).
16. Youssef, S., E. Rosenberg, H. Deschamps, R. Oughanem, E. Maire, and R. Mokso, “Oil ganglia dynamics in natural porous media during surfactant flooding captured by ultra-fast x-ray microtomograpy”, *SCA2014-023,* (2014).
17. Georgiadis, S. Berg, A. Makurat, G. Maitland and H. Ott, “Pore-Scale micro-CT Imaging: Non-Wetting Phase Cluster Size Distribution During Drainage and Imbibition”, *Physical Review E* (2013), **88**, 3.

EXPERIMENTAL CARACTERISATION OF THE RELATIVE GAS PERMEABILITY OF VERY LOW PERMEABILITY ROCKS

F. Bignonnet[1], P. Egermann[2], Z. Duan[3], L.Jeannin[4], F. Skoczylas[3]
1 : Université de Nantes, GeM équipe IEG, UMR CNRS 6183, France
2 : Storengy (ENGIE group), France
3 : Ecole Centrale de Lille, France
4 : ENGIE E&P International, France

This paper was prepared for presentation at the International Symposium of the Society of Core Analysts held in Snowmass, Colorado, USA, 21-26 August 2016

ABSTRACT

The relative gas permeability (k_{rg}) of a low permeability caprock has been measured on a set of samples. The intrinsic gas permeability of the samples are typically in the order of 10^{-4}-10^{-3} mD in the dry state at in-situ confining stress (9 MPa). Water saturations of the samples are achieved by equilibrating them in chambers whose relative humidities are imposed. The measured k_{rg} points lie on a main curve for all the samples and exhibit a very high critical gas saturation (S_{gc}) around 30% above which gas flow can be detected. The origin of this very specific behaviour is discussed using the percolation theory and an analogy with the k_{rg} curves shape observed during depletion tests. A possible explanation involves flow of gas as a discontinuous phase at gas saturations below S_{gc} during the percolation regime, leading to extremely low k_{rg} values with a plateau shape like in depletion tests.

INTRODUCTION

The characterization of low permeability rocks comprising clay is important in the context of unconventional reservoir production, basin modelling and geological storage (CO_2, natural gas,). Nevertheless the available literature data about their associated relative permeabilities are scarce mainly because of the complexity to derive these data in a representative manner and in a reasonable time frame from laboratory experiments (Lefort *et al.*, 2011). This work is a contribution to provide such a dataset in a tight carbonate with a significant clay fraction.

PROCEDURES

Material

The studied material is a caprock, featuring very fine grained carbonate aggregates and minor clay content. All the samples used in this study have been extracted from a core taken from a caprock layer located at a depth around 450 m. A confining pressure of 9 MPa has been assumed representative of in-situ conditions for this layer.

Geochemical analysis indicates that the carbonate content is high with 276,000 parts per million in weight (ppm) of Ca. Additionally, the rock comprises 7,030 ppm of Mg, 7,980 ppm of K, 11,250 ppm of Fe and 6,130 ppm of S, which indicates silicates and clay content. The total organic carbon is 0.57 % and the pyrite component is minor (1.1 %). The anions have not been measured in the "bulk" geochemical analysis, but local EDX analysis indicates that the carbonate is made of tightly packed aggregates of size 1-10 μm, separated by thin layers or canaliculi. The clay content - most likely illite - is located in these thin layers surrounding the carbonate aggregates as well as in isolated high-porosity pockets of micro-metric extension which exhibit micro-metric porosities.

Methods

Sample preparation: Eight vertical cylindrical samples with diameter 37 mm and height 10 mm have been extracted from the main vertical core. The axis of the cylinders is assumed perpendicular to the bedding. The cylindrical samples are first obtained by 37-mm coring, and then cut to the specified length. The faces of the samples are then polished with sandpaper. The height h and diameter d of each sample are then measured with a calliper with a precision of 0.02 mm. The total volume V of each sample is simply assessed by $V = \pi h d^2/4$.

Water Sorption Isotherms and Water Porosity Measurements

Step 1: Drying. All samples are first oven-dried at 60°C until mass stabilisation is achieved, which occurs after about two weeks. This temperature has been chosen to ensure a fairly good state of drying, while limiting the damage (e.g. micro-cracking), which could arise at higher temperatures. This state is considered as the reference dry state, and the water saturation S_w is assumed null. The mass in the dry state m dry is measured with a precision of 0.01g.

Step 2: Water saturation. To obtain a partial water saturation, the samples are stored in a chamber comprising air and water vapour in equilibrium with a saturated saline solution at 20°C (Chen *et al.*, 2012). The relative humidity of the atmosphere in the chamber is imposed by thermo-dynamical equilibrium and depends on the type of saline solution. The relative humidities imposed in the present study range from 43% to 98%.In turn, the capillary pressure $P_{cap} = P_g - P_l$ between the gas (here at atmospheric pressure) and the liquid water (which condenses in the pore network of the sample) is related to the relative humidity RH of the atmosphere by Kelvin's law (first part of equation 1). The capillary pressure is itself related to the curvature of the liquid-gas menisci by Young-Laplace's law (second part of equation 1). If the contact angle between the water and the solid phase is null, the two relations imply:

$$\rho_l RT \ln(1/RH) / M = P_{cap} = 2\gamma / r \qquad (1)$$

where ρ_l is the density of water, M the molar mass of the water, R the perfect gas constant, T the temperature, γ is the coefficient of surface tension, (γ=0.073 N/m for air and water under ambient conditions) and r is a pore size. More precisely, r is either the radius of a cylindrical pore or the distance between the two walls of a flat pore. The capillary pressure thus increases as the relative humidity decreases. For water at 20°C, the

capillary pressures corresponding to the imposed relative humidities range from 2.7 MPa for RH = 98% (corresponding to r=53nm) to 114 MPa for RH = 43% (corresponding to r=1.3nm).

A sample successively equilibrated in chambers with increasing relative humidity undergoes a progressive imbibition, from the smaller to the larger pores. At each step, equilibrium is assumed once mass stabilisation of the sample is achieved, which occurs after about two weeks. The mass m(RH) in the partially water saturated state due to the relative humidity RH is measured with a precision of 0.01 g, and will be used after the third step to deduce the partial water saturation.

Step 3: Total Water Saturation. At the end of the previous steps, the samples are water saturated. To do so, the samples are placed in a vacuumed chamber for 24 hour ; they are partially immersed in water for the 6 first hours to allow the air to drain, then fully immersed. The mass in this saturated state m_{sat} is measured. Assuming the final immersion step guarantees a full water saturation, the porosity φ is:

$$\varphi = (m_{sat} - m_{dry}) / (\rho_l V) \quad (2)$$

Porosity measured using this method will be referred to as "water porosity", as opposed to the "gas porosity" to which it will be compared to later in the paper. Additionally, the partial water saturation $S_w(RH)$ achieved at any of the previous steps by equilibrium with relative humidity RH may now be assessed using

$$S_w(RH) = (m(RH) - m_{dry}) / (m_{sat} - m_{dry}) \quad (3)$$

The $S_w - RH$ curve obtained from equation 3 can be used to derive the capillary pressure curve by means of Kelvin's law (equation 1, left). The latter may be used with caution to estimate the pore size distribution through Young-Laplace's law (equation 1, right), provided the pores are assumed to be either cylindrical or flat and connected in a hierarchy from the smallest to the largest.

Gas Porosity Measurements

An alternative porosity measurement method has been also used using a dedicated method (Chen *et al.*, 2013; Nadah *et al.*, 2013) similar in principle to gas pycnometry. The measurement is performed on a dried sample in a confining cell and relies on the injection of 99% pure Argon in the pore network. The room temperature is set to 20°C. Three volumes have to be distinguished: (1) a reference tank with a calibrated volume V_t of 70 mL, (2) the pore volume $\varphi \times V$ to be measured, (3) the volume V_c of the tubes connecting the reference tank to both sides of the sample. The reference tank is initially at a pressure P_t of 1 MPa which is monitored using a pressure sensor with a precision of 100 Pa, whereas the porosity and the connecting tubes are at atmospheric pressure P_{atm} . The valves between the reference tank and the sample are then opened while the pressure in the reference tank is monitored. Once gas pressure and temperature are equilibrated, application of the law of perfect gases in isothermal conditions links the final pressure P_f to the sample porosity through:

$$P_t V_t + P_{atm} (V_c + \varphi V) = P_f (V_t + V_c + \varphi V) \quad (4)$$

The porosity measurement deduced from equation 4 is referred to as "gas porosity". The volume V_c (≈ 5 mL) is measured based on the same principle using a non-porous steel sample.

Gas Permeability Measurements

Gas permeability K is measured using a uniaxial steady state gas flow apparatus. The apparatus consists of a confining cell which is allowed to reach confining pressures P_c as high as 60 MPa, together with a gas injection device (Dana and Skoczylas, 1999, 2002; Lion *et al.*, 2004, Davy *et al.*, 2007; Chen *et al.*, 2012, 2013; Nadah *et al.*, 2013; Duan *et al.*, 2014). The gas used in the current study is 99% pure Argon with a viscosity of $\mu = 2.2\times10^{-5}$ Pa.s.

The injection pressure P_i at the upstream side is set to values ranging from 0.5 MPa to 1.5 MPa, whereas the back-pressure P_d at the downstream side is equal to the atmospheric pressure. The injection pressure is measured with a pressure sensor with a precision of 0.002 MPa. The drainage flow rate q_d at x = h is measured with a set of flow-meters, the finer of them allowing measurement of flow rates from 0.1 ml/min to 1 ml/min with a precision of 0.01 ml/min.

Combining Darcy's law, mass conservation and the law of perfect gases to Klinkenberg's law (1941) to account for slip flow effects yields the expression for the apparent gas permeability K_{app} as a function of the measured drainage flow rate q_d in the steady state regime:

$$K_{app} = K_{int}(1+b/P_m) = 2\mu h P_d q_d / A(P_i^2 - P_d^2) \text{ with } P_m = (P_i + P_d)/2 \qquad (5)$$

where K_{int} is the intrinsic gas permeability, b is Klinkenberg's coefficient and $A = \pi d^2/4$ is the area of the sample section. The equation 5 has been rigorously derived accounting for the non-uniformity of the pressure gradient profile along the sample due to the gas compressibility and is valid irrespective of P_i and P_d, which may be very different. Hence, the plot of K_{app} with respect to $1/P_m$ allows determination of the intrinsic gas permeability and the Klinkenberg coefficient. In practice, three different gas injection pressures are successively applied: 0.5, 1 and 1.5 Mpa.

In order to assess the relative gas permeability as a function of the water saturation S_w, effective gas permeability measurements are performed at each step of saturation obtained by the procedure described above. As the Argon gas injected in the partially water saturated sample is dry, the mass of the sample is checked before and after the measurement to monitor potential desaturation of the sample. In practice for the current study, changes in water saturation due to dry gas injection have been observed to be negligible.

RESULTS

Porosity

The measured "water porosities" (equation 2) and "gas porosities" (equation 4) are reported in Table 1. Water porosities are measured without confining pressure, whereas

gas porosities are measured at three steps of a confining pressure cycle (from 2 MPa to 9 MPa (≈ in-situ pressure) and back to 2 MPa).

	confining pressure (MPa)									
	0	2 → 9 → 2			2	9	2	9	2	9
	porosity				permeability					
sample	water	gas (Argon)			K^{app} (μD) for Pi = 1MPa		K^{int} (μD)		b (MPa)	
MIL-12	10.6	-	-	-	1.44	1.28	0.28	0.23	2.4	2.8
MIL-11	9.6	11.84	10.67	11.53	1.20	1.12	0.18	0.16	3.4	3.6
MIL-14	8.9	12.43	11.69	12.15	1.21	1.13	0.19	0.18	3.3	3.2
MIL-20	14.5	-	-	-	9.41	3.94	7.0	2.4	0.23	0.40
MIL-21	13.3	-	-	-	2.15	1.83	0.55	0.44	1.7	1.9
MIL-22	10.2	12.70	11.79	12.50	1.36	1.26	0.42	0.38	1.1	1.0
MIL-23	9.0	11.65	10.81	11.51	1.13	1.05	0.18	0.16	3.3	3.3
MIL-24	9.1	11.75	11.13	11.77	1.16	1.09	0.19	0.21	3.0	2.5

Table 1. Measured porosities and dry-state gas permeabilities.

Gas porosities exhibit a low dispersion and range from 11.7 to 12.7% at 2 MPa of confining pressure. Water porosities are more dispersed, mostly because of the presence of the two specimens MIL-20 and MIL-21, which have been sampled closer to the upper part of the received core than all other samples.

The water porosities appear to systematically underestimate the gas porosities by 1 to 2 porosity units. As water molecule and Argon atom diameters are respectively 0.28 nm and 0.38 nm, their size cannot explain this discrepancy. The possible origin of this difference may be the sorption of Argon on pore walls during the porosity measurement experiment, which has not been quantitatively assessed.

The confining pressure increase from 2 MPa to 9 MPa leads to a decrease of 1 porosity unit. After unloading, the initial porosity values are retrieved up to the measurement errors. This indicates that the evolution of the samples along the imposed stress path is mostly elastic.

Water Sorption Isotherm, Capillary Curve and Pore Size Distribution

In order to determine the length scales associated with the porosity, the water sorption and desorption curves are measured based on the partial water saturation method described in the previous section. Note that the S_w−RH curves obtained from equation 3

Figure 1. Water sorption-desorption isotherms (left) and inferred cumulative pore size distribution from Kelvin-Laplace's law (right).

and presented in Figure 1 can be used to derive capillary pressure curves by means of Kelvin's law (equation 1).

The desorption curve, which has been measured on a single sample, is slightly above the sorption curves. As for the set of eight sorption curves, the dispersion increases with decreasing capillary pressure ($S_w = 0.68 \pm 0.10$ at $P_{cap} = 2.7$ MPa ; $S_w = 0.115 \pm 0.015$ at $P_{cap} = 114$ MPa). Again, the two specimens MIL-20 and MIL-21, which have the highest total porosities, have also the weakest water saturation at $P_{cap} = 2.7$ MPa. This indicates that the extra porosity of these two specimens is mostly a macro-porosity.

The sorption-desorption curves presented in Figure 1 are re-interpreted as cumulative pore size distributions using Young-Laplace's law (equation 1). To do so, the pores have been assumed flat, i.e. described as the space between two parallel planes with an aperture r, which is of course a rough approximation. Under these assumptions, around 70±5% of the porosity corresponds to pores with an aperture below 50 nm. This fine porosity is attributed to the clay phase, which is located either in the canaliculi spanning carbonate aggregates or in high-porosity pockets. The pore size distribution above 50 nm cannot be evaluated by the present method, but mainly corresponds to the inter-particular pores observed by SEM in the high-porosity pockets.

Gas Permeability

Dry case

The gas permeability has been initially measured on the dried samples using the steady state method. Each sample undergoes a confining pressure cycle from 2 MPa to 9 MPa and back to 2 MPa. At each confining pressure step, the apparent gas permeability is measured for three different gas injection pressures: 0.5 MPa, 1 MPa and 1.5 MPa. Except for the two samples MIL-20 and MIL-21, the apparent gas permeability for an injection pressure of 1 MPa is 1.25±0.15 μD and Klinkenberg corrected intrinsic permeability is 0.24±0.1 μD (see Table 1). The specimens MIL-20 and MIL-21, which

also have more micro-cracks and macro-porosity, have permeabilities 2 to 8 times greater than all other samples.

The moderate increase in confining pressure from 2 to 9 MPa results in a decrease in permeability of only 10%. After unloading to 2 MPa, the initial permeability is almost recovered with less than 5% relative difference. These relatively low fluctuations indicate that the deformation of the samples is mostly elastic during the present load cycle.

Relative gas permeability k_{rg}

In order to assess the relative gas permeability, effective gas permeability measurements are carried out on the partially water saturated samples. At each imposed relative humidity step, the samples undergo the same confining pressure/gas injection pressure cycles as in the dry case.

The measured gas relative permeabilities are reported as a function of water saturation in Figure 2, for confining pressures of 2 and 9 MPa.

Figure 2. Gas relative permeability k_{rg}.

For water saturations below 0.5, effective gas permeabilities exhibited limited hysteresis to a cycle in confining pressure (2→9→2 MPa). However at the highest water saturation tested (corresponding to RH = 98%), the effective gas permeability after the confining pressure cycle ranged only from 1/2 to 1/3 of the value before the cycle, for the same reference value (2 MPa) of confining pressure. Two hypotheses may be proposed to explain this hysteresis: (1) pore compression due to hydrostatic loading induces a spatial reorganisation of the water or (2) the saturation cycle has induced micro-cracking of the samples. Subsequent permeability measurements after a second drying of the samples suggest that limited micro-cracking might indeed have occurred.

Except for the two outlier specimens MIL-20 and MIL-21 which suffered from severe micro-cracking induced by the saturation process, all the measured relative permeabilities in Figure 2 lie on a master curve, for both confining pressures (2 and 9 MPa). The main feature of the relative permeability curve is the presence of a high critical gas saturation S_{gc} around 0.29 ± 0.04 for which gas permeability nearly vanishes. The influence of the

saturation history on the relative permeability curve has not been assessed and requires further investigation. This effect has been studied on two industrial concretes (Chen *et al.*, 2012), evidencing that the saturation history influences k_{rg} mainly in the case of a strong hysteresis in desorption/re-saturation isotherms (i.e. S_w − RH relations), which is not the case of the material presently under consideration (Figure 1).

DISCUSSION

Are the k_{rg} curves obtained relevant for drainage or imbibition ? A priori the saturation protocol relies on a progressive imbibition through the relative humidity technique. Nevertheless, the trapped gas phase is compressed from 1 atm (initial pressure) to very large pressures (Young Laplace) since the pressure is imposed by the size of the throat which trapped the gas. For 50 nm, it gives a pressure of around 30 bars leading to a strong compression and a dissolution of the gas phase in the surrounding water phase. It makes this protocol be an equivalent drainage process since all the gas trapping is progressively and naturally removed by this compression-dissolution mechanism.

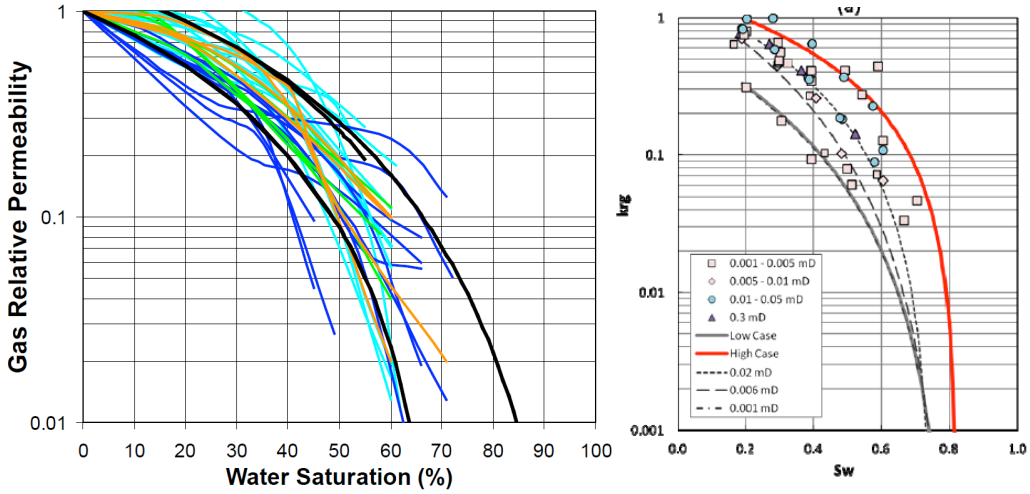

Figure 3. Examples of gas drainage relative permeability curves obtained on tight reservoirs, Cluff and Byrnes, (2010) on the left and Wang et al (2011) on the right)

The gas drainage relative permeability obtained on a caprock facies of extremely low permeability, appear very similar to the ones already published for tight gas reservoirs since they exhibit also very high S_{gc} values (typically in the 15-40% range) as shown in Figure 3 (Cluff and Byrnes,2010; Wang *et al.*, 2011 and Duan *et al.*, 2014). The S_{gc} is defined here as the saturation which corresponds to the apparent beginning of a gas flow in a connected form. Cluff and Byrnes (2010) proposed an empirical formula based on tight reservoir sample to obtain the apparent S_{gc} value ($S_{gc} = 0.15 – 0.05*\log_{10}K$). This does not seem to be applicable for our lower permeability samples since it would give more than 40% rather the observed values in the 25-30% range.

Above the S_{gc} value, the flow topology (connected gas phase) is consistent with the Darcy formalism and therefore a Corey type function appears adequate to reproduce the

general shape of the data (Figure 5). Surprisingly, the gas relative permeability behaviour below S_{gc} has raised little interest to date (Lefort *et al.*, 2011). It is often considered that the gas phase exhibits no mobility at all in this saturation range, which is often referred as the "permeability jail". As pointed out by Cluff and Byrnes (2010), this is not true in a drainage mode by flooding since the gas must have some mobility to make its own saturation increase up to S_{gc}. The expected shape of the k_{rg} curve in this saturation interval have been inferred by combining several sources of information:

1. Although this parameter is difficult to measure directly, both Busch and Amann-Hildenbrand (2013) and Haoguang *et al.* (2014) have reported that very low permeability rocks are characterized by large aspect ratios (pore body size divided by pore throat size). On the opposite, the length ratio (pore body length divided throat length) is small in this particular rocks (elongated throats).

2. Several interesting results can be obtained from the works on the percolation-invasion mechanisms (Lenormand *et al.*, 1983; Wilkinson, 1986). In the percolation regime at low saturation, the k_{rg} is proportional to Sg^{α}. α is in the order of 5 and depends on the conductivity exponent of the medium. It is also established that the aspect ratio plays a major role in the snap-off frequency during the percolation. It therefore suggests that the texture of low permeability rocks significantly favours this mechanism. This could induce the formation of disconnected gas ganglia and a dispersed flow topology at a certain level of gas saturation. This mechanism could be potentially exacerbated by the small length ratio which also prevails in very low permeability rocks. In the configuration of a drainage at low rate with a low viscosity gas phase, the DLA (Diffusion Limited Aggregation) percolation mode is the one which prevails (Lenormand *et al.*, 1988). These snap-off events could occur not only at the flood front but all along the DLA flow path leading to a dispersed, disconnected gas distribution pattern and a reduced gas mobility comparing to what predicts the percolation theory.

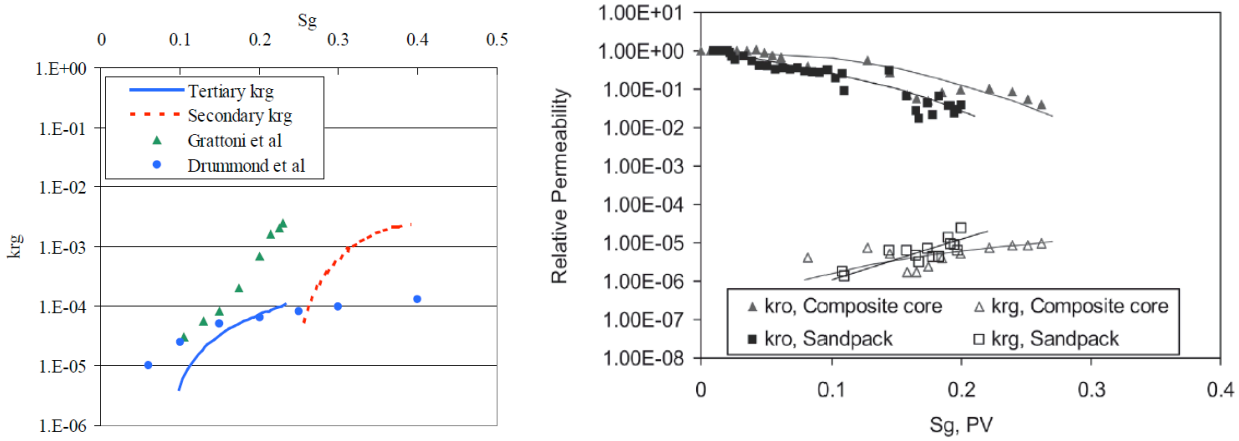

Figure 4. Examples of solution gas relative permeability curves obtained with light oils (Egermann et al., 2004) and heavy oils (Tang et al., 2006)

3. The dispersed flow characteristics have been extensively studied in the context of the recovery processes based on solution gas drive by depletion under secondary / tertiary conditions for both light / heavy oils (Egermann *et al.*, 2004, Bauget *et al.*, 2005, Tang *et al.*, 2006). In these cases, the discontinuous gas phase is created in-situ by nucleation and then diffusion from the solution gas. The DLA – snap-off events suspected in low permeability rocks could conduct to a similar gas distribution pattern once the gas saturation reached a certain value. All the results from the studies on solution gas drive mechanisms converge towards a very typical shape of the k_{rg} curves with a plateau at very low values (Figure 4). Whatever the type of fluid system considered, the plateau is typically located below 10^{-3}-10^{-4}.

By combining these various sources of information, it is then possible to propose what the global k_{rg} shape could be over the whole saturation range. At low saturation (Figure 5 left red curves), the percolation k_{rg} curve is quite steep rather the solution gas drive like k_{rg} curve exhibits a plateau ending at around 10^{-4}. This value is completely speculative and has been chosen only because it seems representative of the values found for similar viscosity ratio cases. Additional studies would be needed to better assess this value according to the rock and fluid/system. At very low S_g, the percolation k_{rg} curve is more relevant (see paragraph 3 above). At higher S_g, a dispersed gas flow regime could start before S_{gc} and then the connected flow (blue part). The proposed shape of k_{rg} below the apparent S_{gc} is a composite curve built from percolation and dispersed flow theory (Figure 5 right green curve). It is interesting to notice that this composite curve is normally completely hidden because the measurement of such low values of k_{rg} are not accessible with standard protocols with low permeability rocks.

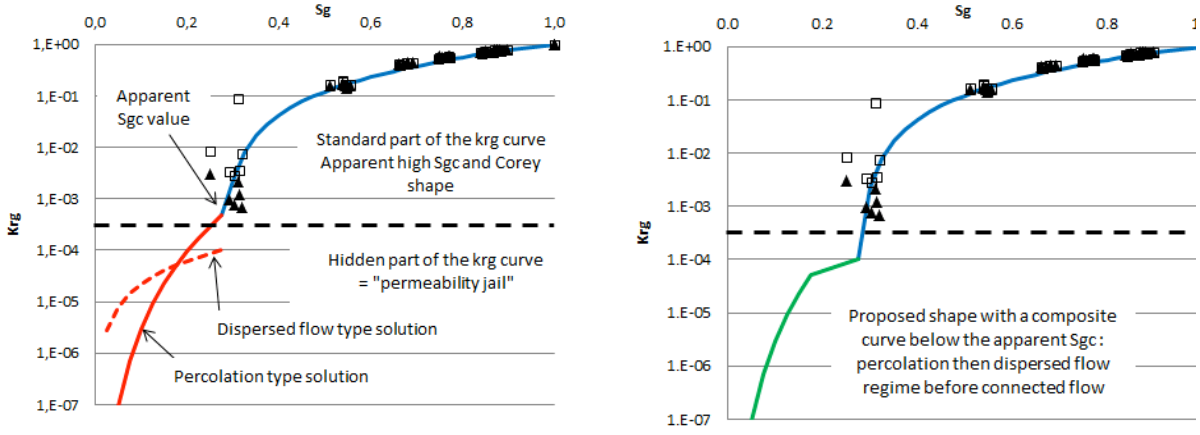

Figure 5. Possible shape of the global krg curve over the whole saturation range for very low K rocks

Having the complete shape of the k_{rg} is of interest for various industrial applications especially those with large time scales, which give more importance about the role played by low k_{rg} values. It concerns mainly the applications related to the basin modelling simulation; the CO_2 storage or the nuclear waste storage (evolution of the associated H_2 produced) where accurate and complete k_{rg} curve description is needed to assess the long fate of the gas phase.

The specific k_{rg} curve shape has also strong implications for gas storage applications since it implies that the gas mobility is very limited at low saturation. It means that a caprock exhibits two interesting features in term of confinement properties. The first is the standard one which consists in a static barrier related to the threshold capillary pressure value. The second one, evidenced by this work, consists in a dynamic barrier, related to the specific gas relative permeability curve shape, which delays significantly the gas flow at low saturations.

CONCLUSION

This paper provides a new complete set of experimental data at various confining pressures to characterize a caprock facies including porosity accessible to gas or water, water sorption-desorption isotherms and gas permeabilities as a function of water saturation, gas injection pressure and confining pressure. The measured relative gas permeabilities lie on a main curve for all samples and exhibit a very high critical gas saturation around 30% where gas flow can be detected. This behaviour is very specific and was already evidenced on tight reservoir samples. Several pieces of information about the pore texture in low permeability rocks, the percolation-invasion mechanisms and the works conducted for determining flow parameters under solution gas drive, have been combined to assess the flow behaviour below this apparent S_{gc} value. A composite curve is proposed which exhibits extremely low gas relative permeability far below the limit of what can be measured in the laboratory in such rocks. When the gas saturation becomes large enough, a connected flow can take place and be measured. This specific behaviour consists in a key feature for various industrial applications with large characteristic times since it rules the flow kinetic in this low gas saturation range and k_{rg} values.

ACKNOWLEDGEMENTS

We are grateful to ENGIE E&P International and Storengy (ENGIE group) for permission to publish these results and to R. Lenormand for fruitful discussions.

REFERENCES

F. Bauget, P. Egermann, R. Lenormand, “A new model to obtain representative field relative permeability for reservoirs produced under solution gas drive”, *SPEREE*, (August 2005), 348-356.

A. Busch, A. Amann-Hildenbrand, “Predicting capillarity of mudrocks”, *Marine and Petroleum Geology,* (2013) **45**, 208-223.

W. Chen, J. Liu, F. Brue, F. Skoczylas, C.A. Davy, X. Bourbon, and J. Talandier, “Water retention and gas relative permeability of two industrial concretes,” *Cement and Concrete Research*, (2012) **42,** 1001–1013.

X.T. Chen, G. Caratini, C.A. Davy, D. Troadec, and F. Skoczylas, “Coupled transport and poro-mechanical properties of a heat-treated mortar under confinement”, *Cement and Concrete Research*, (2013) **49,** 10–20.

R.M. Cluff, A.P. Byrnes, “Relative permeability in tight gas sandstone reservoirs – The “permeability jail” model”, *SPWLA 51th Annual Logging Symposium*, (June 19-23, 2010).

E. Dana and F. Skoczylas, “Gas relative permeability and pore structure of sandstones”, *International Journal of Rock Mechanics and Mining Sciences*, (1999) **36**, 613–625.

E. Dana and F. Skoczylas, “Experimental study of two-phase flow in three sandstones. I. Measuring relative permeabilities during two-phase steady-state experiments”, *International Journal of Multiphase Flow*, (2002) **28,** 1719–1736.

C.A. Davy, F. Skoczylas, J.D. Barnichon, and P. Lebon, “Permeability of macro-cracked argillite under confinement: Gas and water testing”, *Physics and Chemistry of the Earth*, (2007) **32**, 667–680.

Z. Duan, C.A. Davy, F. Agostini, L. Jeannin, D. Troadec, and F. Skoczylas, “Gas recovery potential of sandstones from tight gas reservoirs”, *International Journal of Rock Mechanics & Mining Sciences*, (2014) **65**, 75–85.

P. Egermann, S. Banini, O. Vizika, “Depressurization under tertiary conditions in the near-wellbore region: experiments, visualization and radial flow simulations”, *Petrophysics*, (Sept-October 2004) **45**, n°5.

W. Haoguang, M. Kun, Y. Xiang’an, W. Xinxin, “The relationship of ultra-low permeability sandstone aspect ratio with porosity, permeability”, *Advances in Petroleum Exploration and Development*, (2014) **7**, n°1, 7-12.

L. J. Klinkenberg, “The permeability of porous media to liquids and gases”, In *API Drilling and Production Practices*, New York, API 11th mid-year meeting, Tulsa (1941), 200–213.

R. Lenormand, C. Zarcone, A. Sarr, “Mechanisms of the displacement of one fluid by another in a network of capillary ducts”, *J. Fluid Mech.*, (1983) **135**, 337-353.

R. Lenormand, E. Touboul, and C. Zarcone, “Numerical models and experiments on immiscible displacements in porous media”, *J. Fluid Mech.*, (1988) **189**, 165-187.

M. Lion, F. Skoczylas, and B. Ledésert, “Determination of the main hydraulic and poro-elastic properties of a limestone from Bourgogne, France”, *International Journal of Rock Mechanics & Mining Sciences*, (2004) **41**, 915–925.

J. Nadah, F. Bignonnet, C. A. Davy, F. Skoczylas, D. Troadec, and S. Bakowski, “Microstructure and poro-mechanical performance of Haubourdin chalk”, *International Journal of Rock Mechanics & Mining Sciences*, (2013) **58**, 149–165.

G.-Q. Tang, A. Sahni, F. Gadelle, M. Kumar, A.R. Kovscek, 'Heavy-oil solution drive in consolidated and unconsolidated rock”, *SPE Journal*, (June 2006), 259-268.

D. Wilkinson, “Percolation effects in immiscible displacement”, *Physical review A*, (1986) **34**, n°2, 1380-1391.

P. Lefort, V. Sarrot, M. Prat, J. Talandier, “Hyperslow drainage”, *20ème congrès français de mécanique*, 29 août-2 septembre 2011, Besançon, France.

Y. Wang, Z. Chen, V. Morah, R. J. Knabe and M. Appel. *Gas phase relative permeability characterization on tight gas samples.* SCA2011-13.

MEASUREMENTS OF ROCK CORE DISPERSIVITY AND TORTUOSITY FOR MULTI-PHASE SYSTEMS

Marco Zecca[a], Abdolvahab Honari[a], Sarah J. Vogt[a], Branko Bijeljic[b], Eric F. May[a] and Michael L. Johns[a]
[a] School of Mechanical and Chemical Engineering M050, University of Western Australia, 35 Stirling Highway, Crawley 6009, Western Australia, Australia.
[b] Department of Earth Science and Engineering, Imperial College London, Prince Consort Road, London SW7 2BP, United Kingdom.

This paper was prepared for presentation at the International Symposium of the Society of Core Analysts held in Snowmass, Colorado, USA, 21-26 August 2016

ABSTRACT
Known as CSEGR (Carbon Sequestration with Enhanced Gas Recovery), sequestered CO_2 can be used to re-pressurise partially depleted natural gas reservoirs to increase gas recovery, with the intention to also store the CO_2. Because natural gas and CO_2 are fully miscible, simulations require CO_2-natural gas dispersion at supercritical conditions to be accurately measured in order to quantify this mixing and hence establish the viability of CSEGR. We have designed and constructed a unique core flooding apparatus capable of accurately determining such supercritical gas dispersivity; this has been measured in two sandstones and two carbonates cores as a function of temperature, pressure and interstitial velocity. This is supplemented with Nuclear Magnetic Resonance (NMR) measurements of tortuosity to quantify the underpinning effective diffusion process. The resultant dispersivity data (K - Peclet number (Pe) plot) and tortuosity data are combined and presented in a format which is readily incorporated into CSEGR simulations.

INTRODUCTION
Even though enhanced oil recovery (EOR) via CO_2 flooding is a promising method to improve the recovery factor of oil reservoirs and geologically sequester CO_2, enhanced gas recovery (EGR) with CO_2 flooding/sequestration has not been widely considered by the oil and gas industry. The only current field-scale EGR project is the Rotliegend K12-B gas reservoir, located offshore of the Netherlands, which started in 2004 after 17 years of conventional gas production (Vandeweijer *et al.*, 2011). A Canadian depleted gas reservoir was also used for an EGR/CO_2 sequestration trial in 2002 but the operation was terminated after three years due to the early CO_2 breakthrough into the producing wells (Pooladi-Darvish et al., 2008).

EGR cannot only safely store CO_2 within the formation but also can improve the natural gas recovery by maintaining the reservoir pressure and enhancing sweep efficiency and production rates. However, natural gas and CO_2 are entirely miscible in all proportions and consequently the risks of extensive mixing of these fluids within the reservoir formation and early CO_2 breakthrough into production wells are the main hurdles for EGR implementation. These associated risks and uncertainties of EGR projects can be estimated by using reservoir simulations in which fluid flow in reservoir formations can be quantitatively modeled and, in principle, the mixing process between the injected CO_2 and natural gas captured. Doing so reliably, however, requires (1) adequate characterization of physical dispersion at all relevant length-scales, and (2) that numerical dispersion in such simulations be kept sufficiently small. Extensive studies of dispersion at the field scale have been published (Arya et al., 1988; Coats et al., 2009a; Lake, 1989) but generalizing the results of these studies is not straightforward. Physical dispersion at smaller length scales is also important because the description of transport at the core scale can play an important role in the prediction of mixing at the field scale.

In this work, a unique core flooding apparatus capable of accurately determining supercritical gas dispersivity has been designed and constructed. The measured dispersion coefficients (K_L) of CO_2 and CH_4 for two sandstone cores (Berea and Donnybrook) and two carbonate rock samples (Ketton and Estaillades) are presented over a range of pressure, temperature, and interstitial velocities. These highly reproducible data are used to obtain the characteristic mixing length-scale for the different rocks. These measurements were extended to also consider the effect of residual water on the dispersion process and were supplemented by an independent measurement of tortuosity using appropriate NMR methodology.

THEORY

Dispersion in floods of cylindrical core plugs with injection along the axis can be adequately described by the one-dimensional advective-dispersion (AD) equation:

$$\frac{\partial C}{\partial t} = K_L \frac{\partial^2 C}{\partial x^2} - u_m \frac{\partial C}{\partial x} \quad , \qquad (1)$$

where C is the concentration of the dispersing species, t is time, K_L is the longitudinal dispersion coefficient and u_m is the mean interstitial velocity in the direction of bulk flow, x, in the porous medium. We note the use of alternative models (continuous time random walks and multi-rate mass transfer models) to describe dispersion in more complex, heterogeneous porous media (e.g. Haggerty and Gorelick, 1995; Berkowitz et al., 2006). The ratio of the dispersion coefficient calculated from Eq. (1) to the diffusion coefficient, K_L/D, has been commonly plotted as a function of Peclet number. This is defined here as $\alpha u_m/D$ where α denotes the medium dispersivity. This differs from the classical definition in which grain/particle diameter replaces α as the characteristic length scale for mixing in the pores (Perkins and Johnston, 1963). Note that this latter definition is inappropriate for consolidated media such as the rock cores studied here.

Additionally, Eq.**(2)** has been frequently used to characterize the different dispersion behaviors evident in such correlated data:

$$\frac{K_L}{D} = \frac{1}{\tau} + \frac{\alpha u_m^n}{D}, \quad (2)$$

where τ is tortuosity, and n is an exponent. These three parameters characterize a given porous medium: generally $1 \leq n < 1.5$ (Brigham *et al.*, 1961; Gist et al., 1990; Legatski and Katz, 1967) and τ can range from $\sqrt{2}$ (for ideal packed beds only) to as much as 13 for certain consolidated media (Gist et al., 1990; Hurlimann et al., 1994). Generally for consolidated media these three parameters are treated empirically and must be determined from experiments with the rock; while τ can be determined via several methods, α and n can only be determined from core flooding experiments.

METHODOLOGY

Materials

The methane, carbon dioxide and nitrogen used in our experiments were supplied by BOC Scientific at purities greater than 0.999 mole fraction. Mixtures of CO_2 and CH_4 for pulse injection were prepared gravimetrically. Two types of 1.5 inch diameter sandstone cores, Berea and Donnybrook, and two carbonates, Estillades and Ketton were available. These cores were cleaned prior to use by Soxhlet extraction with a mole fraction mixture of 0.9 dicholormethane (Chem-Supply) + 0.1 methanol (Ajax-Finechem). The geometrical properties of the four cores used are listed in Table 1 with porosities, Φ, and permeabilities, k.

Core	Length (mm)	Diameter (mm)	$p_{confining}$ (MPa)	Φ	k (mD)
Berea sandstone	100.4	37.6	8	0.2043	463.3
			10	0.2039	460.7
			12	0.2036	458.2
Donnybrook sandstone	101	37.5	8	0.1576	12.07
			10	0.1573	12.01
			12	0.1572	11.95
Ketton carbonate	104.7	38.0	8	0.2277	2922.4
			10	0.2274	2912.2
			12	0.2270	2902.7
Estillades carbonate	105.6	37.9	8	0.2817	211.7
			10	0.0811	211
			12	0.2806	210.1

Table 1 Rock cores properties.

Apparatus and method

The specialized core flooding apparatus for $^{SC}CO_2$-CH_4 dispersion measurements was adapted from our previous experimental set-up for breakthrough measurements (Hughes *et al.*, 2012) to allow for pulse injection and to enable water delivery to, and drainage of, the rock core. A schematic of the apparatus is shown in Figure 1. A HPLC switching valve was included to allow for a controlled injection of a pulse of a 50% CH_4 and 50% CO_2 mixture. This composition was calculated as the best trade-off between minimizing density and viscosity contrasts between the fluids and maintaining an adequate signal to noise ratio. Analysis of the core effluent was conducted at measurement pressure using a HPIR cell and a syringe pump was used for effluent collection, ensuring better pressure regulation during the pulse displacement process. Details of the core holder, core wrapping, the core holder bath temperature control, pressure instrumentation and calibration of FT-IR spectrometer are included in our previous work (Hughes *et al.*, 2012). All experiments described below were conducted with the core in a vertical orientation.

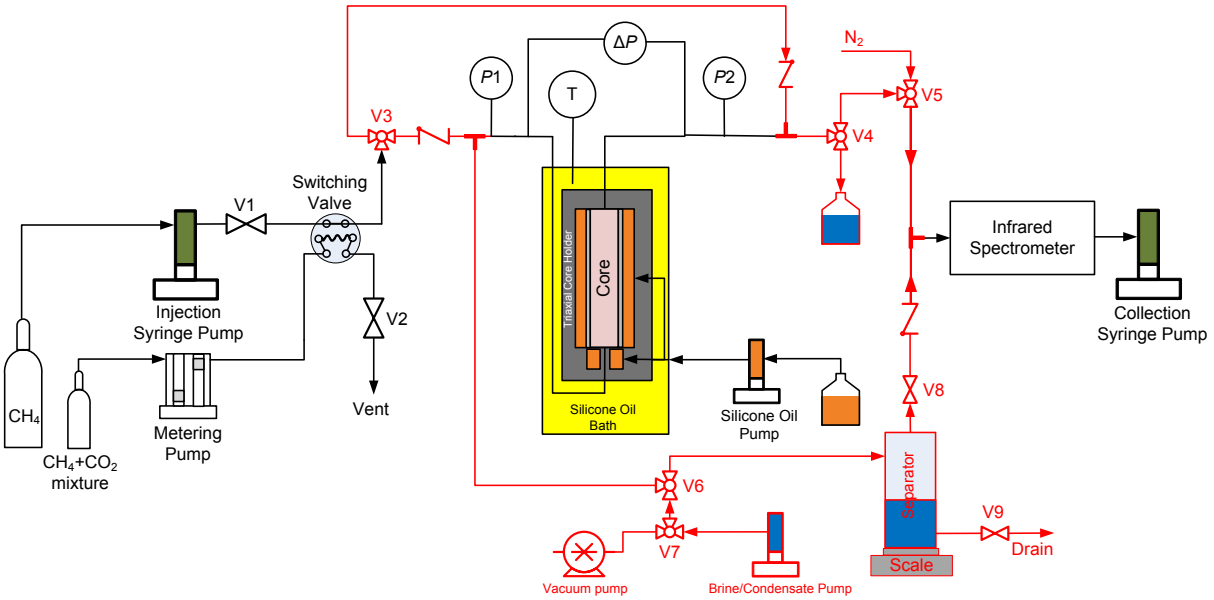

Figure 1 Simplified schematic of the core-flood apparatus for accurate dispersion measurements. The HPLC switching valve is shown in the sample loop filling position. To inject the pulse the valve is switched (rotated 180◦) so that the CH_4 flow flushes the sample out of the loop.

The flow from the injection pump was stopped when the dispersed pulse had passed completely through the IR cell. The experiments were conducted at core temperatures and pressures of 40 to 100 °C and 8 to 14 MPa, respectively, and with interstitial velocities between 0.004 and 1.908 $mm \cdot s^{-1}$.

Data analysis

For pulse experiments, the boundary conditions are:
$C(x > 0, t = 0) = 0$, $C(x = \infty, t) = 0$, $C(x = 0, 0 < t < \delta) = C_0$ and $C(x = 0, t > \delta) = 0$ where δ is the pulse duration. The solution to Eq. (1) with these boundary conditions (Levenspiel, 1999) is:

$$C = \frac{u_m}{\sqrt{4\pi K_L t}} \exp\left(-\frac{\left(L - u_m t\right)^2}{4K_L t} \right), \tag{3}$$

where L is the experimental length scale (core length). Eq.**(1)**, and its solution (Eq.**(3)**) are one–dimensional, as such they are unable to account for any velocity variations in the radial or cross-sectional direction.

However, Eq.**(3)** alone was not adequate for description of the effluent tracer concentration curves produced from the Ketton carbonate because of the non-Fickian/preasymptotic transport behavior associated with its heterogeneity in pore sizes. To describe this non-Fickian flow regime, several alternative models have been developed including the mobile-immobile model (MIM) (Deans (1963)), diffusion models, MRMT models (Haggerty and Gorelick, 1995) and CTRW models (Berkowitz *et al.*, 2006). In this case, it was found that the non-Fickian behavior of Ketton carbonate could be adequately modeled utilizing the MIM approach, which assumes the existence of two distinct regions in the rock, mobile and stagnant/immobile, and which describes the diffusional transport of species between these two zones using a first order mass transfer expression. This model was initially proposed by Deans (1963), who added two new parameters to Eq.**(1)**, namely the mass transfer coefficient and immobile volume fraction, but did not include the longitudinal dispersion coefficient. Coats and Smith (1964) modified Deans' version of Eq.**(1)** by adding this dispersion coefficient to produce (Coats and Smith, 1964; Van Genuchten and Wierenga, 1976)

$$\theta_m \frac{\partial C_m}{\partial t} + \theta_{im} \frac{\partial C_{im}}{\partial t} = \theta_m K_L \frac{\partial^2 C_m}{\partial x^2} - u_m \theta_m \frac{\partial C_m}{\partial x}, \tag{4}$$

$$\theta_{im} \frac{\partial C_{im}}{\partial t} = \beta\left(C_m - C_{im}\right) \tag{5}$$

where C_m and C_{im} are the concentrations of the dispersing solute species in the mobile and immobile regions, respectively; θ_m and θ_{im} are the mobile and stagnant fractions of the fluid in the porous media; β is a mass transfer coefficient; and u_m is the mean interstitial velocity in the mobile zone. To apply this solution to the measured effluent pulse profiles obtained for the Ketton core, the dispersion coefficient (K_L), the mobile fluid fraction (θ_m) and the mass transfer coefficient (β) were treated as the fitting parameters and the measured pulse breakthrough profiles were regressed to the analytical solutions of Eq. **(4)** and Eq.**(5)**.

The dispersion that occurs in the tubing leading to and from the core, and the inhomogeneous velocity profiles around the core entry and exit, both add to mixing and erroneously increase the apparent dispersion. As discussed in our previous work (Hughes *et al.*, 2012), to remove these effects measurements were conducted at the same conditions of T, P and flow rate with short and long Berea rock cores. The concentration profiles collected with the short core were used as inlet boundary conditions to a hypothetical undisturbed core of a length equal to the difference in length between our long and short core. Eq.**(1)** was solved numerically using a central finite difference method (the method of lines) implemented in Matlab within this hypothetical core and regressed to the experimental (long core) data in order to determine K_{corr}. In this manner this systematic error, between K_{long} extracted via Eq.**(3)** and the above methodology employing long and short core, was quantified. The modified setup produced a correction which was significantly dependent on velocity; a clear trend is shown in Figure 2. Consequently all K_{long} data measured for all the rock cores were corrected to account for these systematic errors as shown in Figure 2 to give the K_{corr} values listed in Table 2.

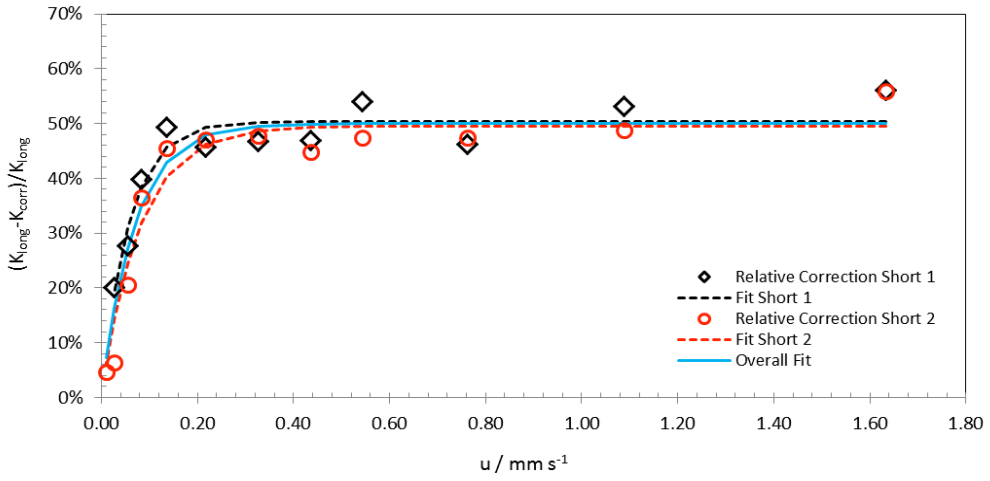

Figure 2 Relative size of dispersion coefficient correction as function of the interstitial velocity. The two data sets correspond to the two halves obtained from the cut of the original long core.

Independent measure of tortuosity

The diffusion coefficients D in Eq.**(2)**, which depend on pressure, temperature and composition, were obtained from the data of Takahashi and Iwasaki (1970). An error in the calculation of D would cause an offset in the value of (K_L/D) determined from the dispersion measurements, which would be most pronounced in the limit $u_m \rightarrow 0$. To confirm that no such offset was present, we measured the core's tortuosity, τ, using a second, completely independent technique. The Berea and Donnybrook rock core samples were evacuated and then saturated with distilled water at a pressure of 10 MPa and left for several hours to ensure complete saturation. These saturated cores were then placed in a 12.9 MHz nuclear magnetic resonance (NMR) rock core analyzer (Oxford Instruments) to

enable self-diffusion measurements via the application of pulsed field gradient stimulated-echo (PGSTE) techniques (Stejskal and Tanner, 1965). Measurement of the water's self-diffusion coefficient for a free liquid sample (D_0) and for the water in the saturated rock core (D), enables calculation of the system tortuosity ($\tau = D_0/D$) if a sufficiently long observation time is allowed to ensure the diffusion within the core is completely restricted. The same experiments were also run with methane at 3MPa providing a tortuosity consistent with the value obtained from water. In future, tortuosity will be measured as a function of the residual water content; D_2O will be adopted to avoid NMR signal from this wetting phase.

RESULTS AND DISCUSSION

'Dry' Sandstones and Carbonates

Table 2 summarizes all our experimental conditions (T, P and u_m), and a selection of dispersion coefficients (K_{corr}) for all the cores considered. The values of K_{corr} have been corrected for entry/exit and tubing effects as outlined above.

Core	T (°C)	P (MPa)	u (mm s^{-1})	D (10^{-8} m^2 s^{-1})	K_{corr} (10^{-8} m^2 s^{-1})
Berea	40	8	0.025	16.4	6.63
	40	8	0.499	16.4	22.12
	40	10	0.006	12.5	3.98
	40	10	0.140	12.5	9.58
	40	12	0.010	10.0	4.00
	40	12	0.199	10.0	10.37
	60	8	0.452	19.6	20.24
	60	10	0.012	15.2	5.39
	60	10	0.304	15.2	13.63
	60	12	0.004	12.3	3.21
	60	12	0.035	12.3	5.36
	80	8	0.034	23.1	8.00
	80	8	0.216	23.1	13.27
	80	10	0.016	18.0	6.18
	80	10	0.085	18.0	8.47
	80	12	0.120	14.7	8.45
	80	12	0.482	14.7	18.67
	100	8	0.085	26.6	10.17
	100	10	0.085	21.0	8.45
	100	10	0.142	21.0	9.64
	100	12	0.085	17.2	7.81
	100	12	0.207	17.2	10.18
Donnybrook	40	8	0.025	16.4	7.21
	40	8	0.140	16.4	18.22
	40	12	0.050	10.0	6.69
	40	12	0.141	10.0	18.66

	60	10	0.007	15.2	5.17
	60	10	0.304	15.2	39.95
	60	12	0.008	12.3	2.72
	60	12	0.035	12.3	5.36
Estillades	40	8	0.09	16.4	10.38
	40	10	0.004	12.5	3.79
	40	10	0.04	12.5	5.76
	40	12	1.151	10	140.03
	60	10	0.23	15.2	21.59
	60	10	1.149	15.2	133.65
	60	12	0.016	12.3	4.39
	60	12	1.646	12.3	214.59
Ketton	40	8	0.053	16.4	17.08
	40	10	0.011	12.5	8.49
	40	10	0.141	12.5	27.06
	40	10	1.124	12.5	212.49
	40	12	1.743	10	381.7
	40	14	1.908	8.1	424.03
	60	10	0.015	15.2	10.03
	60	10	0.745	15.2	115.94

Table 2 Dispersion coefficients of equimolar mixtures of CO_2–CH_4 into pure CH_4 or pure CO_2 for Berea, Donnybrook, Estillades and Ketton cores.

Application of Eq.**(2)** allowed the dispersivity (α) to be determined for the two sandstone cores. For the Berea and Donnybrook rocks, $\alpha = 0.35$ mm and 1.31 mm, respectively, with a relative statistical uncertainty in these parameters from the regression of less than 5%. These values are consistent with those reported for sandstones by Coats *et al.* (2009b), although in the case of the Berea sandstone, the dispersivity measured here is moderately lower than other values reported in the literature (1.2 mm (Gist et al. (1990)); 3.75 mm (Brigham et al. (1961)); 2.2 mm (Legatski and Katz (1967)); 1-6 mm (Schulze-Makuch (2005))). However, as demonstrated by the discussions above, the value of the apparent dispersivity obtained can readily be affected by systematic measurement errors, compounded by the effects on α due to variation in sample length employed and, of course, variability in the actual samples used.

In Figure 3 the pulse breakthrough profiles of Estillades and Ketton carbonates show the reproducibility of the data and the better fitting obtained for Ketton with the MIM model in comparison to the AD equation.

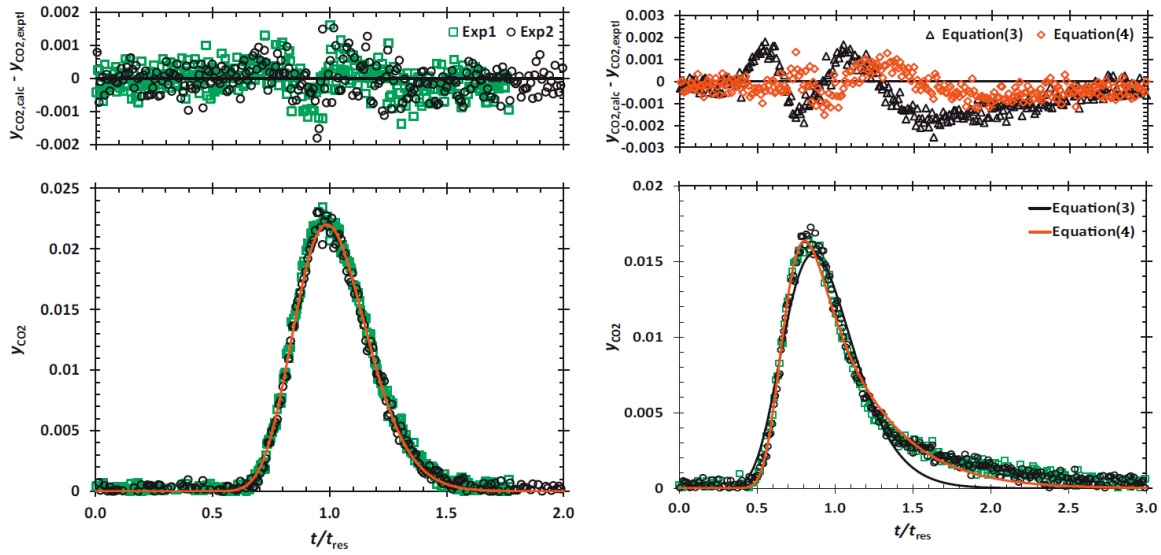

Figure 3 Left: repeatability of the pulse-breakthrough profiles for Estaillades carbonate core at 60°C, 10 MPa and 0.14 mm s^{-1}. Right: Ketton carbonate core at 60°C, 10 MPa and 0.28 mm s^{-1}. The lower panel demonstrates the breakthrough profiles and the fits achieved using Eq. (3) for Estaillades and both Eqs. (3) and (4) for Ketton. The upper panel shows the resulting residuals of the fits.

Our previous results showed the 1D-AD equation was adequate for the description of dispersion of CO_2-CH_4 system through sandstone cores. Larger dispersion coefficients at similar conditions for Donnybrook sandstone were reported, indicating a higher level of heterogeneity relative to the homogenous Berea sandstone. Because carbonate rocks are known as heterogeneous porous media, long tailing and early breakthrough profiles of the CO_2 together with comparatively higher dispersion coefficients were expected. After comparing several measured dispersion coefficients of the sandstones and carbonates at similar conditions, the dispersion coefficients for both carbonate samples were found to be larger than those for the homogeneous sandstone rock (Berea) whereas Estaillades showed similar dispersive behaviour to the more heterogeneous (Donnybrook) sandstone. Ketton exhibited the greatest dispersion among all the core samples used during this study. The pulse breakthrough profiles we observed for Ketton carbonate showed a more persistent long tail and an earlier breakthrough than for Estaillades carbonate.

The calculated dispersivities were then used to produce Figure 4 where the ratios of dispersion and diffusion coefficients, K_{corr}/D, were plotted against Pe_m. Also shown are two curves utilizing Eq.**(2)** where n was 1 for $Pe_m<1$ and 1.2 and 1.4 (power-law scaling) for $Pe_m>1$ (Bijeljic and Blunt, 2006; Bijeljic *et al.*, 2011). Figure 4 explicitly shows that the curves produced using Eq.**(2)** with n = 1.2 for sandstones and n = 1.4 for carbonates are an excellent fit with the Donnybrook and Ketton data respectively for $Pe_m>10$. This provides experimental validation for the power law exponents derived from transport simulations (e.g. Bijeljic and Blunt (2006) and Bijeljic et al. (2011)). Finally, the $Pe_m<100$ considered in the study is lower compared to other standard curves reported in literature

(e.g. Seymour and Callaghan (1997)) since this the IR spectrometer could not detect the breakthrough pulse for higher velocities due to the limited time resolutions of the instrument.

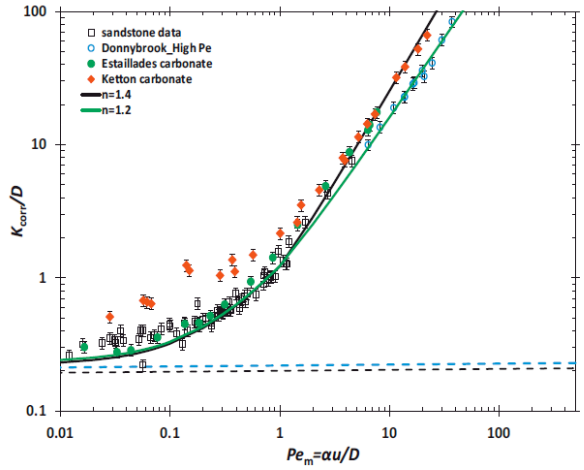

Figure 4 Measured K_{corr}/D vs. Pe_m for Berea and Donnybrook sandstone and Ketton and Estaillades carbonate cores. The dashed lines indicate the independent NMR measurements of sandstone rocks tortuosity. The fitted curves are produced by Eq. (2) for n equal to 1.2 and 1.4.

Inclusion of Residual Water

Figure 5 shows the impact of connate or residual water on the breakthrough profiles for Donnybrook. The presence of this second phase clearly increases the dispersion significantly, the corresponding dispersion coefficients are 5.7×10^{-7} and 39.0×10^{-7} $m^2\cdot s^{-1}$ respectively. Future work will quantitatively measure the dependence of medium properties such as dispersivity on the residual water content.

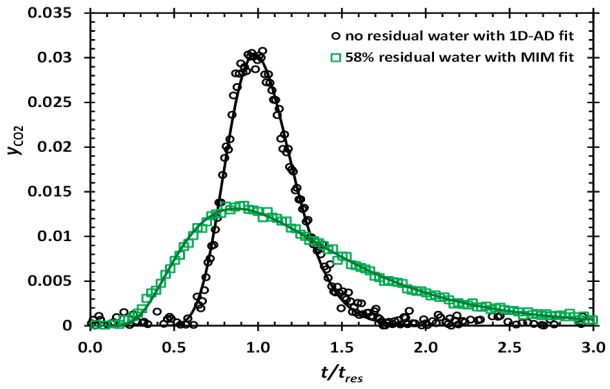

Figure 5 Pulse breakthrough profiles obtained for Donnybrook dry and 58% saturated with water. The measurements were made at 40 °C, 10 MPa and with an interstitial velocities 0.34 $mm\cdot s^{-1}$.

Measurement of Tortuosity

The NMR measurements of tortuosity (τ), using water with diffusion times between 10ms and 1s, were 4.3 and 4.8 for Berea and Donnybrook sandstone cores, respectively. In literature, lower values of tortuosities have been reported from electrical measurements (Zhan et al. (2011)). The tortuosity value for the Berea rock core was also calculated by measuring the self-diffusion coefficient of methane at 3MPa; the tortuosity value in this case was 4.5 which is broadly in agreement with the water measurement. In Figure 6 we show the raw signal attenuation NMR data – the slope of these data provides the diffusion coefficient according to the Stejskal-Tanner equation (Stejskal and Tanner, 1965) and the ratio of the free to restricted diffusion coefficient provides the tortuosity, τ. The diffusion time for these measurements was 100 ms, ensuring the diffusion to be fully restricted ((Hurlimann (1994). In future we will measure τ as a function of water content.

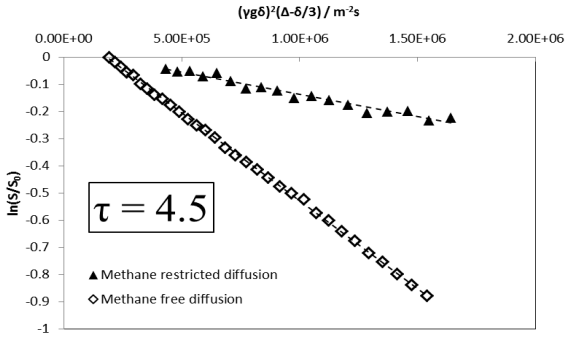

Figure 6 NMR diffusion measurements of free and restricted methane at 3MPa.

CONCLUSIONS

A pulsed measurement apparatus was established for the measurement of the dispersion coefficient (K) for $^{SC}CO_2$ and CH_4 and successfully applied to two sandstones and two carbonates samples. The methodology was adapted to minimize the effects of density and concentration contrasts; the reproducibility obtained were excellent. By using 1D- ADE approach for sandstones and Estillades carbonate and a mobile-immobile model to analyse the breakthrough profiles observed for the Ketton carbonate, asymptotic dispersion coefficients were obtained and compared. All acquired data collapsed onto a common curve when K/D was plotted as a function of Pe_m, capturing variation with temperature and pressure. Preliminary results showed the impact of residual water on the dispersion mechanism and independent measurements of tortuosity with water and methane also produced consistent results.

ACKNOWLEDGEMENTS

This work was supported by the Western Australian Department of Environment and Conservation through the Low Emissions Energy Development fund.

REFERENCES

Arya, A., Hewett, T. A., Larson, R. G., Lake, L. W., 1988. Dispersion and reservoir heterogeneity SPE Reservoir Engineering 3, 139-148.

Berkowitz, B., Cortis, A., Dentz, M., Scher, H., 2006. Modeling non-fickian transport in geological formations as a continuous time random walk, Reviews of Geophysics 44, 1-49.

Bijeljic, B., Blunt, M. J., 2006. Pore-scale modeling and continuous time random walk analysis of dispersion in porous media, Water Resources Research 42, W01202.

Bijeljic, B., Mostaghimi, P., Blunt, M. J., 2011. Signature of non-Fickian solute transport in complex heterogeneous porous media, Physical Review Letters 107, 204502.

Brigham, W. E., Reed, P. W., Dew, J. N., 1961. Experiments on mixing during miscible displacement in porous media, SPE Journal 1, 1-8.

Coats, K. H., Smith, B. D., 1964. Dead-end pore volume and dispersion in porous media, SPE Journal 4, 73-84.

Coats, K. H., Whitson, C. H., Thomas, L. K., 2009a. Modeling Conformance as Dispersion, SPE Reservoir Evaluation & Engineering 12, 33-47.

Coats, K. H., Whitson, C. H., Thomas, L. K., 2009b. Modeling conformance as dispersion, SPE Reservoir Evaluation & Engineering 12, 33-47.

Deans, H. A., 1963. A mathematical model for dispersion in the direction of flow in porous media Society of Petroleum Engineers Journal 3, 49-52.

Gist, G. A., Thompson, A. H., Katz, A. J., Higgins, R. L., 1990. Hydrodynamic dispersion and pore geometry in consolidated rock, Physics of Fluids A 2, 1533-1544.

Haggerty, R., Gorelick, S. M., 1995. Multiple-rate mass transfer for modeling diffusion and surface reactions in media with pore-scale heterogeneity, Water Resources Research 31, 2383-2400.

Hughes, T. J., Honari, A., Graham, B. F., Chauhan, A. S., Johns, M. L., May, E. F., 2012. CO_2 sequestration for enhanced gas recovery: new measurements of supercritical CO_2-CH_4 dispersion in porous media and a review of recent research, International Journal of Greenhouse Gas Control 9, 457-468.

Hurlimann, M. D., Helmer, K. G., Latour, L. L., Sotak, C. H., 1994. Restricted diffusion in sedimentary rocks. determination of surface-area-to-volume ratio and surface relaxivity, Journal of Magnetic Resounance, Series A 111, 169-178.

Lake, L. W., 1989. Enhanced oil recovery Prentice Hall 550, New Jersey, USA.

Legatski, M. W., Katz, D. L., 1967. Dispersion coefficients for gases flowing in consolidated porous media, SPE Journal 7, 43-53.

Levenspiel, O., 1999. Chemical reaction engineering 3rd ed. John Wiley & Sons.

Perkins, T. K., Johnston, O. C., 1963. A review of diffusion and dispersion in porous media, SPE Journal 3, 70-84.

Pooladi-Darvish, M., Hong, H., Theys, S., Stocker, R., Bachu, S., Dashtgard, S., 2008. CO_2 injection for enhanced gas recovery and geological storage of CO_2 in the long Coulee Glauconite F pool, Alberta. In SPE (Ed.), SPE Annual Technical Conference and Exhibition, Denver, Colorado.

Schulze-Makuch, D., 2005. Longitudinal dispersivity data and implications for scaling behavior, Ground Water 43, 443-456.

Seymour, J. D., Callaghan, P. T., 1997. Generalized Approach to NMR Analysis of Flow and Dispersion in Porous Media, AIChE Journal 43, 2096-2111.

Stejskal, E. O., Tanner, J. E., 1965. Spin diffusion measurements: spin echoes in the presence of a time dependent field gradient The Journal of Chemical Physics 42, 288-292.

Takahashi, S., Iwasaki, H., 1970. The diffusion of gases at high pressures. III. The diffusion of $^{14}CO_2$, in the $^{12}CO_2$-CH_4 system, Bulletin of the Chemical Research Institute of Non-Aqueous Solutions, Tohoku University 20, 27-36.

Van Genuchten, M. T., Wierenga, P. J., 1976. Mass transfer studies in sorbing porous media I. analytical solutions, Soil Science Society of America Journal 40, 473-480.

Vandeweijer, V., van der Meer, L. G. H., Hofstee, C., Mulders, F., Graven, H., D'Hoore, D., 2011. Monitoring CO_2 Injection at K12-B http://www.co2geonet.com/UserFiles/file/Open%20Forum%202011/PDF-presentations/2-10_Vanderweijer.pdf.

Zhan, X., Zhu, Z., ToksoZ, M. N., 2011. Quantitative DC and high frequency AC seismoelectric measurement on Berea sandstone, SEG Technical Program Expanded Abstracts 30, 2246-2250.